ETH. DISS. NO 21677

Influence of Rotational Energy Transfer on Quantitative O_2 Laser-Induced Fluorescence Measurements in Flames

A dissertation submitted to attain the degree of

Doctor of Science
(Dr. sc. ETH Zürich)

presented by
Felix Grygier
Dipl.-Ing. Universität Stuttgart
born 27th of February, 1983
citizen of Germany

accepted on the recommendation of
Prof. Alexander Wokaun
Prof. Martin Quack
Dr. Alexey Denisov

2014

To Yvonne, Karin and Ronald

Abstract

Laser-induced fluorescence (LIF) is a widely used technique in combustion diagnostics due to its high detection sensitivity and its potential for 2-D and even 3-D applications. Commonly used diagnostic molecules are e.g. the OH radical for flame front detection or the NO radical for concentration or temperature measurements. Their spectroscopic properties and important collisional processes for quantitative LIF interpretation are well investigated. Despite of its predissociative nature, which is beneficial for high-pressure LIF as the signal is less affected by fluorescence quenching, the O_2 molecule is not often used and collisional processes relevant in combustion environments are not investigated to the same detail. One of the possible reasons is that a saturation effect of the LIF signal was observed when employing high energy lasers, which is not quantitatively understood. This saturation is the result of the competition of laser excitation and ground state rotational energy transfer (RET).

In this work, I introduce an experimental setup including a data acquisition routine and propose a kinetic model to investigate the saturation of O_2 LIF. Concerning the modeling, I show that a relatively simple three-level model provides the best agreement with experimental data. A comparison of this model to others, including a more detailed description of RET population exchange indicates why the three-level model better represents the experimental data. Quantitative analysis with the three-level model at different pressures and for different flame gas compositions indicates that the saturation of the O_2 LIF signal decreases with increasing pressure, although the dependence is not linear. In addition I found that the saturation depends on the flame gas composition, but not on the ro-vibronic transition in the investigated range. I show that the common O_2 simulation tools can be expanded to predict the saturation effect.

With respect to practical application of O_2 LIF, I propose the use of 2-D O_2 LIF to locate flame fronts in rich flames. The accuracy of this method is experimentally compared to traditionally used OH LIF and found to be identical. For quantitative spectral analysis I show that a non-negative matrix factorization method can successfully decompose an O_2 spectrum into its different vibronic contributions. From this decomposition, I can estimate an upper bound of the quenching cross section of excited B-state O_2 and show that quenching can be neglected for quantitative LIF investigations up to at least 10 bar.

Zusammenfassung

Die Laser-induzierte Fluoreszenz (LIF) ist eine weit verbreitete Diagnosetechnik in der Verbrennungsforschung. Ihre hohe Empfindlichkeit erlaubt bildgebende Verfahren bis hin zur dreidimensionalen Erfassung von Konzentrationsfeldern. Häufig wird in der LIF Diagnostik das OH-Radikal zur Visualisierung der Flammenfront angeregt. Das NO-Radikal kann mit LIF direkt in der Entstehung dargestellt werden und eignet sich zum Erfassen zweidimensionaler Temperaturfelder. Die spektroskopischen Eigenschaften beider Moleküle und die für quantitative LIF Messungen relevanten Stossprozesse sind eingehend untersucht und weitgehend bekannt. Obwohl das stark prädissoziierende O_2 Molekül sehr gut für quantitative LIF bei hohen Drücken geeignet wäre, da das LIF Signal nur wenig von Stosslöschung beeinflusst ist, wird es selten in der Flammendiagnostik genutzt. Die unter Flammenbedingungen auftretenden Stossprozesse sind weit weniger gut untersucht. Ein möglicher Grund hierfür ist, dass ein Sättigungsprozess bei der Anregung mit starken Lasern beobachtet wurde, der bisher nur qualitativ beschrieben wurde. Diese Sättigung ist das Ergebnis aus dem Zusammenspiel von Laseranregung und Rotationsenergie Transfer (RET) im Grundzustand.
In dieser Arbeit beschreibe ich sowohl einen Versuchstand mit der dazugehörigen Messtechnik als auch ein kinetisches Modell um die Sättigung von O_2 LIF zu untersuchen. Bezüglich der Modellierung zeige ich, dass ein recht einfaches drei-Niveau-Modell die beste Übereinstimmung mit experimentell gewonnenen Daten aufweist. Ein Vergleich mit anderen Modellen, in denen auch der RET Populationsaustausch präziser beschrieben ist, liefert Erklärungen warum das drei Level Model die beste Übereinstimmung aufweist. Die quantitative Datenauswertung mithilfe des drei-Niveau-Modells zeigt, dass die Sättigung erwartungsgemäss mit steigendem Druck abnimmt. Unerwartet war, dass dieser Zusammenhang nicht linear ist. Erweiterte Messungen zeigen, dass die Sättigung von der Zusammensetzung des brennbaren Gasgemischs abhängt, aber innerhalb der untersuchten Bedingungen nicht von dem ro-vibronischen Übergang. Diese Ergebnisse nutze ich um ein gängiges Simulationsprogramm zu erweitern, das dann den Sättigungseffekt korrekt abbildet.
In einer praktischen Anwendung beschreibe ich die Möglichkeit 2-D O_2 LIF zur Lokalisierung von Flammenfronten unter fetten Verbrennungsbedingungen zu nutzen. Die

Genauigkeit dieser Methode erweist sich in Experimenten als gleichwertig verglichen mit traditioneller OH LIF.
Mithilfe einer nicht-negativen Matrix Faktorisierung zeige ich, dass ein O_2 Spektrum in seine vibratorischen Komponenten zerlegt werden kann. Diese Zerlegung ermöglicht es eine obere Grenze für den Querschnitt Stosslöschung des angeregten O_2 Zustands abzuschätzen. Es zeigt sich, dass Stosslöschung für Drücke bis mindestens 10 bar vernachlässigt werden kann.

Acknowledgement

I would like to thank Prof. Alexander Wokaun, head of the general energy department and referent of my thesis, as well as Dr. Peter Jansohn, head of the Laboratory of Combustion research who made my PhD thesis at the Paul Scherrer Institut possible.
It is very important to me to express my special appreciation and thanks to Dr. Alexey Denisov, my direct supervisor, for all his scientific and experimental support. You helped so much to form a combustion spectroscopist from an engineer.
I thank Prof. Martin Quack for kindly accepting the task of being co-examiner of this thesis and for the inspiring discussions.
I would like to thank Dr. Rolf Bombach for all his support in the lab and the fruitful scientific discussions. And for our common lunch breaks conversations.
For our common effort of renewing the high-pressure burner control soft- and hardware, I thank Dr. Rolf Bombach and Dr. Alexey Denisov. The burner can now be operated safer and much more flexible.
I also thank Marco Schultze and Dr. Yiannis Mantzaras for our successful project on planar O_2 LIF at the TCC test rig.
I thank Marco Schultze, Dr. Rolf Bombach, Dr. Alexey Denisov, Dr. Christos Frouzakis and Yu-Chun Lin for providing me with drawings and pictures of experiments, allowing me to better introduce laser diagnostic based topics.
The technical support by Daniel Erne, Pascal Beerkircher, Markus Obrist and Jürgen Theile is gratefully acknowledged.
I like to thank the other members of my group Hannelore Krüger for all her administrative support, Dr. Walter Hubschmid for his mathematical skills, Dr. Klaus Hoyer, Dr. James Mannekutla, Giacomo Colmegna for the easy lab exchange, and my PhD colleagues Yu-Chun Lin, Dr. Salvatore Daniele, Milosz Matuszewski and Dario Wüthrich who accompanied me during my time at PSI. It is sometimes helpful if people around share comparable challenges.
I also thank my colleagues who enriched my time at PSI in inspiring coffee break discussions or during tennis matches: Vera Tschedanoff, Sinan Teske, Simon Maurer, Philip Edinger, Dr. Urs Rhyner, Jessica Settino, Yaroslaw Sych, Dr. Nikolaos Prasianakis, Martin Künzle, Thomas Thüring, Dr. Christian Grünzweig, Silke Pfinninger, Dr. Katja Rinne

and many more.
The funding of this work provided by the Swiss National Science Foundation (SNF project 200021_121947) is gratefully acknowledged.
I thank Prof. Christoph Schulz for providing us with the LIFSIM code, Dr. Christoph Schneider for borrowing me the beam profile camera and Dr. Wolfgang Kreutner for having the initial idea of this project.

Contents

List of Figures

List of Tables

Nomenclature

Abbreviations

EGL	Exponential gap law
FWHM	Full width at half maximum
HPB	High pressure burner
ICCD	Intensified charge-coupled device
LIF	Laser-induced fluorescence
MEG	Modified exponential gap law
NMF	Non-negative matrix factorization
RET	Rotational energy transfer
VET	Vibrational energy transfer

Constants

k_B	$k_B = 1.3806488 \cdot 10^{-23}\,\mathrm{J/K}$	Boltzmann constant
c	$c = 299792458\,\mathrm{m/s}$	Speed of light
h	$h = 6.62606957 \cdot 10^{-34}\,\mathrm{Js}$	Planck constant

Math Symbols/Variables

A	Spontaneous emission rate constant	$[\,s^{-1}]$
B	Einstein B coefficient	$[m^3/(Js^2)]$
b	Excitation / stimulated emission rate constant	$[\,s^{-1}]$
B_{rot}	Rotational constant	$[\,cm^{-1}]$
E	Engergy	$[\,J]$
F	Fluorescence signal	$[\,a\,u\,]$
FC	Fluorescence constant	$[\,a\,u\,]$
I	Laser intensity	$[\,W/m^2]$
J	Rotational quantum number	[-]
k	Rotational energy transfer state-to-state rate	$[\,s^{-1}]$
l	Angular momentum quantum number	[-]
λ	Air excess ratio	[-]
N	Population	[-]
P	Predissociation rate constant	$[\,s^{-1}]$
p	Pressure	[bar]
φ	Fluorescence quantum yield	[-]
Q	Quenching rate constant	$[\,s^{-1}]$
Q_{RET}	Rotational energy transfer rate constant	$[\,s^{-1}]$
σ	Collisional cross section	$[\,Å^2]$
T	Temperature	[K]
t	Time	[s]
τ	Laser pulse length	[s]
v	Vibrational quantum number	[-]

1. Introduction

According to the World Energy Resources Report 2013 by the World Energy Council [1], in 2011 82 % of the world's primary energy supply was based on fossil fuels. Although this share is predicted to decrease in the future as renewable resources become more and more available, the absolute amount of energy supplied by fossil fuel keeps increasing as the total primary energy demand increases as well. The anthropogenic combustion of fossil fuels changes the Earth's energy budget and, according to the IPCC's WP1 summary of the 5th assessment report [2], is a driver for climate change. Changes of energy fluxes to the Earth's energy budget are quantified by radiative forcing, where positive forcing leads to surface warming. The largest contribution to the change of radiative forcing is caused by the increase in the atmospheric concentration of CO_2 since 1750 [2]. Even though the long-term aim should be to supply the world entirely with renewable and thus sustainable energy, improving fossil fuel combustion is a powerful way to reduce emissions of CO_2 and other pollutants in the meantime. As an example, a 1% improvement in the efficiency of a conventional pulverized coal combustion plant results in a 2-3% reduction in CO_2 emissions. Highly efficient modern coal plants emit almost 40% less CO_2 than conventional plants [1]. Modern combustion research looks at new technologies, such as pre- and post-combustion carbon storage that require combustion of different fuels or fuel compositions, respectively and different ways of combustion, e.g. partially catalytic supported combustion. This also includes challenges in combustion of renewable energy carriers and the need of more flexible combustion systems.
To understand and improve combustion processes, laser diagnostics provide powerful methods to yield information about the complex interaction between fluid mechanics and chemical kinetics. They allow to measure in-situ and non intrusively important characteristics such as flow field, temperature, species concentrations and reaction zone location with high temporal and spatial resolution as well as high accuracy and precision. Common laser optical techniques to measure flow fields include particle image velocimetry (PIV) or laser Doppler anemometry (LDA), wheres laser-induced fluorescence (LIF) coherent anti-Stokes Raman spectroscopy (CARS) and Raman spectroscopy are common laser spectroscopical techniques to conclude chemical properties e.g. temperature, species concentrations or 2-D images of the flame front. In Figure 1.1, I show as an

example LIF applied to a Bunsen flame. Different species act as indicators, CH_2O can be used as a precursor of the reaction zone in which the fuel is thermally decomposed. CH can be used to visualize the rich premixed reaction zone whereas OH can be used to visualize the diffusion flame front.
In this work, I am investigating LIF of the O_2 molecule. I will explore whether O_2 LIF can extend diagnostic capabilities to new combustion systems in which traditional methods cannot be applied anymore. Concerning quantitative LIF with the O_2 molecule in high pressure flames, a better understanding of quenching and relaxation processes of O_2 is needed. This work strives to fill gaps in the knowledge of spectroscopic properties of O_2 at technical combustion relevant conditions.

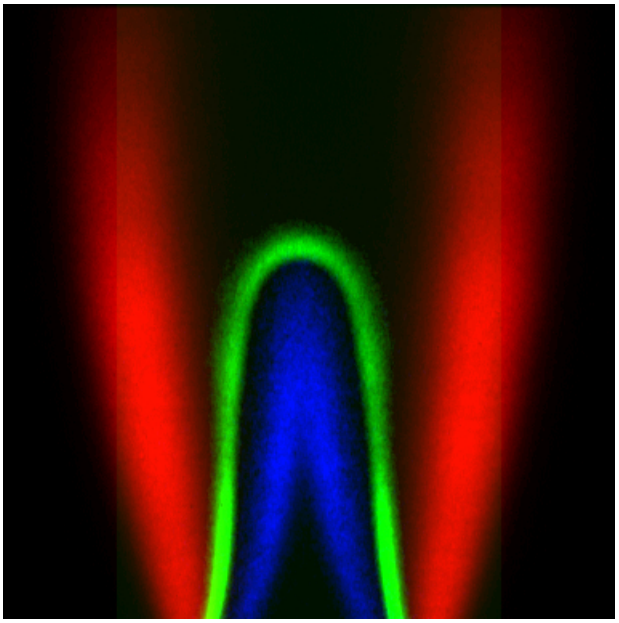

Figure 1.1.: LIF in a Bunsen flame, taken from Bombach and Käppeli [3]. Blue color shows fluorescence of CH_2O, green color of CH and red color of OH.

2. Background

The relevant theoretical and experimental background information is briefly given in this chapter. Important spectral properties of the O_2 molecule and their influence on LIF are discussed as well as important collisional processes regarding LIF. A literature overview concerning O_2 spectroscopy in flames is given at the end of the chapter.

2.1. Spectral Properties of the Oxygen Molecule

Oxygen is one of the most abundant and most important chemical elements for life on Earth. Oxygen was discovered by C.W. Scheele, a Swedish pharmacist in 1771. Due to its importance to many fields of science (e.g biology, medicine, chemistry, combustion) it has been widely investigated. Oxygen (O_2, in the entire work I will refer to O_2 always as the molecule consisting of two ^{16}O atoms) is spectroscopically well investigated [4] and has a dominant UV absorption band around 200 nm which is named after German physicist V. Schumann and German mathematician C.D. Runge. Schumann [5] discovered this absorption band system in 1903 during his pioneering work in the spectral region below 200 nm. Runge [6] found in 1921 excitation bands of atmospheric O_2 at wavelenghts above 200 nm which were found to belong to the same system. Both should have immediately observed ozone formation by its smell. This mechanism is also responsible for ozone formation in the atmosphere. The reactions can be written as

$$O_2 \xrightarrow{h\nu} 2O \tag{2.1}$$

$$O_2 + O + M \rightarrow O_3 + M \tag{2.2}$$

The physics behind reaction 2.1 can be explained with the spectral properties of the Schumann-Runge system. The system denotes transitions between the electronic ground state ($X^3\Sigma_g^-$) and an excited electronic state ($B^3\Sigma_u^-$), which have been subject to many investigations during the last century e.g. by Curry and Herzberg [7], Creek and Nicholls [8], Slanger and Cosby [9], Lewis et al. [10], Sick and Szabadi [11]. Figure 2.1 shows for this work relevant potential energy functions of O_2 electronic states. Two important aspects can be seen from this figure: i) The equilibrium distance between O-atoms in the

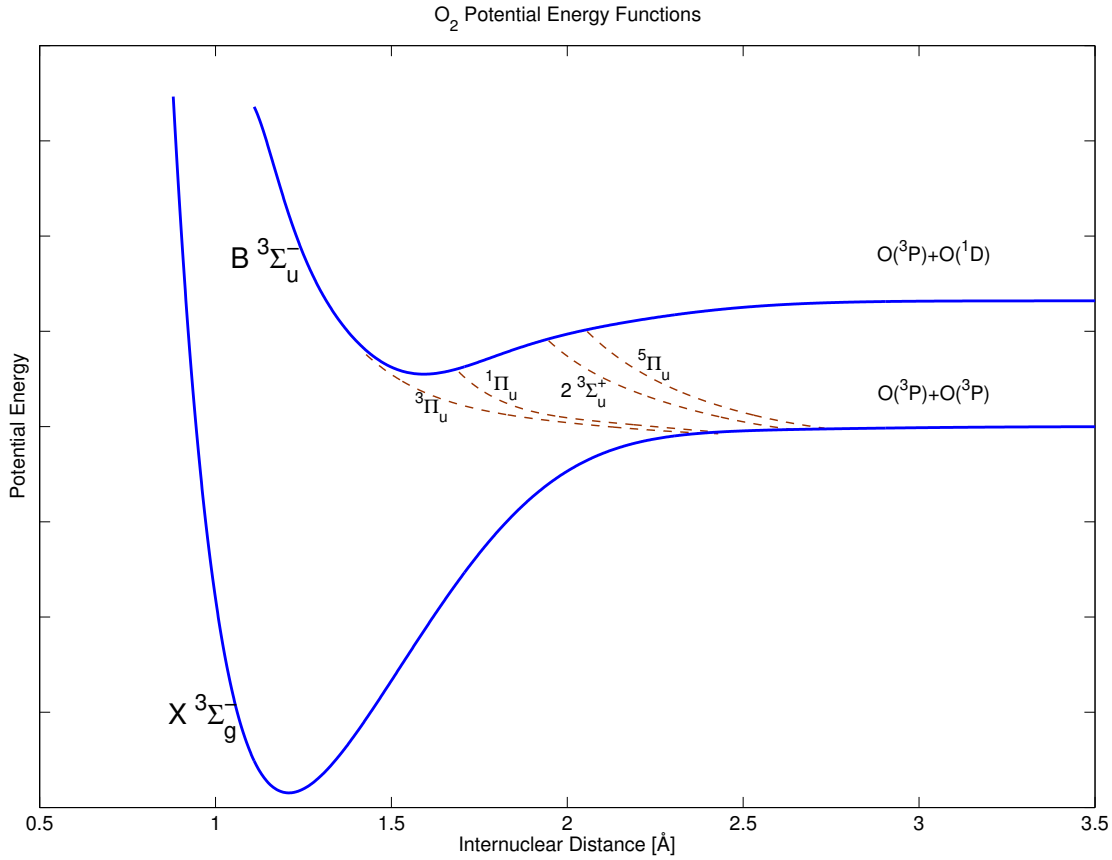

Figure 2.1.: Potential energy functions of O_2, data compiled from Bytautas et al. [12] and Decker [13].

excited ($X^3\Sigma_g^-$) state is about 0.4 Å larger than in the ground state, resulting in a large number of allowed vibrational transitions. This explains the wide absorption range and the atmospheric opacity below 200 nm. ii) The repulsive states ($^3\Pi_u, ^1\Pi_u, 2^3\Sigma_u^+, ^5\Pi_u$), crossing the $B^3\Sigma_u^-$ state potential curve are responsible for the large predissociation rates of excited O_2 molecules. Franck Condon factors of the Schumann-Runge system are shown in Figure A.1.

The molecular orbital scheme with the electron occupation of the O_2 ground state is shown in Figure 2.2. This scheme can be used to describe O_2 and F_2, whereas for B_2 C_2 or N_2, $\sigma_g 2p$ lies energetically higher than $\pi_u 2p$. The electron configuration of the O_2 ground state is thus

$$(\sigma_g 1s)^2(\sigma_u^* 1s)^2(\sigma_g 2s)^2(\sigma_u^* 2s)^2(\sigma_g 2p)^2(\pi_u 2p)^4(\pi_g^* 2p)^2$$

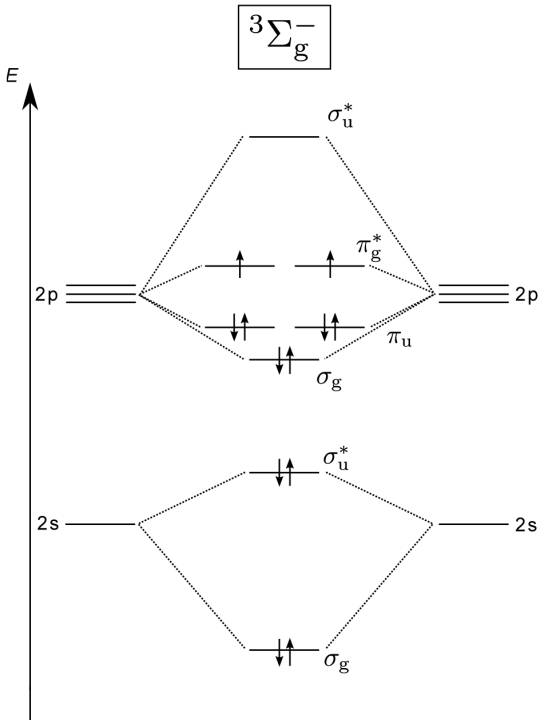

Figure 2.2.: Molecular orbital scheme of O_2 with ground state electron occupation. The molecular orbitals arising from the 1s atomic orbitals are not shown, as they are almost completely localized on the atoms and lie significantly lower in energy.

which would allow according to the Pauli principle the term symbols $^3\Sigma_g^-$, $^1\Delta_g$ and $^1\Sigma_g^+$. With Hund's rule $^3\Sigma_g^-$ can be identified as the ground state. The term symbol for the excited state is $^3\Sigma_u^-$. The term symbols specify symmetry properties of the electronic wave function Ψ_{elec}: The 'g' or 'u' subscripts imply symmetry or antisymmetry, respectively, to inversion through the center of a diatomic molecule and the subscript '+' or '-' relate to symmetry or antisymmetry with respect to reflection across a plane containing the internuclear axis.

As ^{16}O atoms have a nuclear spin of zero, their nuclei are bosons and thus the total wave function of O_2 must be symmetric with respect to the permutation of the two ^{16}O nuclei.

For O_2, the total wave function can be written as:

$$\Psi_{total} = \Psi_{elec}\Psi_{vib}\Psi_{rot}\Psi_{nucl}. \tag{2.3}$$

The vibrational wave function Ψ_{vib} depends only on the distance between the two nuclei which is not affected by the permutation. Therefore Ψ_{vib} is symmetric. The nuclear spin wave function Ψ_{nucl} is symmetric for the nuclear spin of zero of ^{16}O. The rotational wave function Ψ_{rot} is symmetric for even rotational quantum numbers J and antisymmetric for odd J. To determine the symmetry of the electronic wave function Ψ_{elec} with respect to the permutation of two atoms, this permutation can be represented by a combination of an inversion and a reflection. Thus, Ψ_{elec} for the $X^3\Sigma_g^-$ state is antisymmetric and is symmetric for the $B^3\Sigma_u^-$ state. Consequently, for the O_2 ground state only odd J values are allowed and for the excited state only even J values. Thus, Q-branch lines with $\Delta J = 0$ are not visible in the ro-vibronic spectra of the O_2 Schumann-Runge system.
The coupling of the angular momenta of the O_2 can be described with Hund's case b, as for the Σ state of O_2 the orbital angular momentum is zero. The coupling between the rotation (quantum number J) and the spin (quantum number S) results in a splitting of the rotational level into three components (F_1, F_2, F_3).

2.2. Laser-Induced Fluorescence

Laser-induced fluorescene (LIF) is a widely used technique in combustion diagnostics. The two main reasons for that are the high sensitivity of the technique which allows for the detection of combustion radicals and its capability for 2-D imaging. LIF for combustion species has been described in detail by Eckbreth [14] and Kohse-Höinghaus [15, 16]. I will briefly summarize the relevant information regarding this work using the nomenclature of Eckbreth [14].

2.2.1. Molecules Used for LIF in Gas Combustion

The combustion of hydrocarbons can be described with a global reaction equation e.g. for methane

$$CH_4 + 2O_2 \rightleftharpoons CO_2 + 2H_2O. \tag{2.4}$$

This global equation can not represent the complexity of interaction between the various elementary reactions and intermediate species which occur during the oxidation reaction. Figure 2.3 shows a simplified reaction path scheme for lean CH_4 combustion as developed by Frouzakis and Boulouchos [17].
A detailed reaction mechanism for modeling hydrocarbon combustion is the GRI 3.0 mechanism, developed at the UC Berkeley [18] (all chemical combustions simulations in this work are calculated with the GRI 3.0 mechanism). This mechanism takes 53 species and 325 elementary reactions into account. Some of these intermediate combustion

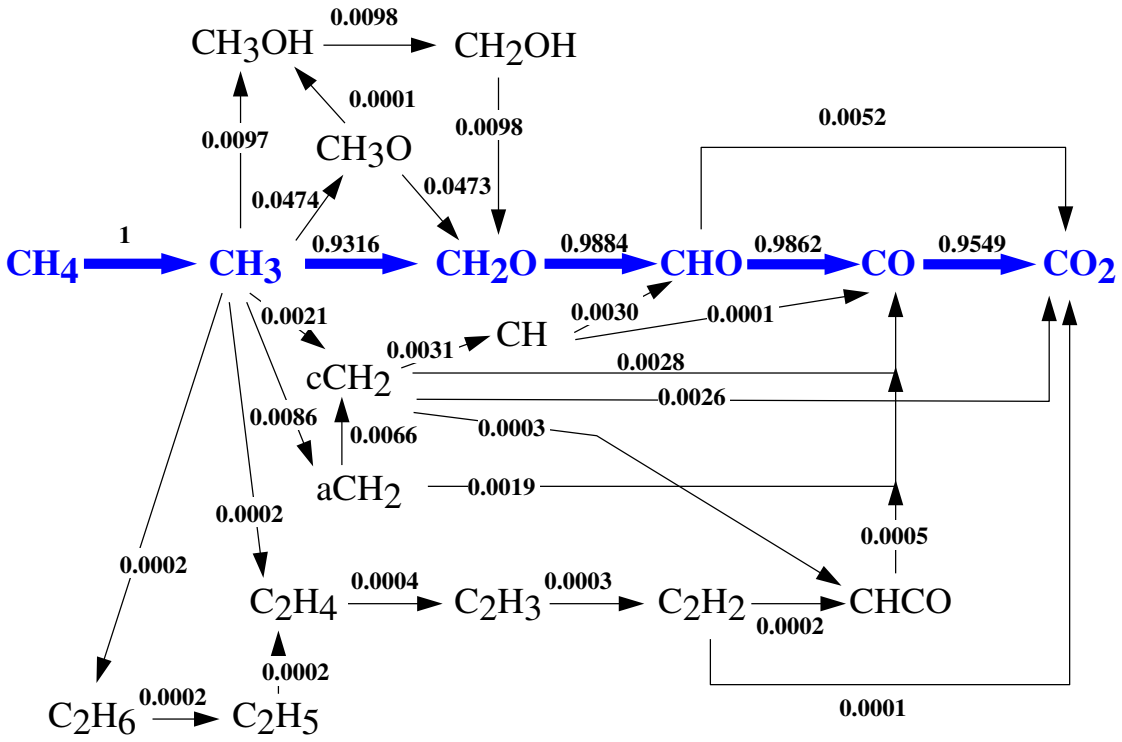

Figure 2.3.: CH_4 reaction path scheme, kindly provided by C. Frouzakis. The numbers at the arrows indicate normalized reaction rates.

species like OH, CH, CH_2O or NO can be used for LIF diagnostics. Figure 2.4 shows a selection of combustion intermediates spatially resolved along the flame front of a lean premixed CH_4 flame as well as the corresponding temperature and heat release profiles. A typical definition of the location of the flame front is the position with the highest heat release (the minimum of the heat release curve). From Figure 2.4 it can be seen that the concentration of CH peaks very close to the position of the flame front. CH can therefore be used as an indicator of the flame front (e.g. in a Bunsen flame, see Figure 1.1 or [20]). The concentration of CH_2O peaks before the reaction zone caused by the thermal decomposition of the fuel. CH_2O can hence be used as a precursor for the reaction (see also Figure 1.1 or [21]). The concentration of OH rises strongly within the flame front. OH is thus also a possible indicator for the flame front.
From the major species of CH_4 combustion (CH_4, O_2, CO_2 and H_2O) only O_2 has been shown to be useful for LIF diagnostics in flames with UV lasers [22, 23]. LIF in flames of hot CO_2 was reported by Lee et al. [24] but they found a strong temperature dependence of the LIF signal and mention the little fundamental knowledge about the interaction of

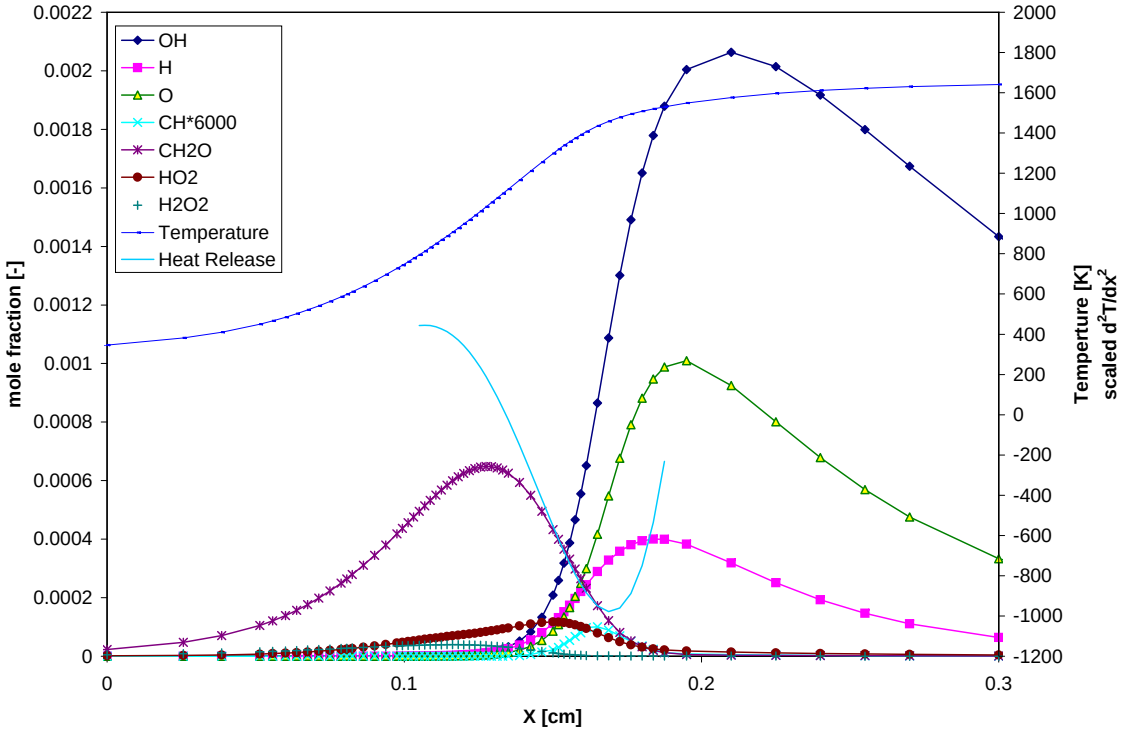

Figure 2.4.: Selected minor species in lean premixed CH_4 combustion with $\lambda = 1.67$, calculated with the GRI 3.0 mechanism [18] and the PREMIX code from the CHEMKIN package [19]. The heat release is scaled to be able to plot it on the same axis as the temperature.

hot CO_2 and UV light.
The other more stable molecules would need a higher photon energy to be excited (VUV light), which is practically impossible to apply in technical combustion processes.

2.2.2. Two-Level LIF Model

The principles of LIF can be described, strongly simplified, with a two energy level model as shown in Figure 2.5 in which the state E_1 is termed ground state and E_2 the excited state. Introducing N_1 and N_2 as the number of molecules populating E_1 and E_2, respectively, the rate equations for the temporal derivatives of the state population

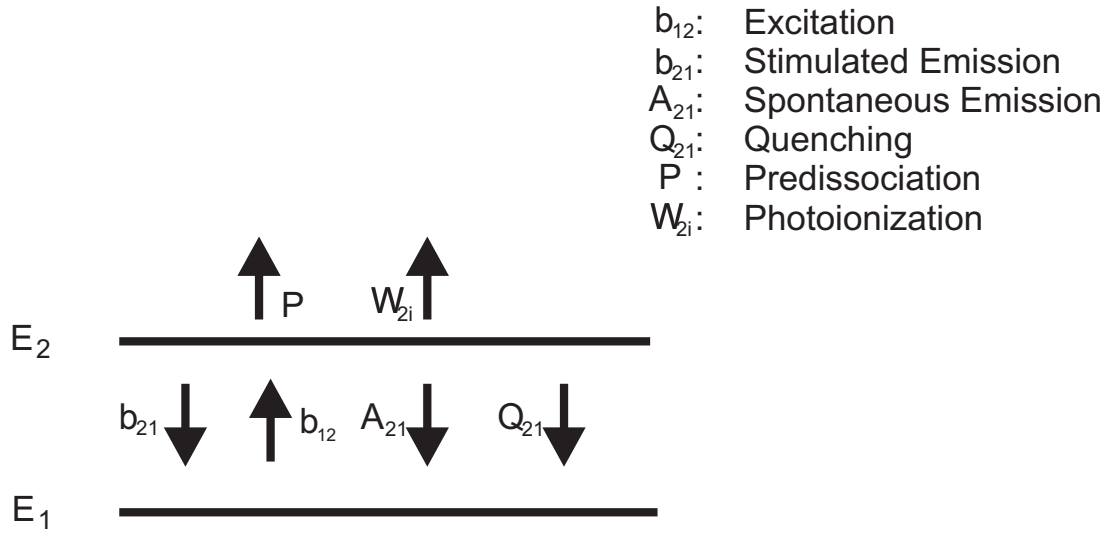

Figure 2.5.: Two Energy Level LIF Model according to Eckbreth [14].

densities can be written as

$$\frac{dN_1}{dt} = -N_1 b_{12} + N_2(b_{21} + A_{21} + Q_{21}) \tag{2.5}$$

$$\frac{dN_2}{dt} = +N_1 b_{12} - N_2(b_{21} + A_{21} + Q_{21} + P + W_{2i}) \tag{2.6}$$

with the rate constants b_{12} (excitation), b_{21} (stimulated emission), A_{21} (spontaneous emission), Q_{21} (fluorescence quenching, a collisional deactivation explained in more detail in section 2.3), P (predissociation) and W (photoionization) and the initial conditions $N_1(0) = N_1^0$ and $N_2(0) = 0$. The fluorescence signal power F is proportional to the population of the excited state N_2 and can be expressed as

$$F = C_e D_e A_{21} N_2 \tag{2.7}$$

in which C_e and D_e are constants denoting the collection efficiency (C_e), comprising e.g. the photon energy of the emitted fluorescence, the collection angle, the focal area of the laser beam, and the detection efficiency D_e, accounting for light amplification and the detection characteristics of the CCD camera.
When $A_{21} + Q_{21} + P >> b_{21}$ the system depicted in Figure 2.5 reaches a steady state during the laser pulse [14]. In the important case of low excitation rate b_{12}, which means it changes the population of N_1 only negligibly, and photoionization W is negligible LIF is termed to be in the linear regime and the fluorescence power can be expressed

proportional to the initial population N_1^0 as:

$$F = C_e D_e b_{12} \underbrace{\frac{A_{21}}{A_{21} + Q_{21} + P}}_{\varphi} N_1^0 \tag{2.8}$$

In this equation, φ denotes the fluorescence quantum yield. In the case of predissociative LIF in the linear regime, which means $P >> Q + A$, the quantum yield can be expressed as $\varphi \approx \frac{A_{21}}{P}$. The LIF signal F is then

$$F = C_e D_e b_{12} \frac{A_{21}}{P} N_1^0. \tag{2.9}$$

For all the O_2 B-X transitions investigated in this work φ is dominated by P and in the order of 10^{-7}.

2.2.3. LIF Models with more than Two Levels

In practice, the 2-level model is not sufficient to describe LIF kinetics as often collision induced rotational energy transfer (RET, see subsection 2.3.1) must be considered. To account for RET, Berg and Shackleford [25] or Lucht et al. [26] proposed to extend the two-level model into a four-level model as depicted in Figure 2.6, which they successfully used to describe saturated OH LIF measured with Q-switched Nd:YAG lasers. In this four-level model, the levels 3 and 4 are not single energetic states as levels 1 and 2, they comprise as pool or bath states an ensemble of rotational states. The de- and repopulation of levels 1 and 2 through the bath states 3 and 4 with the corresponding rate constants represent effective processes which are the result of the interaction of many state-to-state processes. A more detailed description of these state-to-state processes is usually not possible in LIF experiments, as such processes can not be resolved. On the other hand a four-level model allows a quick computation of model results which is advantageous when fitting the models to a large number of experimental data points.

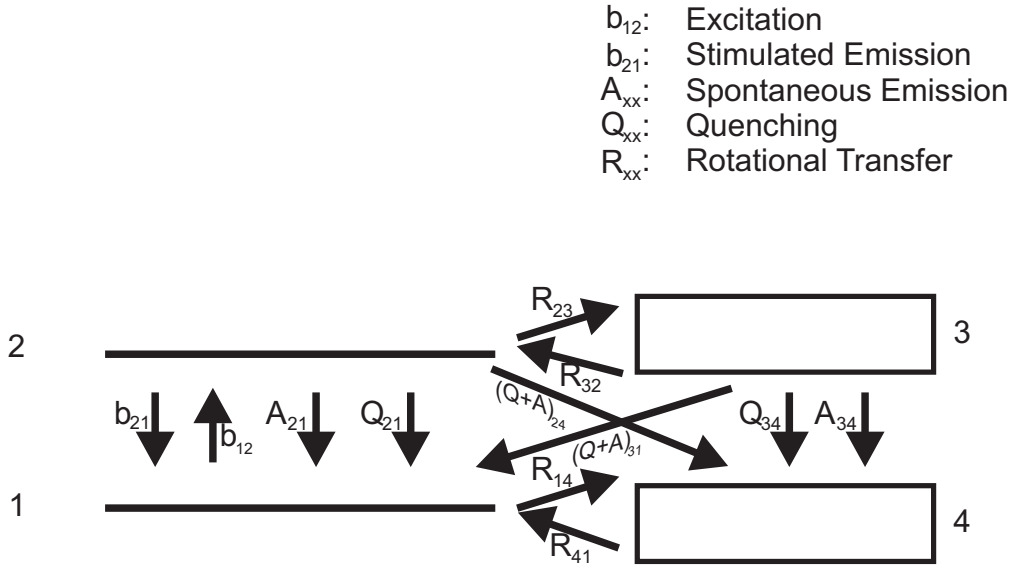

Figure 2.6.: Four-level LIF model according to Berg and Shackleford [25] and Lucht et al. [26].

The rate equations for the four-level system can be written as:

$$\frac{dN_1}{dt} = -N_1(b_{12} + R_{14}) + N_2(b_{21} + A_{21} + Q_{21}) + N_3(A_{31} + Q_{31}) + N_4 R_{41} \tag{2.10}$$

$$\frac{dN_2}{dt} = +N_1 b_{12} + N_3 R_{32} - N_2(b_{21} + A_{21} + Q_{21} + A_{24} + Q_{24} + R_{23}) \tag{2.11}$$

$$\frac{dN_3}{dt} = +N_2 R_{23} - N_3(A_{31} + Q_{31} + A_{34} + Q_{34} + R_{32}) \tag{2.12}$$

$$\frac{dN_4}{dt} = +N_1 R_{14} + N_2(A_{24} + Q_{24}) + N_3(A_{34} + Q_{34}) - N_4 R_{41} \tag{2.13}$$

The four-level model can be seen as the core description for LIF including RET, which has been adapted for different molecular systems. In this scope, for time dependent studies of OH LIF, Stepowski and Cottereau [27] have proposed a three-level model which comprises levels 1,2 and 3 from Figure 2.6. They assume for weak pumping that rotational energy transfer is fast enough to maintain the population N_1 at its Boltzmann fraction.

For planar LIF with NO Lee et al. [28] proposed a five-level model. In this model the additional fifth level acts as a sink for quenching of the upper states. Nguyen and Paul [29] showed that a five-level model for saturated O_2 LIF can be simplified to a three-level model, which is what I will use as a starting point for modeling saturated O_2 LIF in this work.

2.3. Collisional Processes Relevant for LIF in Combustion

When molecules are colliding with other molecules or atoms, they may exchange energy. By either accepting or releasing a certain amount of energy, the energetic state of the molecules changes. With the LIF technique, molecules are excited to a distinct energetic state and the fluorescence from it is analyzed. Not considering collisionally induced population changes of the LIF-involved energetic states may lead to an over- or underestimation of the recorded LIF signal. As shown by e.g. Eckbreth [14], Rothe et al. [30] or Decker [13] collisional processes may influence the LIF signal significantly in combustion environments.
One way to categorize collisional processes is to discriminate by the amount of exchanged energy (e.g. if the transferred energy is equal to the energetic separation of two rotational or vibrational states). The efficiency of a collisional process in ideal gas can be described by its effective collisional cross sections σ, so that the rate constant of the process can be calculated as:

$$Q_{coll} = n_{tot} v_{rel} \sigma \qquad \text{with} \tag{2.14}$$

$$v_{rel} = \sqrt{\frac{8 k_B T}{\pi \mu}} \qquad \text{the relative mean velocity where } \mu \text{ is the reduced mass} \tag{2.15}$$

$$n_{tot} = \frac{p}{k_B T} \qquad \text{the particle density from the ideal gas law with pressure } p \tag{2.16}$$

Especially for quantitative LIF analysis, it is important to know the rate constants for such collisional processes. I present in the coming section the important processes which are relevant for LIF applied to combustion problems.

2.3.1. Rotational Energy Transfer

The conversion from translational energy (momentum) to rotational energy (angular momentum) or vice versa and the exchange of rotational energy as the result of inelastic collisions between molecules is called Rotational Energy Transfer (RET). The theory of rotational relaxation was reviewed e.g. in Secrest [31]. This energy exchange process is of major importance to the present work, as Grinstead et al. [32] have shown that compared to the pulse duration of a typical combustion diagnostics laser in the order of $3 - 20$ ns RET of O_2 is a fast process. Thus concerning LIF measurements, RET will change population densities of the ground state and the excited state during the laser pulse and must be accounted for in quantitative LIF measurements. Nguyen and Paul [29] have shown that the saturation effect of the LIF signal in predissociative O_2 LIF is

the result of a competition between laser excitation out of the ground state and RET repopulating the ground state.

Modeling RET

The population change of a rotational level N_{J_f} resulting from rotational energy transfer can be written as:

$$\frac{dN_{J_f}}{dt} = \sum_{i \neq f} (k_{J_i \to J_f} N_{J_i} - k_{J_f \to J_i} N_{J_f}) \tag{2.17}$$

If for example $J_{max} = 100$ rotational states are considered, RET rates between every state are usually written in a state-to-state rate matrix (called relaxation matrix, in this case a 100×100 matrix). A matrix element $k_{J_i \to J_f}$ describes the rate from the initial rotational level J_i to the final level J_f. Following Brunner and Pritchard [33], models describing RET can be divided into two classes: fitting laws and scaling laws. The fitting laws are empirical functions which represent the state-to-state matrix with only a few parameters. They are often determined and verified experimentally. The scaling laws are based on a theoretical approach, they are derived from the formulation of the quantum mechanical scattering problem by applying certain assumptions to the Schrödinger equation. Due to the usually large number of free parameters, scaling laws directly are not practical to fit experimental data. I will review in the upcoming sections commonly used laws, following [33].

Scaling Laws

Under the assumption of sudden collisions, where the collision is fast compared to the rotation of the molecule, the infinite-order sudden scaling law (IOS) can be derived from the Schrödinger equation by applying certain dynamical approximations. The relaxation matrix elements from the IOS scaling law, involving a sum of products of angular momentum coupling coefficients can be written as:

$$k^{IOS}_{J_i \to J_f} = (2J_f + 1) \exp\left(\frac{E^r_{J_i} - E^r_{J_>}}{k_b T}\right) \sum_l \begin{bmatrix} J_i & J_f & l \\ 0 & 0 & 0 \end{bmatrix}^2 (2l+1) k_{l \to 0} \tag{2.18}$$

In this equation $J_>$ denotes the greater of J_i and J_f. $k_{l \to 0}$ is a set of base rate constants. The matrix in the sum is called Wigner or 3-j-symbol matrix and considers coupled angular momenta in two quantum systems. The IOS scaling law is, due to the assumptions made in its derivation, restricted to collisions where the duration of the collision is small compared to the rotational period of the molecule. Good agreement between the IOS

scaling law and experimental data has been observed in collisional systems of light atoms with molecules.
A further generalization of the IOS scaling law allows to extend the scaling relationships beyond the above mentioned restriction of sudden collisions. A factor A_J, termed adiabatic factor is introduced resulting in the energy-corrected sudden approximation (ECS) scaling law:

$$k^{ECS}_{J_i \to J_f} = (2J_f + 1)\ \exp\left(\frac{E^r_{J_i} - E^r_{J_>}}{k_b T}\right) \sum_l \begin{bmatrix} J_i & J_f & l \\ 0 & 0 & 0 \end{bmatrix}^2 (2l+1)[A_j]^2 k_{l\to 0} \tag{2.19}$$

Fitting Laws

The fitting laws are based on the assumption that the relaxation matrix elements $k_{J_i \to J_f}$ depend on the energetic difference of initial and final state: $k_{J_i \to J_f}(\Delta E_{J_i J_f})$. The oldest and widely used fitting law is the exponential gap law (EGL), proposed by Polanyi [34].

$$k^{EGL}_{J_i \to J_f} = \beta\ \exp(-\alpha |\Delta E_{J_i J_f}|) \tag{2.20}$$

In this law, α and β are the fitting parameters. Polanyi [34] has shown good agreement of this law with light molecules, but it is not suitable for heavier molecules. Attempts have been made to explain the EGL with suprisal theory (information theory), but none of them should be thought of as proving the EGL.
Koszykowski et al. [35] proposed for their comparison to experimental data, adding further parameters to the EGL yielding a so-called modified EGL (MEG).

$$k^{MEG}_{J_i \to J_f} = \alpha \left(\frac{1 + aE_{Ji}/k_B T\delta}{1 + aE_{Ji}/k_B T}\right)^2 \left(\frac{T_0}{T}\right)^N exp(-\beta \Delta E_{J_i J_f}/k_B T) \tag{2.21}$$

They have found good agreement for O_2 - O_2 and O_2 - N_2 collisions.
Another empirical correlation is the statistically based power gap law (SPG), which can be written as follows:

$$k^{SPG}_{J_i \to J_f} = \beta\ |\Delta E_{J_i J_f}/B_{rot}|^{-\alpha} \tag{2.22}$$

where B_{rot} denotes the rotational constant, and again, α and β are the fitting parameters. The SPG was successfully applied to experiments (see Brunner et al. [36]).
For N_2 - Ar collisions a combination of the SPG and EGL called the statistical exponential-

power gap law (SEPG) has been successfully applied (see Brunner et al. [36]),

$$k^{SEPG}_{J_i \to J_f} = \beta \ |\Delta E_{J_i J_f}/B_{rot}|^{-\alpha} \exp(-\alpha_2 |\Delta E_{J_i J_f}|) \tag{2.23}$$

where α, α_2 and β are the fitting parameters.

A possibility to apply the scaling laws to experimental data is to define the base rates $k_{l\to 0}$ of the IOS or ECS scaling laws (Equation 2.18, 2.19), as power law for the angular momentum, similar to the SPG

$$k^{P}_{l\to 0} = a[l(l+1)]^{-\gamma} \tag{2.24}$$

where a and γ are the fitting parameters. The fitting laws resulting from this combination are termed IOS-P and ECS-P, respectively. When using a combination of power law and exponential law to define the base rates $k_{l\to 0}$:

$$k^{EP}_{l\to 0} = a[l(l+1)]^{-\gamma} \exp\left(\frac{-l(l+1)}{l^*(l*+1)}\right) \tag{2.25}$$

with fitting parameters a, γ and l^*, consequently, the fitting laws are termed IOS-EP and ECS-EP.
Knopp et al. [37] have introduced an angular momentum-based scaling (AECS) law, in which the $k_{J_i \to J_f}$ scale with $\sqrt{\Delta E}$ instead of ΔE, as in the energy scaling laws.
Describing collisional processes, it is common to all the RET model approaches that they scale linearly with the pressure. One important aspect to note is that there are no clear rules and indications for which system which scaling or fitting law is preferred. Steinfeld et al. [38] have shown for N_2 that ECS-EP represents their data better than EGL, SEPG, IOS, IOS-EP or ECS-P. For a wide pressure range Koszykowski et al. [35] and Seeger et al. [39] have found that MEG describes N_2-N_2 and N_2-O_2 collisions best. Knopp et al. [37] have found for N_2 collisions their AECS model superior compared to ECS-EP and ECS-P. Regarding this work, the differences between the model approaches can assumed to be negligible and therefore all model approaches are acceptable.

2.3.2. Vibrational Energy Transfer

The conversion from translational energy to vibrational energy or vice versa as well as the exchange of vibrational energy as the result of inelastic collisions between molecules is called Vibrational Energy Transfer (VET). The theory of vibrational relaxation was reviewed e.g in Rapp and Kassal [40], Kneba and Wolfrum [41], Secrest [31], Lambert

[42] and Capitelli et al. [43]. In their work, Capitelli et al. [43] point out that VET is a slow process compared to RET ($\tau_{VET} >> \tau_{RET}$). For the scope of this work it is important to know how the characteristic timescale of VET compares to the laser pulse duration (τ_{VET} vs τ_{laser}).
According to Capitelli et al. [43], three different mechanisms of VET need to be distinguished. The analysis is based on the harmonic oscillator model, which describes vibrational relaxation well for low vibrationally excited levels.

- Vibrational to Translational (VT) energy transfer.
  The population change of a vibrational level N_n can be written as, similarly to Equation 2.17 for RET

$$\frac{dN_n}{dt} = Z \sum_{m \neq n} (P_{mn} N_m - P_{nm} N_n) \tag{2.26}$$

  where Z denotes a collision frequency and P the transition probability. The collision frequency Z is calculated as

$$Z = 2d^2 n_{tot} \sqrt{\frac{2\pi k_B T}{\mu}} \tag{2.27}$$

  where d is referred to the diameter of an atom or molecule, n_{tot} is the total number of particles and μ is the reduced mass of the collisional partners. This notation with the collision frequency and probabilities is advantageous when probabilities can be calculated and is linked to the notation in Equation 2.17 by the calculation of the collision frequency Z in Equation 2.27 in which the collisional cross section is set to $\sigma_{coll} = \frac{\pi d^2}{4}$. Assuming a Maxwellian velocity distribution and considering the principle of detailed balance, the probabilities are related as

$$P_{nm} e^{-\frac{E_n}{k_B T}} = P_{mn} e^{-\frac{E_m}{k_B T}}. \tag{2.28}$$

  Typically, only single-quantum transitions need to be considered [43] with probabilities

$$P_{n+1,n} = (n+1) P_{10} \tag{2.29}$$

  in which P_{10} denotes the probability of the transition $N_1 \rightarrow N_0$. By defining a total vibrational energy as $E_{vib} = \sum n E_{10} N_n$ and considering Equations 2.28 and 2.29, Equation 2.29 yields the energy relaxation equation with the VT relaxation

time τ_{VT}

$$\frac{dE_{vib}}{dt} = -\frac{E_{vib} - E^0_{vib}}{\tau_{VT}} \tag{2.30}$$

which was derived by Landau [44].

- Vibrational to Vibrational (VV) energy transfer between identical molecules. Considering VV exchange, Equation 2.26 must be extended to

$$\frac{dN_n}{dt} = \\ Z \sum_{m \neq n} (P_{mn} N_m - P_{nm} N_n) + \frac{Z}{\sum_{m=0} N_m} \sum_{m,s,l} (P^{sl}_{mn} N_s N_m - P^{ls}_{nm} N_l N_n) \tag{2.31}$$

in which P^{sl}_{mn} is the probability of VV exchange in a collision after which two molecules in the initial states m and s transfer to the final states n and l. Again, from the principle of detailed balance, the probabilities of VV exchange are related through the expression

$$P^{ls}_{nm} e^{-\frac{E_l + E_n}{k_B T}} = P^{sl}_{mn} e^{-\frac{E_s + E_m}{k_B T}}. \tag{2.32}$$

According to Capitelli et al. [43] there are usually two different relaxation timescales for which can be said:

$$\tau_{VV} \approx \frac{1}{Z P^{01}_{10}} << \frac{1}{Z P_{10}} \approx \tau_{VT}. \tag{2.33}$$

- Vibrational to Vibrational energy transfer between different types of molecules (VV') .
In mixtures of diatomic gases energy exchange caused by collisions between molecules of different types needs to be considered, which can assumed to be independent from the above mentioned VT and VV exchange. The population change caused by VV' exchange can be written as

$$\frac{dN^A_n}{dt}_{VV'} = \frac{Z_{AB}}{\sum_n N^B_n} \sum_{m,s,l} (P'^{sl}_{mn} N^B_s N^A_m - P'^{ls}_{nm} N^B_l N^A_n) \tag{2.34}$$

in which Z_{AB} is the mean number of collisions of a molecule A with molecules B. The principle of detailed balance relates the probabilities of VV' exchange as

$$P'^{ls}_{nm} e^{-\frac{E^B_l + E^A_n}{k_B T}} = P'^{sl}_{mn} e^{-\frac{E^B_s + E^A_m}{k_B T}}. \tag{2.35}$$

For a single-quantum VV' exchange between two harmonic oscillators for which

$$E_{10}^{A} > E_{10}^{B}; \quad E_{10}^{A} < 2E_{10}^{B} \tag{2.36}$$

the following inequality according to Capitelli et al. [43] can be assumed

$$\tau_{VV}^{A}, \tau_{VV}^{B} << \tau_{VV'}^{A}, \tau_{VV'}^{B} << \tau_{VT}^{A}, \tau_{VT}^{B}. \tag{2.37}$$

Concerning predissociative B-XO_2 LIF in flames, Sick et al. [45] have shown that neither VV, VV' or VT exchange can be measured in the excited state. This is not unexpected as the excited state is dominated by fast predissociation ($\tau_{pred} << \tau_{VV}, \tau_{VV'}, \tau_{VT}$) and thus VET of the excited state can be neglected. Ground state VET of O_2 is important to the process of ozone formation in the Earth's atmosphere and has thus been investigated by the atmospheric chemistry community e.g by Coletti and Billing [46]. Their theoretical and experimental results show that O_2 VV and VT exchange is slow compared to the laser pulse duration ($\tau_{laser} << \tau_{VV}, \tau_{VT}$).

VET in Collisions with Oxygen Atoms

In the present work O_2 molecules are photo-dissociated caused by the laser excitation. Collisions of molecular O_2 and O atoms of the form

$$O_2(v'') + O \rightarrow O_2(v') + O \tag{2.38}$$

are known to be efficient in multi-quantum VT vibrational energy exchange, because a stable intermediate complex O_3 can be formed. Esposito and Capitelli [47] investigated this relaxation process in detail. Their results show that the above mentioned collision (Equation 2.38) can cause faster relaxation of O_2 compared to molecular collisions. With respect to the present work, an upper bound of this vibrational relaxation process can be estimated by assuming that all O_2 molecules of a lower state (e.g. $v'' = 6$) are dissociated into O atoms. Considering the rate constants of [47], the resulting VET rates are due to the low concentration of O about four orders of magnitude smaller compared to RET rates.

Considering these results and Equation 2.37, during a laser pulse all O_2 VET can be neglected in this work.

2.3.3. Quenching

Fluorescence quenching describes the effect that the energy of an excited molecule is quickly exchanged with other molecules via collisions and afterwards released into kinetic or internal energy of the collisional partners instead of fluorescing. In contrast to RET or VET which describe energy exchange within an electronic state, quenching relates to an energy exchange in which the final state of the electronically excited molecule is the electronic ground state. I will discuss two quenching models which have been reported in combustion diagnostics literature and are experimentally supported.

Collisional-Complex Model

In this model, the collision is treated as a reaction of the excited molecule A^* with a collisional partner M which deactivates A^* into the ground state [48] :

$$A^* + M \rightarrow A + M + E_{kin} \tag{2.39}$$

When A^* and M approach each other attractive interactions between them result in the formation of a complex or collision pair $A^* \cdots M$ which either falls back to A^* and M or dissociates into A and M with increased kinetic energy. The reaction path can be written as

$$A^* + M \rightarrow A^* \cdots M \rightarrow A + M \tag{2.40}$$

The collisional complex model was successfully used by Fairchild et al. [48] to describe fluorescence quenching of $A^2\Sigma^+$ OH radicals in measurements at elevated temperature (1100 K) and by Holtermann [49] to describe quenching of single rotational levels of SO_2.

Harpooning Model

In this model, an excited molecule A^* is assumed to form an intermediate ion pair with the collisional partner M, $A^+ + M^-$ by an electron transfer. The corresponding ion potential function crosses the potential functions of the electronic ground state and excited state (sometimes this model is also called "curve-crossing model" [50]). The potential energy functions are schematically shown in Figure 2.7 When a collision happens, A^* can change to the ionic potential with a probability $1 - P_x$ and subsequently change to the ground state potential with the probability $1 - P_y$ or stay on each potential with the probabilities P_x and P_y, respectively. For a quenching process, the initial electron jump occurs at the intersection point "x" in Figure 2.7 and a subsequent electron transfer at intersection point "y". Therefore, "x" and "y" are called entrance and exit channels for

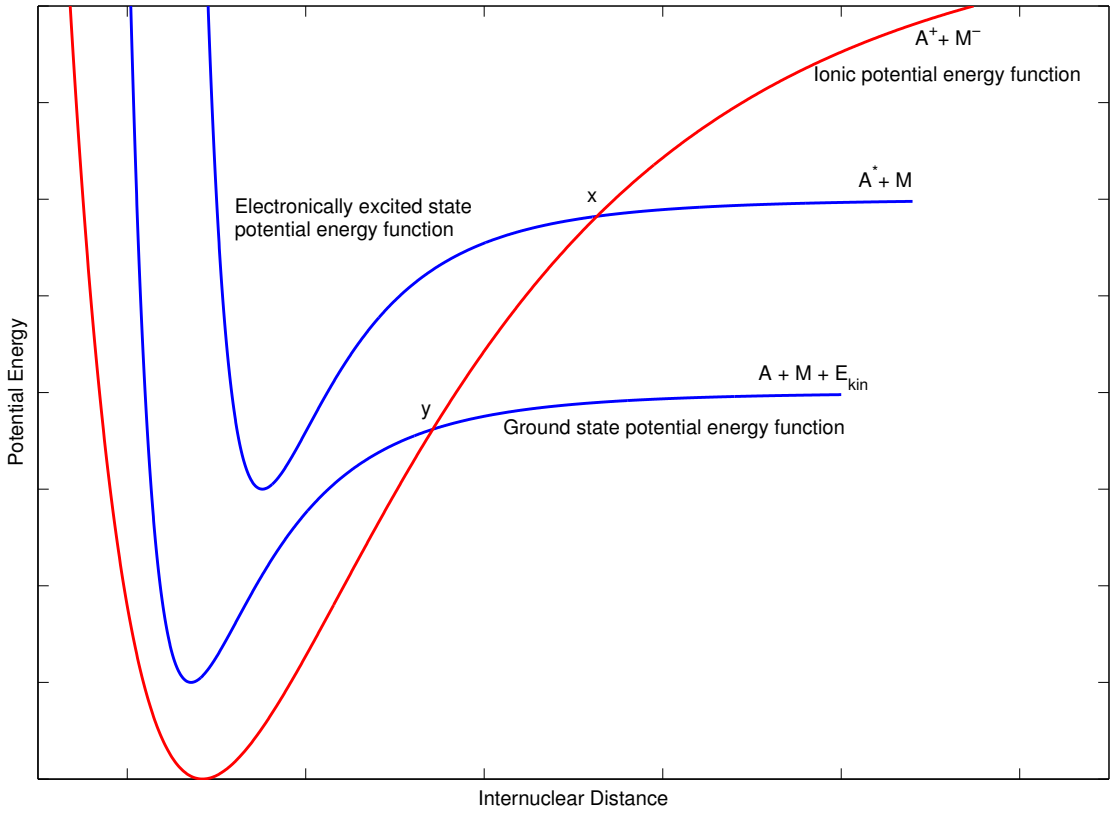

Figure 2.7.: Schematic of the involved potential energy functions relevant for the harpooning quenching model after Decker [13].

electronic quenching. The probability of quenching P_Q can then be defined as [50]

$$P_Q = (1 - P_x)(1 - P_y)/[1 - P_y(1 + P_x)/2]. \tag{2.41}$$

With this model, Paul et al. [50] have found good agreement to measurements of NO fluorescence and have determined quenching cross sections for collisions between NO and O_2, CO_2, H_2O, He, Ne, Ar, CH_4, CF_4, H_2 and C_2H_6 at various temperatures.
Their results point to an issue related to quantitative LIF applications in combustion. Large problems in determining the quenching rate constants arise from the fact that these rate constants depend on the pressure and the composition of the collisional partners. This indicates that for an accurate quantitative interpretation of a LIF signal, the local species composition and the pressure should be measured simultaneously with the LIF signal. A possibility to avoid the exact determination of Q is to use excited states which are strongly predissociative, so that $P >> Q$ and therefore quenching can be neglected

[14]. This is usually assumed for the B-state of O_2 (e.g. Andresen et al. [23]). Despite that, Sick et al. [45] have reported quenching cross sections which are comparable to P only slightly above atmospheric pressure. I will discuss this topic in chapter 6.

2.4. Saturation of LIF

Saturation of LIF occurs when the laser intensity is large enough, so that the LIF signal becomes independent of the laser intensity. From the two-level model introduced in section 2.2 a strategy to avoid quenching corrections can be derived which is linked to saturation of LIF. In the case of saturation, the LIF signal is maximized and quenching becomes unimportant compared to excitation and stimulated emission. This can be derived as follows.
The LIF signal depends on the excitation rate b_{12} which is proportional to the laser intensity I

$$b_{12}(\nu) = \frac{N_1 B_{12} I}{c} \int g(\nu - \nu_0) h(\nu - \nu_l) d\nu. \tag{2.42}$$

The integral in this equation is the overlap integral between the absorption line $g(\nu)$ and the laser line $h(\nu)$. The determination of this integral as well as the calculation of the excitation rate are discussed in detail in subsection 4.3.3. For the two level LIF model (subsection 2.2.2), a saturation intensity can be defined as [14]

$$I_{sat} = \frac{(A_{21} + Q_{21})c}{B_{12} + B_{21}} \tag{2.43}$$

When employing a laser intensity $I >> I_{sat}$, the fluorescence signal can be calculated independent from the excitation rate as [14]

$$F = C_e D_e \frac{B_{12}}{B_{12} + B_{21}} A_{21} N_1^0. \tag{2.44}$$

Saturated LIF measurements to determine concentrations in flames have been conducted with C_2 [51, 52], CH [51, 53], CN [53], OH [54–57] as well as with MgO [58] and results are reviewed by Schofield [59] and Crosley [60] . As mentioned by Altkorn and Zare [61], despite the low dependence on fluorescence quenching and the maximized LIF signal intensity, saturated LIF experiments have some other complications. In practice it is challenging to achieve complete saturation, due to e.g. non-uniformities of the spatial and temporal beam profile of the laser beam. When using extremely high laser intensities, the possibility of laser-induced chemistry [62, 63] or ionization must be considered [61] and extrapolations to complete saturation must be carried out when it can not be

achieved.
Especially in low-pressure flames [64] when VET and RET are negligible, saturated LIF was successfully applied for concentration measurements. An alternative approach for higher pressure flames and for time-varying applications is to measure LIF in the linear regime and measure major quenching species to correct for quenching.
Another, rather practical aspect of saturations needs to be considered. It may be impossible to lower the laser intensity so strong that the linear regime of LIF can be ensured. This is related to the detection efficiency of the experimental setup. In this case partial saturation is observed, which is a deviation of a linear LIF signal dependence on laser intensity. In this case vibrational and especially rotational relaxation need to be considered as we will see later in this work. Depending on the properties of the molecule used for LIF experiments, there are different mechanisms which can cause partial saturation (this is the type of saturation that I will consider in the remainder of this work). E.g. for the NO molecule, saturation arises when the population of the excited state is large, so that excitation and stimulated emission are dominant for the population variation of the ground and excited state. RET and quenching of the excited state are important processes to depopulate the excited state and allow more molecules to be excited [28].
For the case of O_2 LIF with transitions of the Schumann-Runge system, the excited state will never be strongly populated due to the high predissociation rates. In this case, the non-linear dependence arises from a different mechanism. When laser pumping is strong, so that the ground state population differs strongly from its equilibrium value, RET refills the ground state and RET is the limiting factor [65].

2.5. Laser Diagnostics in Combustion

Since the introduction of laser systems, the research field of laser diagnostics in flames has steadily grown. Eckbreth [14] gives an extensive survey of the topic, I will briefly mention some important aspects. Optical laser techniques offer a number of significant improvements compared to physical probing methods such as thermocouples [14, 66], which have been traditionally employed in combustion research to investigate and characterize flame phenomena. The intrusion of physical probes can severely alter the flame behavior and thus change the properties they are supposed to measure. In many practical applications, the flames are stabilized by flow recirculation and the presence of a probe will influence the flow field. Newly introduced recirculation areas may act as flameholders itself. The issue of probe survival the high temperatures dictates the physical robustness of the probes which increases the chance of perturbation. Also physical probes are generally limited in spatial and temporal resolution. Remote measurements such as gas sampling can only measure chemical composition far away from the sampling location and at very different conditions. Optical laser techniques circumvent disadvantages of physical probes. They are almost always non-perturbing and allow for *in-situ* measurements, which makes them ideally suited for measurements in recirculation zones, boundary layers and confined locations as combustion chambers of internal combustion engines or gas turbines. Species concentrations or temperatures are measured directly without the need of uncertain conversion assumptions. Also, laser techniques provide a high spatial and temporal resolution. Drawbacks of laser techniques include the requirement of optical access of the dedicated measurement volume which is not always given and the fact that no single laser technique is capable of measuring all species and the temperature simultaneously. Also, laser spectroscopic techniques are best applicable to small molecules (with less than 6 atoms). For larger molecules spectroscopy is often very complicated depending on the symmetry of the molecule and spectral signatures may be very similar (e.g. in polycyclic aromatic hydrocarbons). Although the single components required for laser based techniques are commercially available (lasers, detectors, spectrographs, lenses, filters, etc.), setting up a dedicated laser diagnostic technique to an experiment requires large efforts and a fairly high level of operator skill.

2.5.1. Typical Laser Diagnostic Methods in Combustion

In this section, I will briefly discuss some of the important laser diagnostic methods besides LIF and their very basic working principles. Detailed information can be found in books of Eckbreth [14] and Raffel et al. [67] as well as in the review of Abbiss et al. [68]

Laser Doppler Anemometry LDA

A point measurement of the flow velocity can be conducted with Laser Doppler Anemometry (LDA) [68]. The method is based on the principle of Doppler shift. The frequency of incident radiation, usually realized with a laser, scattered by an object moving relative to the radiation source is shifted depending on the velocity and the scattering geometry. The scattered frequency is recorded yielding the velocity information. A schematic of an LDA setup is shown in Figure 2.8

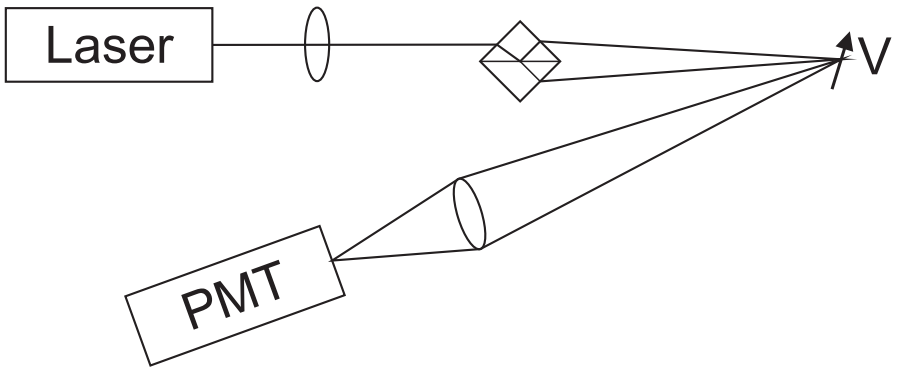

Figure 2.8.: Basic Laser Doppler Anemometry Setup, after Abbiss et al. [68].

Particle Induced Velocimetry PIV

To measure flow field velocities in 2-D, especially turbulent flow fields, Particle Induced Velocimetry (PIV) has proven to be a successful method since it was mentioned in 1994 by Pickering and Halliwell [69] and Adrian [70]. The method of PIV and modern applications are reviewed in Raffel et al. [67]. For PIV measurements, usually tracer particles are added to the flow. These particles are illuminated typically with a laser sheet through the flow at least twice within a short time interval. The light scattered by the particles is recorded by a CCD camera. A schematic of a PIV setup in shown in Figure 2.9. With post processing algorithms, the displacement of the particles in the images between the light pulses can be determined, resulting 2-D flow field maps as shown in Figure 2.10.

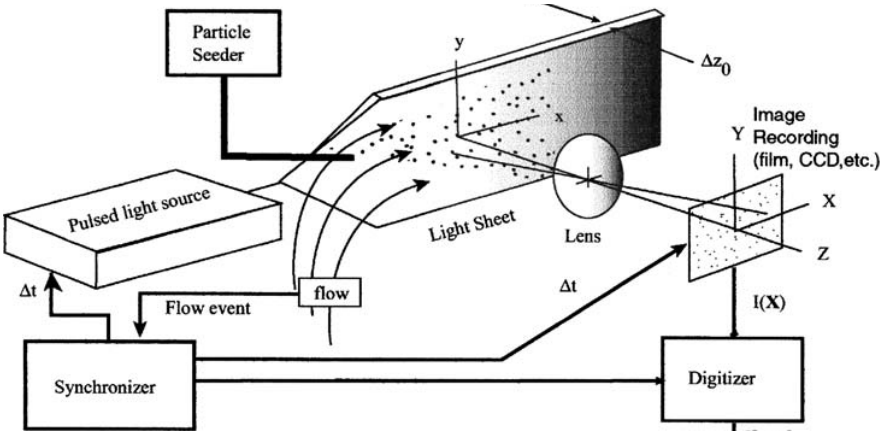

Figure 2.9.: PIV Setup, taken from Adrian [71].

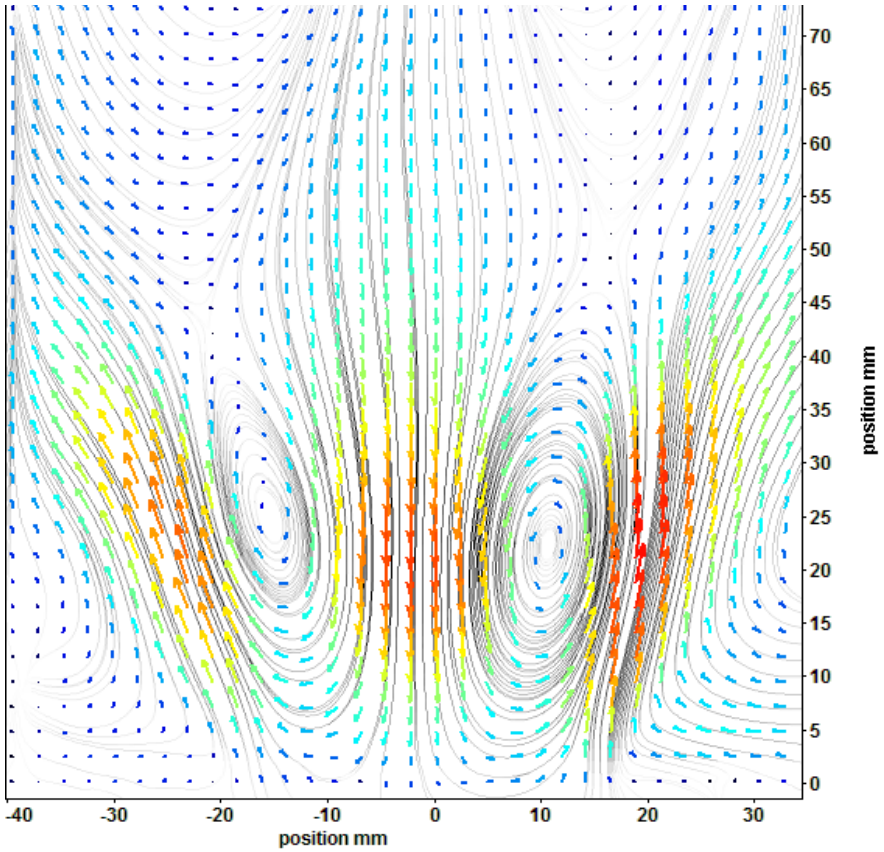

Figure 2.10.: PIV measurement result taken at the swirl burner at PSI by A. Denisov. Color code and arrow length indicate absolute gas velocity.

Spontaneous Raman and Rayleigh Scattering

In gas phase and all other transparent phases, spontaneous Raman scattering is the result of inelastic collision processes between photons and molecules. Rayleigh scattering is the analogous elastic process. A schematic of the involved energetic states for Raman and Rayleigh scattering processes is depicted in Figure 2.11. In combustion diagnostics,

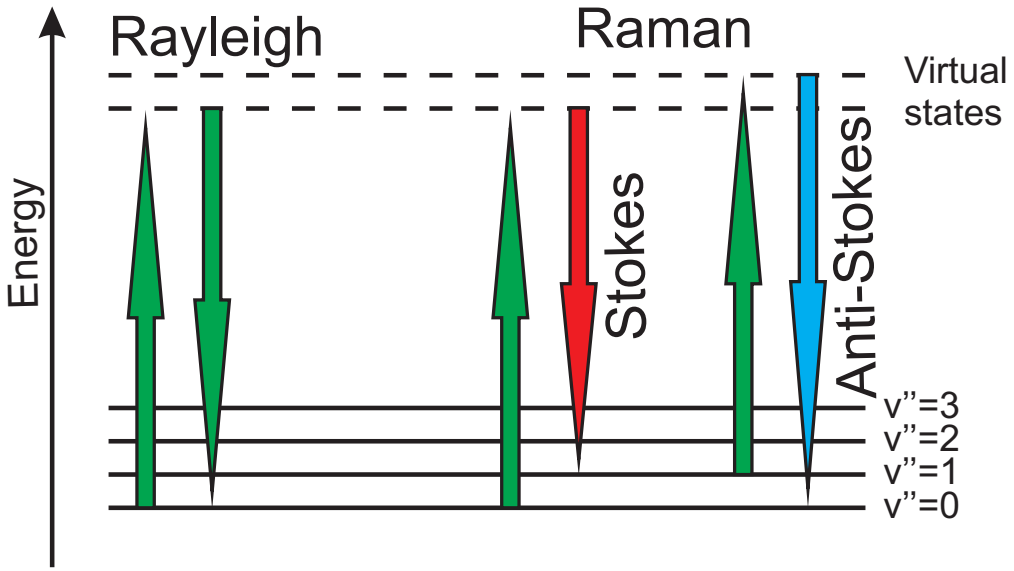

Figure 2.11.: Schematic of the in Raman and Rayleigh scattering methods involved energetic states.

Raman scattering is used to measure concentrations of species, which was pioneered by Lapp and Penney [72] and Lederman [73]. The scattering is a non-resonant process and can thus be operated at any wavelength. Visible and UV wavelengths are favored, because the strength of the scattering scales as the fourth power of the scattered frequency. The inelastic collision causes a frequency shift of the incident radiation while the corresponding energetic difference is either provided by the molecule (anti-Stokes) or absorbed (Stokes). Thus, the frequency shift depends on the molecule and Raman scattering techniques allow to detect many species simultaneously which is shown for flames by e.g. Starner et al. [74], Masri [75] or Hassel et al. [76]. The intensity of the scattered signal is dependent on the Raman cross section of the molecule but independent is from the surrounding gas composition and unaffected by collisional quenching. Absolute calibration can be achieved by a comparison of the scattered light signal from the species of interest to the one of N_2 as the cross sections for N_2 and other combustion

species are known. Cross sections of Raman scattering are usually very small, so that high laser intensities are required.
Rayleigh scattering is significantly stronger and can in specialized situations allow measurements beyond the capabilities of Raman scattering. But as an elastic process, the wavelengths of the incident and scattered light are identical and hence, not specific to the molecule causing the scattering. Thus, Rayleigh scattering can only be used to measure total number densities. Complications in Rayleigh diagnostics arise from Mie scattering and laser reflections, which allow its application only in particle free and reflection free environments.

Coherent Anti-Stokes Raman Spectroscopy CARS

By searching for a combustion diagnostics method which provides stronger signals than spontaneous Raman scattering Regnier [77] as well as Moya et al. [78] provided the impetus for Coherent Anti-Stokes Raman Spectroscopy (CARS). At atmospheric pressures CARS signals are generally orders of magnitude larger compared to the ones of spontaneous Raman. Additionally, CARS radiation emerges as a coherent beam allowing to easily capture the entire signal. In contrast to Raman or Rayleigh scattering techniques, CARS is a non-linear process. A schematic of the CARS involved processes is shown in Figure 2.12. Usually, laser beams with frequencies ω_1 and ω_2 are geometrically mixed with lenses to generate the phase-matched coherent CARS signal $\omega_3 = 2\omega_1 - \omega_2$. ω_1 is called the pump laser and ω_2 the Stokes laser, because it downshifts the frequency of the molecule being probed. Recent developments are hybrid femtosecond/picosecond CARS techniques for high-speed thermometry in unsteady high-temperature flames [79–81].

2.5.2. Typical LIF Applications in Flames

Flame front visualization

Planar LIF with the OH radical (e.g. [82–85]) or the CH_2O molecule [21], both intermediate combustion species, has often been applied to identify the spatial position of the flame front. Figure 2.13 shows a planar OH LIF image, taken by Y.-C. Lin at PSI. As mentioned in subsection 2.2.1 the OH radical concentration has the steepest increase in the flame front and peaks slightly after the flame front. The OH concentration gradually decreases behind the flame front. Thus, with OH LIF a coarse definition of the flame front can be made with the appearing signal. A more precise definition of the flame front requires post-processing. Boxx et al. [86] calculate the spatial derivative of the LIF signal and locate the steepest gradient to determine the flame front. Daniele et al. [83]

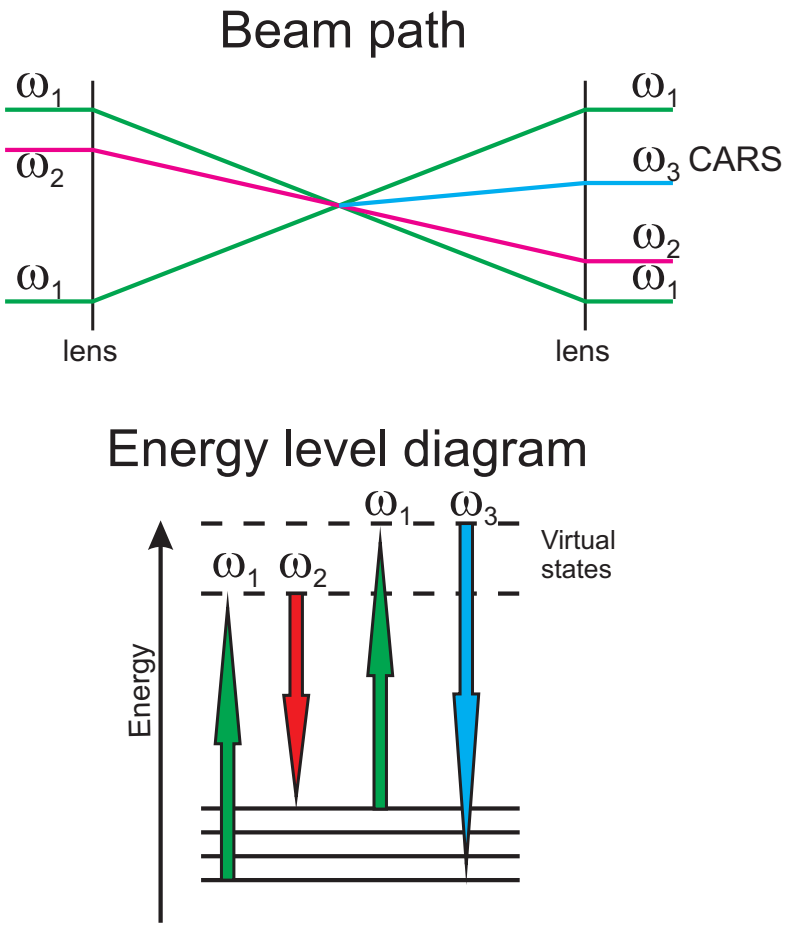

Figure 2.12.: Schematic of CARS spectroscopy, after Eckbreth [14].

use a laser intensity normalized threshold post processing algorithm for the flame front definition.

Concentration Measurements

For LIF in the linear regime, the fluorescence signal can be calculated according to Equation 2.8. Without strong pressure and concentration variations, the fluorescence signal $F \propto N_1^0$ as

$$F = \underbrace{C_e D_e b_{12} \frac{A_{21}}{A_{21} + Q_{21} + P}}_{\text{constant}} N_1^0 = C N_1^0 \tag{2.45}$$

With a calibration measurement the proportionality constant C can be determined (e.g for major combustion species with Raman spectroscopy as shown by Nguyen et al. [87]) and F can be used to indicate the concentration of N_1^0.

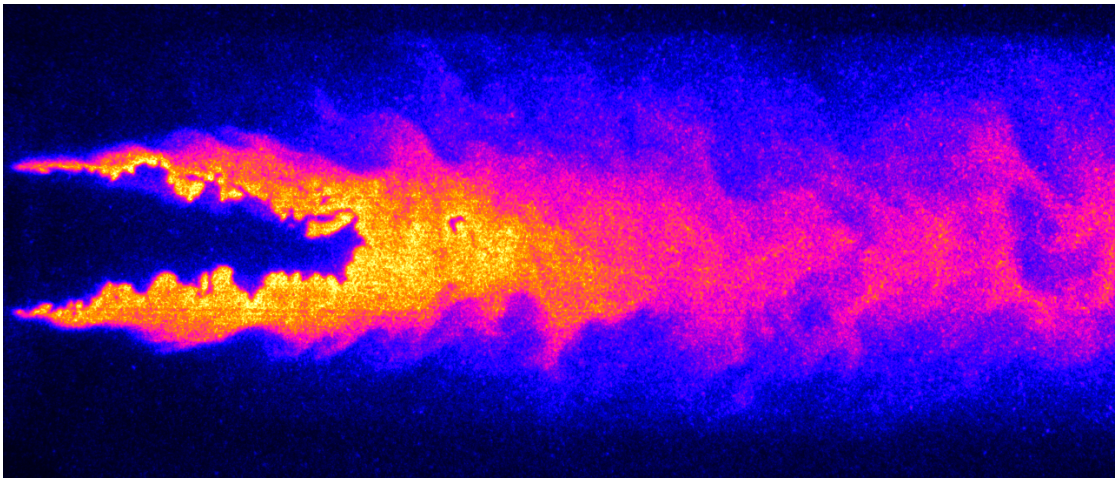

Figure 2.13.: Flame front visualization with OH LIF in turbulent H_2 combustion, taken by Y.-C. Lin at the turbulent premixed burner at PSI. The fuel/air mixture flows from left to right.

A second approach to measure the concentration of a species is to use saturated LIF. As shown in section 2.4 when $I >> I_{sat}$ can be assumed for the entire dedicated measurement region

$$F = \underbrace{C_e D_e \frac{B_{12}}{B_{12} + B_{21}} A_{21}}_{\text{constant}} N_1^0 = C N_1^0. \tag{2.46}$$

Figure 2.14 shows as an example 2-D measurements of relative OH concentration as reported by Schäfer et al. [54].

One-Line Thermometry

Seitzman et al. [88] have introduced a single-laser and single-camera technique to determine the temperature dependence of the LIF signal assuming the linear regime ($I << I_{sat}$, Equation 2.45). In their approach, they seed the flame with a tracer molecule. The initial population N_1^0 of a rotational state of the trace molecule can be related to the total number density N

$$N_1^0 = f_1^{rot}(T) N \chi_{seed} \tag{2.47}$$

in which f_1^{rot} denotes the rotational Boltzmann fraction and χ_{seed} the mole fraction of the seeded species. For a non-reacting seeding molecule, its mole fraction is constant throughout the flame and by assuming that the quenching cross sections do not depend

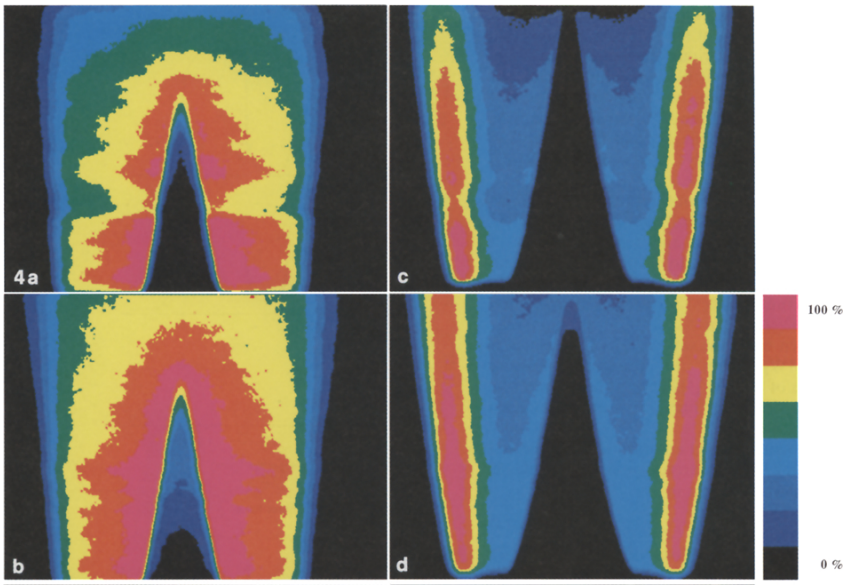

Figure 2.14.: Relative OH concentration in the flame of a laminar burner taken from Schäfer et al. [54]. Plots a and b depict lean premixed flames with $\phi = 0.93$ while plots c and d depict rich premixed flames with $\phi = 1.63$. The laser energy I is larger in plots b and d (200 mJ/pulse compared to 7 mJ/pulse in plots a and c) and not affected by absoption.

on the temperature the fluorescence signal F can be written as

$$F \propto \frac{f_1^{rot}(T)}{\sqrt{T}} \tag{2.48}$$

With a known boundary condition, they could determine instantaneous absolute temperature fields in a fuel-lean CH_4/air flame with NO LIF as shown in Figure 2.15. NO is strictly speaking not a non-reacting molecule as it reacts in the flame front. But in lean flames, the O_2 excess leads to a reappearence of NO in the hot exhaust.

Two-line thermometry

Another approach to conclude the temperature with LIF is to compare the fluorescence from two different (e.g. two ro-vibronic) transitions of a species. When taking the ratio of the fluorescence signals the constants cancel each other and it can be written as

$$\frac{F_{v_1}}{F_{v_2}} = \frac{N^0_{v_1}}{N^0_{v_2}}(T). \tag{2.49}$$

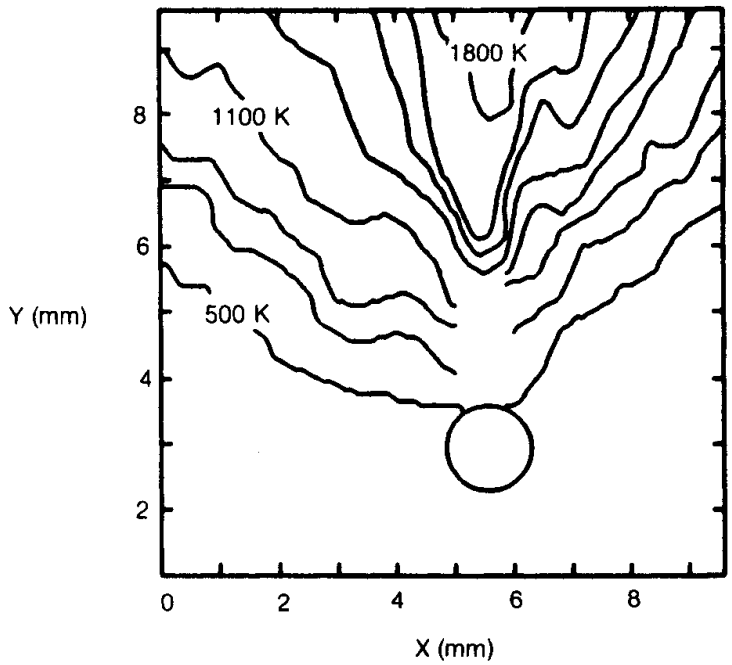

Figure 2.15.: 2-D Thermometry with NO LIF in a rod stabilized fuel-lean CH_4/air flame, taken from Seitzman et al. [88]. Depicted are isotherms.

As for the one-line thermometry when assuming a Boltzmann distribution the initial populations are only dependent on the temperature. The ratio of the fluorescence signal can be directly related to an absolute temperature, there is no calibration measurement or boundary condition needed. 2-D measurements of the temperature in a CH_4/air flame are shown in Figure 2.16.
A further development for thermometry is so-called multi line thermometry described by Bessler and Schulz [90] and Denisov et al. [91]. Instead of using just two lines, the emission of several lines (order of 10) can be used to increase the accuracy of the temperature measurement. The method is based on spectral fitting which requires precise spectral knowledge about the excited species. This is the case for the NO molecule [92]. Figure 2.17 shows temperature maps measured by A. Denisov at PSI.

2.6. O_2 Spectroscopy in Flames

Since the mid 1980s several groups worked on the application of O_2 LIF in combustion diagnostics.
Lee et al. [93] reported planar laser-induced fluorescence images of O_2 in premixed CH_4/air Meker burner flames. They used an ArF laser to excite transitions of the

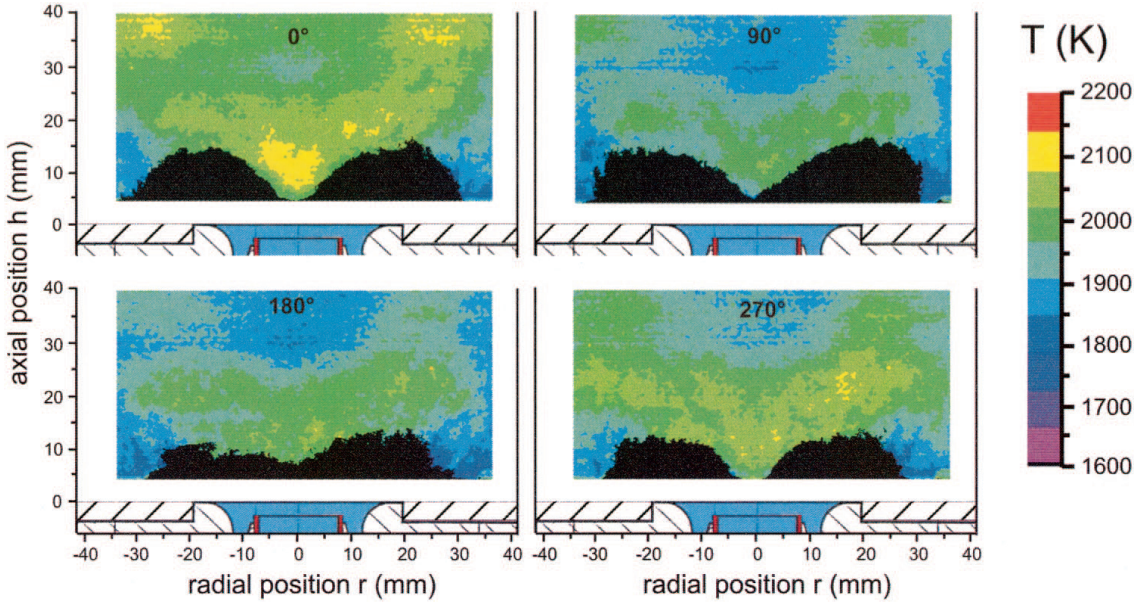

Figure 2.16.: Phase-locked 2-D thermometry with OH of a swirl flame in a turbine model combustor at atmospheric pressure, taken from Giezendanner-Thoben et al. [89]. Unusable measurement regions are marked in black.

Schumann-Runge system of O_2 at 197 nm. They pointed out that the fluorescence yields are large enough for unsteady combustion when strongly focussing the high energy beam of the ArF laser. They also mentioned that the attenuation of the ArF laser in air must be considered.

Goldsmith and Anderson [94] reported high-resolution excitation spectra of the Schumann-Runge system, which they recorded with a 1-D diode array. They used a tunable dye laser system to generate UV light around 200 nm. From their data it can be seen that the low laser energy output of the dye laser system (200 µJ/pulse) compared to the ArF laser of [93] (300 mJ/pulse) does not allow for single pulse measurements.

Lee et al. [95] introduced a method to measure the temperature of heated air flows by exciting transitions of the Schumann-Runge system of O_2 with an ArF laser. They determined the temperature by comparing the measured LIF signal strength to theoretical calculations of the temperature-dependent rotational ground state population to which the LIF signal is proportional. They list explicitly the main advantages of LIF with O_2 compared to other species (e.g Na, NO, CH, CO) used for LIF: it is stable to high temperatures and naturally abundant in many practical applications.

Andresen et al. [23] discussed that high-power excimer lasers are suitable for temperature measurements in combustion environments for LIF with O_2, OH and H_2O. They proposed a two-line thermometry method, in which the temperature can be concluded

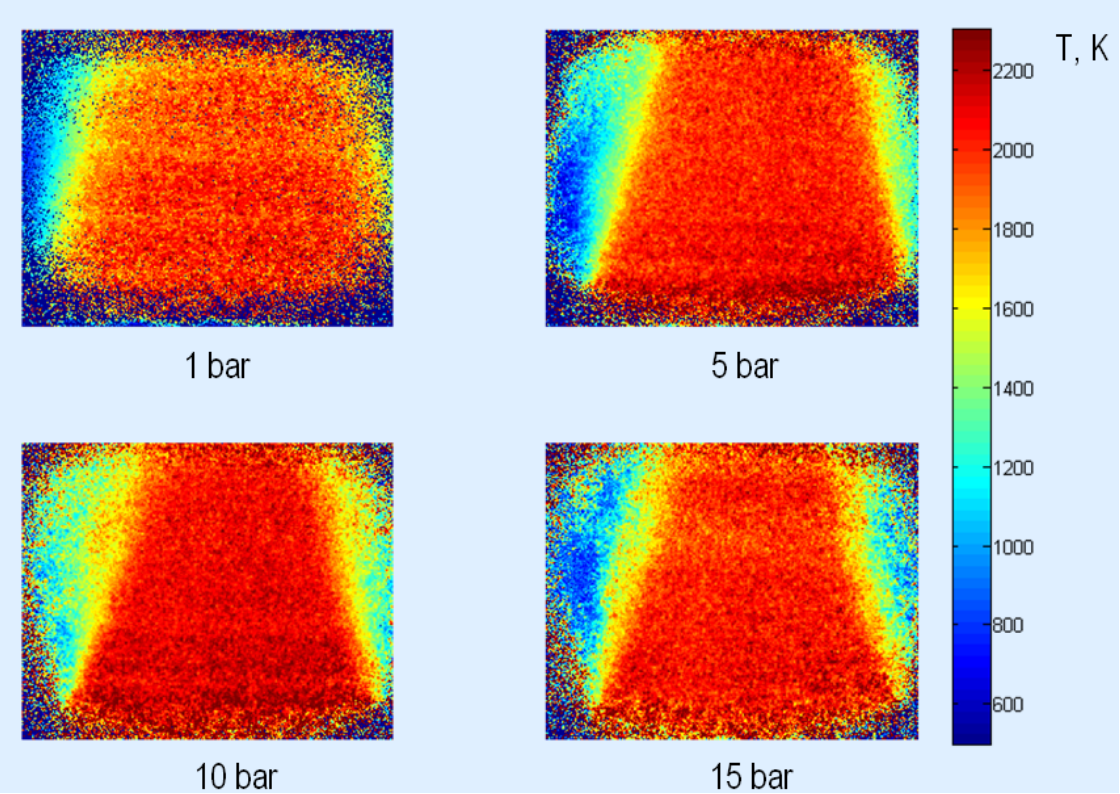

Figure 2.17.: 2-D Thermometry with NO in pressurized flames, taken by A. Denisov.

from the ratio of fluorescence from two different excitation lines and the comparison to calculations of the temperature-dependent ground state populations. In their publication it is especially stressed that the predissociative nature of O_2 is beneficial for high pressure investigations, as the LIF signal will not be affected by fluorescence quenching. Grinstead et al. [22, 32] discussed one and two-line thermometry of O_2 excited with a KrF laser in more detail. They showed that it is a valid assumption to conclude the rotational temperature even though the vibrational energy distribution is not equilibrated. They proposed to use overlapping transitions of the (0-6) and (2-7) bands of the Schumann-Runge system, for which the emission can be spectrally separated. They also found a non-linear dependence of the fluorescence signal on the laser intensity, which they claimed to be caused by ground state depletion. As a result, they defined an upper limit of the laser power to be applied which ensures measurements in the linear regime.
Decker [13] applied a similar method of O_2 thermometry as Grinstead et al. [22] to a Diesel engine, calibrated with a CARS measurement. He was the first to observe RET and estimate cross sections for the excited state. In the followup work of Sick et al. [45] also quenching cross sections derived from the measurements of Decker [13] are reported

for the B-state of O_2 for the first time. For the O_2 $b^1\Sigma_g^+$ state, which is of importance in the atmosphere, quenching rates were reported by Witt et al. [96] and Martin et al. [97]

Rothe et al. [65] and Nguyen and Paul [29] investigated the excitation dynamics for thermometry methods using predissociative OH or O_2 LIF. They referred to the competition between laser pumping out of the lower state and RET into this state as ground state depletion [65] or photobleaching [29], respectively. If the excitation rate reaches comparable values to RET, the limiting effect is the refill of the lower state due to RET. Both publications contain kinetic models (three- and five-state) and they provide results of RET rates measured at atmospheric conditions. They conclude that the low laser intensity needed to avoid saturation for 2-D two-line thermometry will not allow for single pulse measurements.

After these two publications, no further work on quantitative O_2 LIF has been published to my knowledge, with many questions remaining open, e.g. how pressure and gas composition influence the LIF signal dependence on the laser intensity. It remains also unclear how the ground state depletion affects the determination of the quenching cross sections published by Decker [13] and Sick et al. [45].

Amongst others, the motivation of this work is based on these questions.

3. Methods and Models

This chapter provides information about the method used to decompose O_2 spectra into its vibronic contributions and describes the models which are used to model, fit and predict saturated O_2 LIF measurements.

3.1. Non-Negative Matrix Factorization

To decompose O_2 LIF spectra, I can consider the fact that the emission patterns of ro-vibronic transitions can be different with respect to the involved vibrational states but repeat for different rotational transitions. The non-negative matrix factorization (NMF, see Berry et al. [98]) is a mathematical method to yield a low rank factorization of a matrix of data, as schematically shown in Figure 3.1. It can be seen as a principal component analysis method, the NMF allows to decompose the matrix A into the the product of the base vectors (H) of the principal components of A and their contributions (W) to A. The product WH is a low rank approximation, called NMF of A.

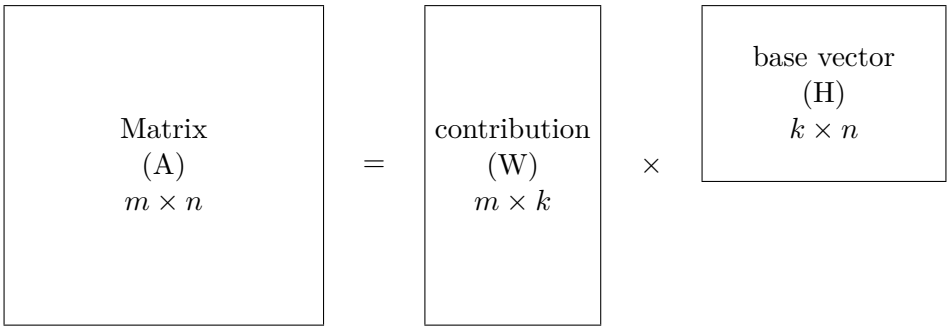

Figure 3.1.: Schematic decomposition with NMF.

Mathematically, the NMF problem can be formulated as (Berry et al. [98]): Given a nonnegative matrix $A \in R^{m \times n}$ and a positive integer $k < min\{m, n\}$, find nonnegative matrices $W \in R^{m \times k}$ and $H \in R^{k \times n}$ to minimize the functional

$$f(W, H) = \frac{1}{2}||A - WH||_F^2. \tag{3.1}$$

The numerical implementation is realized as follows: The matrices W and H are randomly initialized and afterwards the following equations are looped over 500 iterations.

$$H = H. * (W^T A)./(W^T W H + \beta_{NMF} H + 10^{-9}) \tag{3.2}$$

$$W = W. * (A H^T)./(W H H^T + \alpha_{NMF} W + 10^{-9}) \tag{3.3}$$

In this equations α_{NMF} and β_{NMF} are small regularization parameters that balance the trade-off between the approximation error and the constraints. Im my calculation they were set as $\alpha_{NMF} = 1$ and $\beta_{NMF} = 0$ as proposed by Berry et al. [98]. NMF decompositions have been successfully demonstrated in very different fields, such as text mining for email surveillance or in spectroscopy for spectral unmixing for spatially non-resolved space object characterization [98]. For the NMF decomposition, the number of base vectors to be identified must be given as an input. There is no way to calculate this number a-priori. It must be estimated first and empirically optimized for every decomposition. The lower limit is the number of spectral signatures which shall be identified. To the best of my knowledge, decompositions with NMF has not yet been applied in LIF investigations.

3.2. Three-Level LIF Model

A common approach to model population exchange for LIF is to extend the simplest two-level LIF model (see section 2.2) according to the processes that need to be considered (e.g. RET, Q), resulting in three-, four- or more level models [99]. I.e. for NO, a five-level model introduced by Lee et al. [28] successfully described saturated LIF signals. For the predissociative O_2 LIF, RET must be considered. Therefore, the two-level model is extended with a third level to account for ground state RET. Concerning the excited state predissociation will prevent a large population and RET will distribute the remaining excited state population. But I can not distinguish experimentally from which rotational state the fluorescence was emitted. Therefore, the introduction of a fourth state for excited state RET is unnecessary. A similar approach was chosen by Rothe et al. [30] to model predissociative OH LIF. Figure 3.2 shows the three-Level model schematically, the nomenclature is as introduced in Figure 2.5. The newly introduced third level is denoted E_0 and is a bath or pool state, summarizing all other rotational states of the same vibrational energy. These rotational states are the source states for RET. The schematic in Figure 3.2 is adapted to O_2 predissociative LIF including the following assumptions: $P >> A_{21}$, therefore A_{21} is negligible as a loss term for the population of E_2. Only P and b_{21} are considered depopulating E_2 (it will turn out in

chapter 7 that the depopulation of E_2 is dominated by predissociation and thus $b_{21}N_2$ is small). The RET between states E_0 and E_1 ($=(N_1^{s0}\frac{N_0}{N_0^0} - N_1^s)Q_{RET}$) is defined as a net rate, meaning the difference of RET into the state that is depopulated by the laser and out of it. At thermal equilibrium and without laser excitation, this rate is zero. For the quantitative investigations the involved transitions are represented with the rate

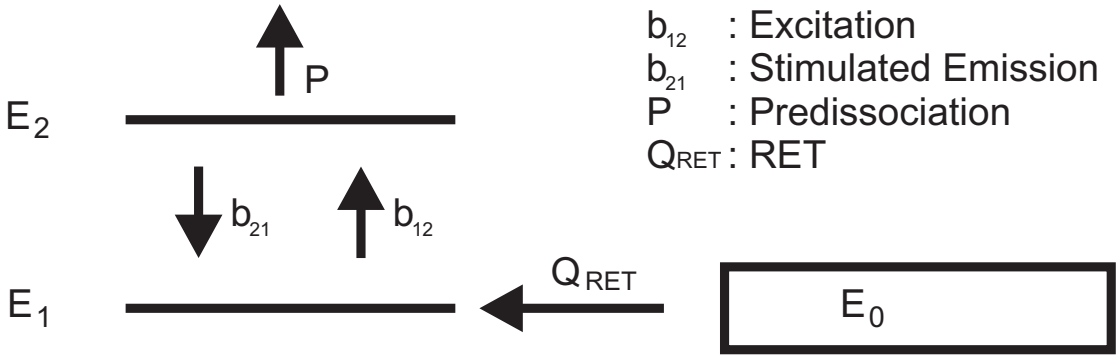

Figure 3.2.: Schematic of the three-level LIF model.

equation system, an ordinary differential equation system, shown in Equation 3.4 - 3.6.

$$\frac{dN_1^s}{dt} = b_{21}^s N_2^s - b_{12}^s N_1^s + (N_1^{s0}\frac{N_0}{N_0^0} - N_1^s)Q_{RET} \tag{3.4}$$

$$\frac{dN_2^s}{dt} = b_{12}^s N_1^s - b_{21}^s N_2^s - N_2^s P \tag{3.5}$$

$$\frac{dN_0}{dt} = -(N_1^{s0}\frac{N_0}{N_0^0} - N_1^s)Q_{RET}. \tag{3.6}$$

In this equations $N_{0,1,2}$ denote the populations of the corresponding states. The superscript $s = F1, F2, F3$ indicates the spin components in which the rotational level are split up to. We will see in subsection 4.3.3 that due to the energetic separation of the spin components, the excitation rates vary for the three of them. Superscript 0 denotes the initial population at $t = 0$. The calculation of the excitation rate b_{12} and the stimulated emission rate b_{21}, which both depend on laser properties, is explained in subsection 4.3.3. As shown in section 2.2, the LIF signal F is proportional to the population of the excited state, which comprises the spin components ($N_2 = \sum_s N_2^s$). I calculate it as the time averaged integral during the laser pulse length τ:

$$F = FC \cdot \frac{1}{\tau}\int_0^\tau N_2(t)dt \tag{3.7}$$

In this equation, FC is the product of all constants in Equation 2.7. $N_2(t)$ is solved for

analytically in a Matlab code.

For the calculations, the populations N^s are normalized with the initial population of the ground state. This results in the initial conditions $N_1^{s0} = 1$ and $N_2^{s0} = 0$. Consequently, the initial population of the pool state N_0^0 can be estimated from the thermal distribution.
Following the construction of the model, we assume that only rotational states of the same vibrational energy are involved in the refill processes of the state which is excited (E_1). It is reasonable to assume that these rotational states are populated according to the Boltzmann distribution. The size of the pool can be calculated as

$$N_0^0 = N \frac{\sum_{j \neq e} g_j e^{-E_j/k_B T}}{\sum_i g_i e^{-E_i/k_B T}} \qquad i,j = 1,2,3,... \qquad e\text{: state to be excited} \tag{3.8}$$

On the other hand, when a comparable three-level model has been used by Rothe et al. [30] to investigate predissociative OH LIF saturation, they assumed a pool of unlimited size for their comparison of the model with measurements, this will be discussed in chapter 7.
In the calculations above, I have not considered Q as a loss term for N_2^s. The reason is that Q is unknown. Andresen et al. [23] proposed that it is negligibly small, while Sick et al. [45] indicate it is in the order of P above 1 bar. But I can use the comparison of the model calculations to experiments to estimate quenching. By neglecting quenching as a loss term to N_2, I overestimate N_2. It is important to point out that neglecting Q does not have an influence on the dynamics of the excitation but on the constant FC in a predictable way: When I investigate the same flame gas composition at different pressures, Q depends only on the pressure, not on the laser intensity. The constant FC without considering quenching is by a factor $(P+Q)/P$ larger compared to the case if Q was known and considered. When comparing measurements to the model calculations, this results in an adaption of FC, which gets correspondingly smaller. From the distribution of FC versus the pressure, conclusions can be drawn about quenching. This is discussed in detail in section 7.6.

3.3. Detailed RET Model with State-to-State Rate Constants

For a more detailed description of RET, I set up a LIF model that includes state-to-state rate RET constants. As shown in subsection 2.3.1, there are several approaches to model state-to-state rate constants. All of them would be appropriate for my investigations,

I chose the MEG law from Koszykowski et al. [35], as they provide model constants for O_2 - O_2 and O_2 - N_2 which are experimentally verified by Millot et al. [100] and Seeger et al. [39]. The rate constants $k_{J_i \to J_f}$ from initial state J_i to the final state J_j are calculated as follows: For J-increasing transitions ($J_i < J_f$)

$$k_{J_i \to J_f} = \alpha p \left(\frac{1 + 1.5 E_{J_i}/k_B T \delta}{1 + 1.5 E_{J_i}/k_B T} \right)^2 \left(\frac{T_0}{T} \right)^N exp(-\beta \Delta E_{J_i J_f}/k_B T) \tag{3.9}$$

and determined by microscopic reversibility for J-decreasing transitions

$$k_{J_i \to J_f} = \frac{2J_{J_i} + 1}{2J_{J_f} + 1} k_{J_i \to J_f} \; exp(\Delta E_{J_i J_f}/k_B T) \tag{3.10}$$

The constants for the MEG law are listed in Table 3.1.

	O_2-O_2	O_2-N_2	Unit
α	16.70 ± 0.20	17.00 ± 0.40	$10^{-3}\text{cm}^{-1}\text{atm}^{-1}$
N	1.32 ± 0.01	1.31 ± 0.01	-
δ	1.32 ± 0.03	1.30 ± 0.05	-
β	1.45 ± 0.03	1.41 ± 0.05	-

Table 3.1.: MEG Constants taken from Millot et al. [100].

To model LIF, I am solving the system of linear differential equations for $J_{max} = 100$ rotational states each in the electronic ground state and the excited state for the three spin components. For the ground state, the population densities can be written as:

$$\frac{dN^s_{1Ji}}{dt} = \sum_{J_f, J_f \neq J_i} k_{J_i J_f} N^s_{1J_f} - \sum_{J_f, J_f \neq J_i} k_{J_f J_i i} N^s_{1J_i} \tag{3.11}$$

For the excited state, the population densities can be written as:

$$\frac{dN^s_{2J_i}}{dt} = \sum_{J_f, J_f \neq J_i} k_{J_i J_f} N^s_{2J_f} - \sum_{J_f, J_f \neq J_i} k_{J_f J_i} N^s_{2J_i} - P_{J_i} N^s_{2J_i} \tag{3.12}$$

The rate constants for excitation and stimulated emission are added to the corresponding states. The LIF signal F during the laser pulse length τ is calculated as the sum of the fluorescence from all rotational levels:

$$F = FC \cdot \frac{1}{\tau} \int_0^\tau \sum_i \sum_s N^s_{2i}(t) dt. \tag{3.13}$$

As for the three-level model, for the comparison with the experiments I detect the fluorescence from all rotational states, which is the reason for the summation over i in Equation 3.13

3.4. Simulation of Saturated O_2 Spectra

The only public available program known to simulate O_2 spectra is LIFSIM (developed by Bessler et al. [92], www.lifsim.com). In LIFSIM, the fluorescence signal is calculated based on a three-level model assuming the linear regime as well as a steady state with rapid ground state RET. Thus, the LIF signal is calculated as described in Equation 2.8 and hence cannot account for saturation. To predict the saturation of O_2 transitions, I have written a simulation code. This code is based on the three-level model described in section 3.2 to calculate the LIF signal.
The spectral database is taken from LIFSIM [92] which includes and expands data from Sick and Szabadi [11] and Lewis et al. [10]. This database lists the transition frequency, the ground state energy, the Einstein A and B coefficients as well as the predissociation linewidth for the Schumann-Runge B-X transitions of O_2 (for $v'' = 0 - 14, v' = 0 - 15, J'' = 1 - 51, J' = 2 - 52$) including the spin-rotational splitting. For the simulation of a spectrum, I calculated at every laser position of interest for every transition (spin component) the corresponding LIF signal by calculating

- the vibrational and rotational Boltzmann fractions f^s_{vib} and f^s_{rot} to yield N_1^{s0}, the relative ground state population.
- the sum of the Einstein A coefficients for transitions that fall into the given emission bandpass to yield FC^s
- the excitation and stimulated emission rates b^s_{12} and b^s_{21} which are proportional to the laser intensity. A detailed description how these rates are calculated and adapted to the experiment is given in subsection 4.3.3.
- the resulting LIF signal for a given laser intensity and Q_{RET} (determined form experiments) with the three-level model.

The sum of the LIF signals from each transition yields the final excitation spectrum.

4. Experimental

4.1. High Pressure Burner

The main investigations of this work were conducted at the high-pressure burner test rig (HPB). The HPB contains a McKenna-type burner in a steel casing originally designed by ONERA (Office National d'Etudes et de Recherches Aéronautiques), Paris. In this burner, schematically shown in Figure 4.1, the premixed flame is stabilized on a sintered bronze plate with a diameter of 20 mm. The casing is constructed to allow a pressurized flame up to 40 bar, for lean flames up to an air excess ratio of approximately $\lambda = 1.5$ for CH_4/air combustion. The flame is optically accessible through seven quartz windows. The burner is designed to provide a highly stationary flame. Important flame conditions (pressure, air excess ratio, inflow speed) can be easily varied with our newly developed control software and the updated hardware. I also installed a vacuum pump at the

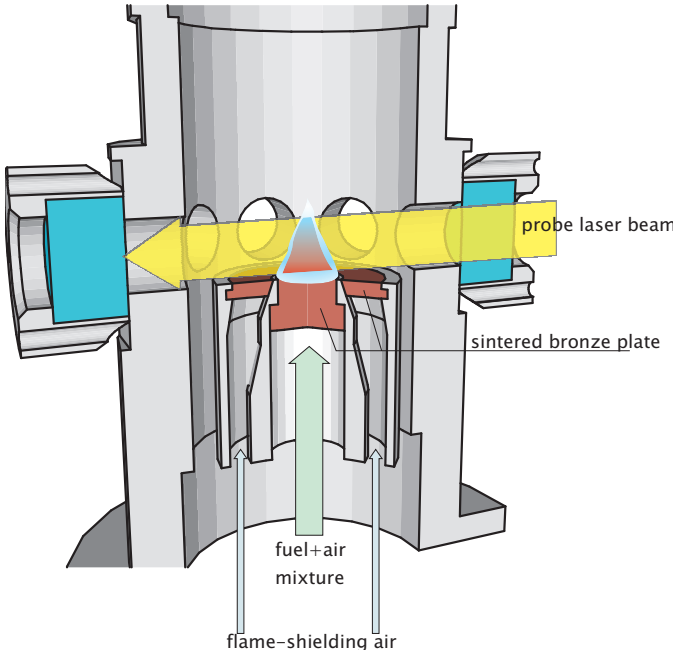

Figure 4.1.: Schematic of the high pressure burner as drawn by Alexey Denisov.

exhaust valve of the burner to enable measurements at sub-atmospheric pressures.

LIF Setup

The overall LIF setup, which I developed for measuring saturated O_2 LIF at the HPB is shown schematically in Figure 4.2. I developed a data acquisition routine to synchronize

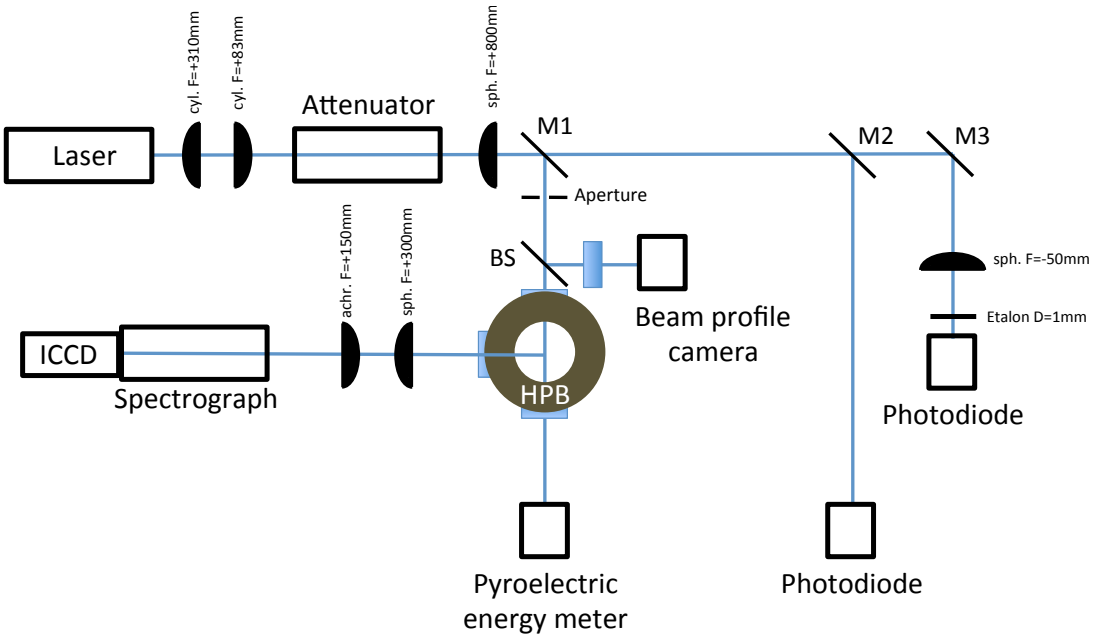

Figure 4.2.: LIF setup at the high pressure burner test rig.

the measurement data of the various devices. These are the following:

- A tunable narrowband krypton fluoride (KrF) excimer laser "Lambda Physik Compex 150T" for the excitation. This laser consists of two separate lasers, as schematically shown in Figure 4.3. The first laser is used as an oscillator, the light is reflected between a tunable grating (600 grooves per millimeter) and a $R = 95\,\%$ output coupler. Afterwards the light is single pass amplified in the second laser. With this setup, the laser can produce 200 mJ/pulse UV light with a FWHM of about $0.6\,\mathrm{cm}^{-1}$ which is tunable in the range of approximately $248\,\mathrm{nm} - 249\,\mathrm{nm}$. The pulse length is about 20 ns.
- A "Chromex 250i" spectrograph to spectrally resolve the fluorescence. I used it with a holographic 1200 grooves per millimeter grating to capture the emission centered at $\lambda = 290\,\mathrm{nm}$ within a range of about 45 nm with a spectral resolution of 0.6 nm.

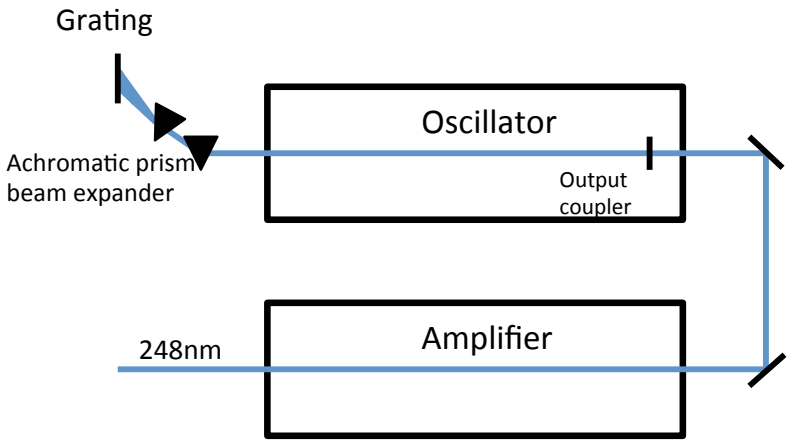

Figure 4.3.: Schematic of the KrF excimer laser.

- A LaVision ICCD camera (customized "FlameStarII") to record the spectrally resolved fluorescence. For O_2 LIF, I collected and summarized the fluorescence of 24 laser pulses on the chip with a gain of 72 counts per photoevent at a quantum yield of 12 % - 13 % (software setting gain=90), gated ±20 ns around the laser pulse.

- A Spiricon SP620U beam profile camera. I recorded the 2-D beam profile with a beam splitter and an additional window at a position that resembles the middle of the burner. The beam profile was recorded once per laser operation (which was usually once per day). As long as the laser is not switched off, it will not change for the KrF laser.

- A Gentec Solo PE pyroelectric energy meter (measurement head: QE25SP-H-MB-DO) to monitor the laser energy on a shot-to-shot basis. Additionally, I measured the laser energy with a photodiode (all PIN-photodiodes in the setup were Hamamatsu S3279, operated at 12 V reverse voltage), which was calibrated once every laser operation.

- A beam attenuator which contains four swiveling quartz plates to vary the laser intensity (as described in Bennett and Byer [101]). I installed a stepper motor to it in order to synchronize the attenuator with the data acquisition routine.

For the saturation measurements I had to ensure that the laser tuning does not change during the measurement. Therefore, I prepared the data acquisition routine to yield the same settings before the beginning and after the end of a measurement. By comparing

the averaged LIF signal of an emission line before and after the measurement I could check whether the laser tuning changed.

4.2. Catalytic Burner

The catalytic burner test rig is an optically accessible channel flow-reactor, comprising two horizontal platinum coated Si[SiC] ceramic plates (300 mm long (x-direction), 104 mm wide (z-direction), 9 mm thick, positioned 7 mm apart (y-direction)) and two vertical quartz windows (see Figure 4.4, [82, 102]). The inner ceramic plate surfaces were coated by plasma vapor deposition, with a 1.5 µm thick non-porous Al_2O_3 layer followed by a 2.2 µm thick Pt catalyst layer. Two 350 mm long, 50 mm high and 35 mm thick

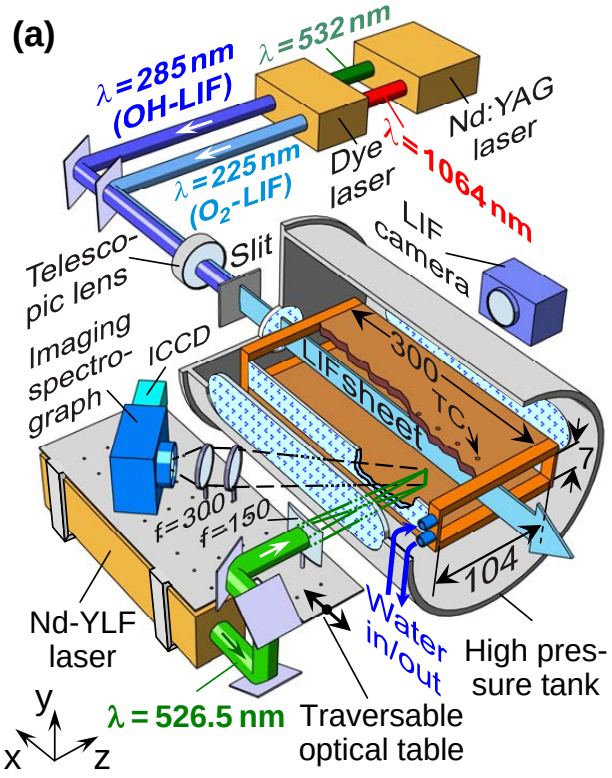

Figure 4.4.: Schematic of the catalytic burner test rig as drawn by M. Schultze, including the installations for Raman measurements.

quartz windows at both sides of the tank provided optical access to the reactor. Two additional quartz windows at the rear tank flange and the reactor exhaust, respectively, facilitated streamwise optical accessibility for the LIF laser beams. Flame gas is supplied

by pressurized bottles and premixed in two sequential static mixers.

LIF Setup

To measure O_2 LIF at the catalytic burner test rig, we used a Nd:YAG laser (Quantel YG781C) in combination with a dye laser (Quantel TDL90) to produce light around 226 nm. A schematic of the laser is shown in Figure 4.5. The fluorescence is measured with a LaVision ICCD camera as explained in the previous section. For one of the

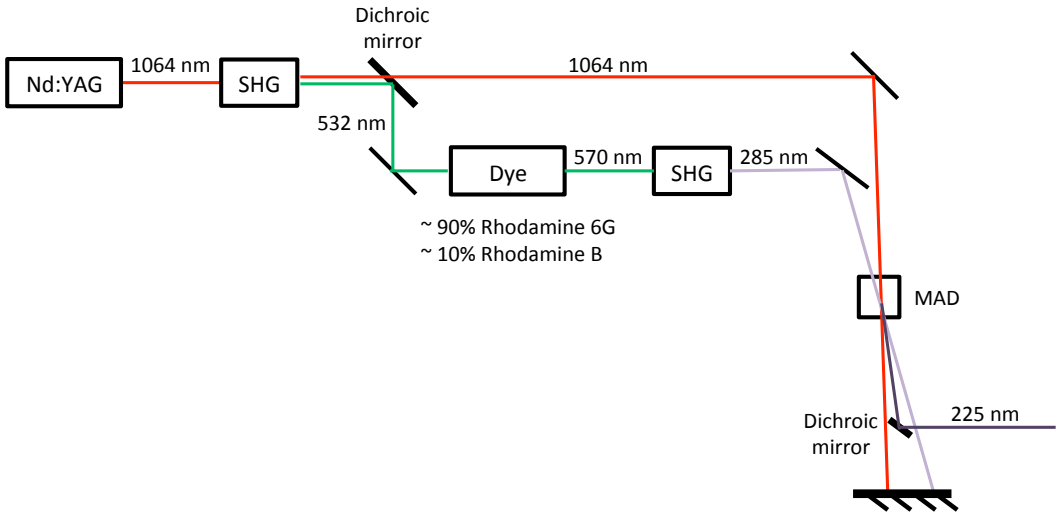

Figure 4.5.: Dye Laser setup for O_2 excitation.

experiments, we wanted to compare O_2 and OH measurements at a stationary operating point in the catalytic burner. Therefore, we modified the dye laser in a way to easily switch between the excitation of O_2 at 226 nm and the excitation of OH at 285 nm (see Figure 4.6). The two different bandpass filters in front of the ICCD camera, a combination of colored glass filters and dielectric reflection filters for O_2 fluorescence detection (260 nm-285 nm, rejecting a H_2 Raman signal at 249 nm) and a combination of colored glass and interference filters for the OH detection (300 nm-326 nm) could also be switched easily. We measured the fluorescence from O_2 and OH sequentially. With a second ICCD camera, the measurement could also be conducted simultaneously.

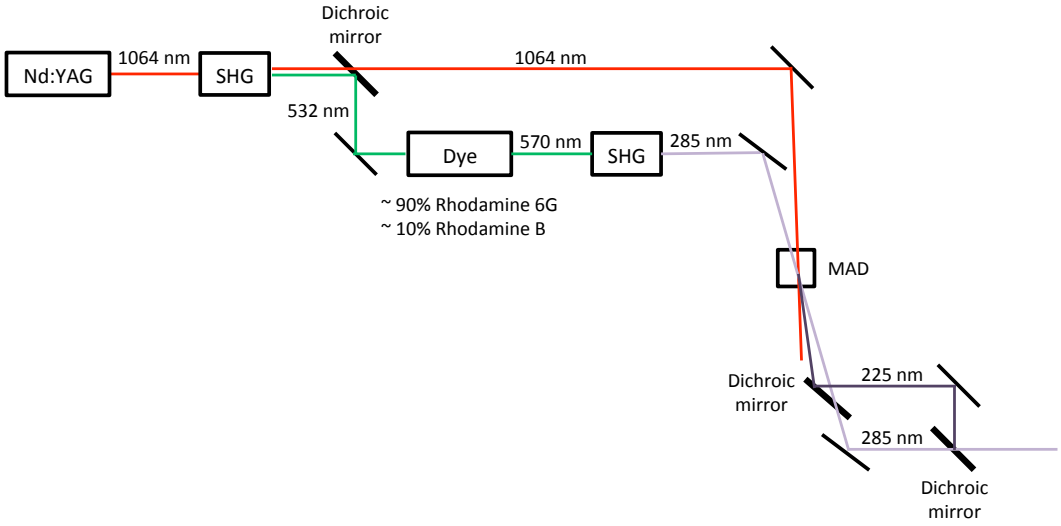

Figure 4.6.: Dye laser setup for combined O_2 and OH LIF.

4.3. Data Processing

4.3.1. Image Processing

The quantitative data analysis is based on the pictures taken with the LaVision ICCD camera at the exit of the spectrograph. The upper part of Figure 4.7 shows such a picture taken for a distinct excitation wavelength, which captures four emission lines along the slit height. For the further data treatment, I averaged the emission along the slit height, as shown in the lower part of Figure 4.7. For the analysis in this work, the averaged emission spectrum was used for two purposes. When scanning the laser, I took a picture for every excitation wavelength (usually with a step-size of about 2 pm). In a post-processing step, I constructed a matrix in which the rows contain the averaged emission spectra resulting in a so-called emission/excitation spectrum as shown in Figure 4.8A for the entire excitation range of the KrF laser. At every excitation wavelength, thus for every picture, I also recorded the laser energy, which varies with the wavelength as shown in Figure 4.8B. In part C, I show the emission-integrated excitation spectrum, which I also normalized with the laser power. From the energy-corrected excitation spectrum it can be seen that the signal-to-noise ratio dramatically decreases near the spectral bounds of reasonable light output of the laser. Therefore I only used the transitions in the center part of the spectrum for the investigations in this work. The other purpose is to extract the integrated fluorescence from the averaged emission spectrum. For this calculation, I subtracted the background signal as shown in Figure 4.7B and integrated the average emission over the entire emission range.

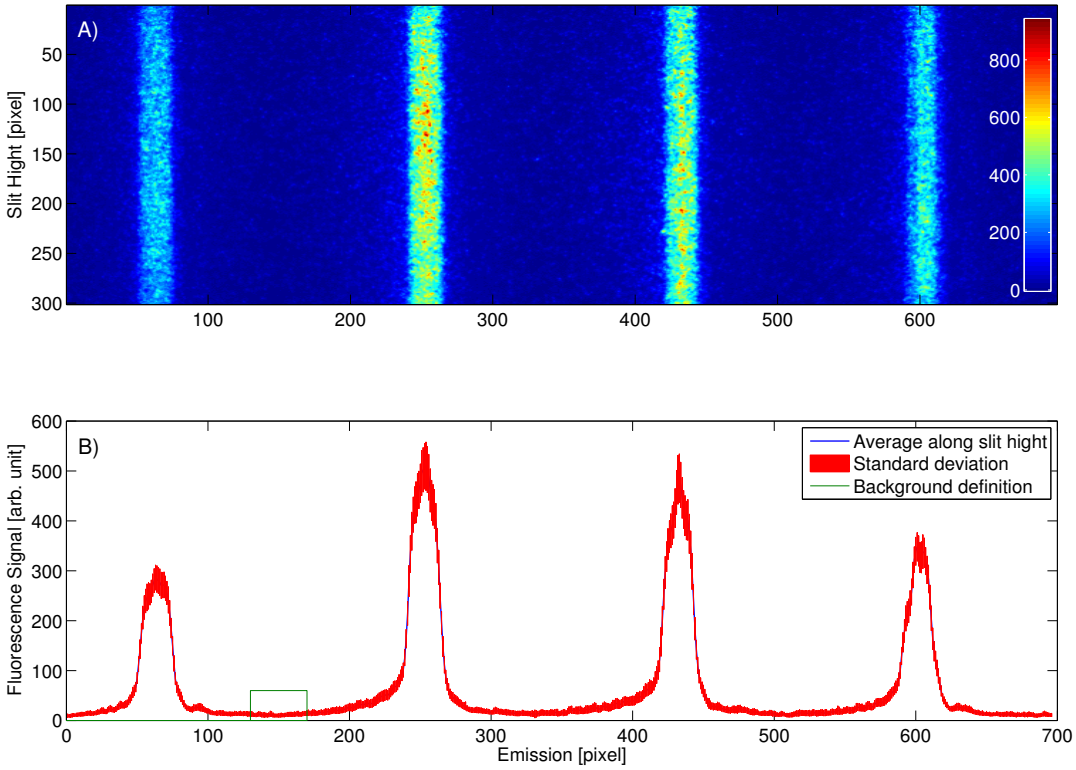

Figure 4.7.: A) Picture taken with the LaVision ICCD camera and B) mean emission spectrum of the spectrographs slit height.

4.3.2. Determination of the Laser Line Width

For the latter calculations, a precise knowledge about the line width of the KrF laser is required. To ensure a high quality determination, the line width is derived in two different ways from the experimental data. For this purpose, I recorded a double resolved emission/excitation spectrum (see Figure 4.10) and simultaneously a Fabry-Perot etalon interference pattern.

Calculation of the Laser Line Width with a Fabry-Perot Etalon

A part of the laser beam is guided through a spherical lens ($f = -50\,cm$) and an etalon allowing to observe an interference pattern on a screen (see Figure 4.2). Through a pinhole, the intensity of the interference rings are measured using a photodiode, which is shown in Figure 4.9.
With the properties of the Fabry-Perot etalon given in Table 4.1 and the equation for

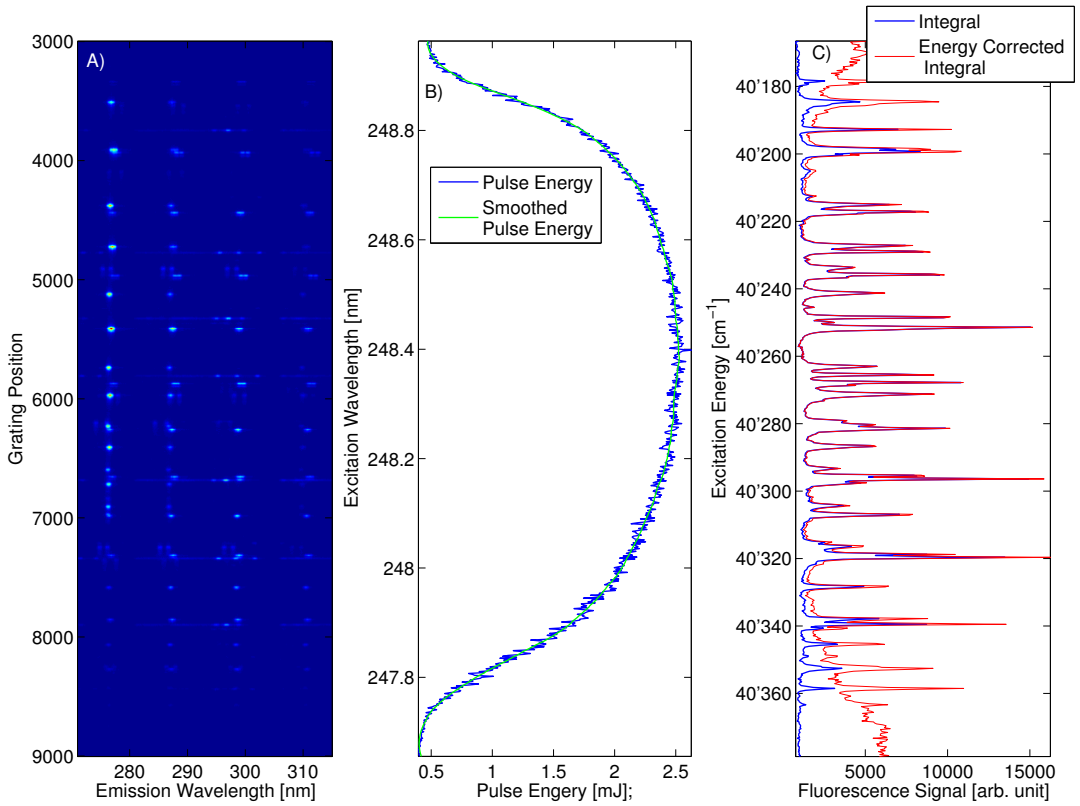

Figure 4.8.: A) Double resolved emission excitation spectrum, B) laser energy measurement and C) emission integrated excitation spectrum for a CH_4/air flame.

the finesse F of the Fabry-Perot etalon (taken from Hecht [103]), F can be calculated as:

$$F = \frac{\pi\sqrt{R}}{1-R} = 37.667 \tag{4.1}$$

The finesse is defined as the ratio between the distance of adjacent maxima (usually termed free spectral range) and the full width at half maximum (FWHM) of the fringe peak:

$$F = \frac{\Delta\lambda}{\Delta\nu} \tag{4.2}$$

With Equation 4.2 and the measurement data from Figure 4.9, the FWHM of the etalon can be calculated in grating steps as:

$$\Delta\nu_{etalon} = \frac{\Delta\lambda}{F} = \frac{87.359}{37.667} = 2.3192 \text{ Grating Steps} \tag{4.3}$$

The measured and fitted curves in Figure 4.9 are a convolution of the etalon peak

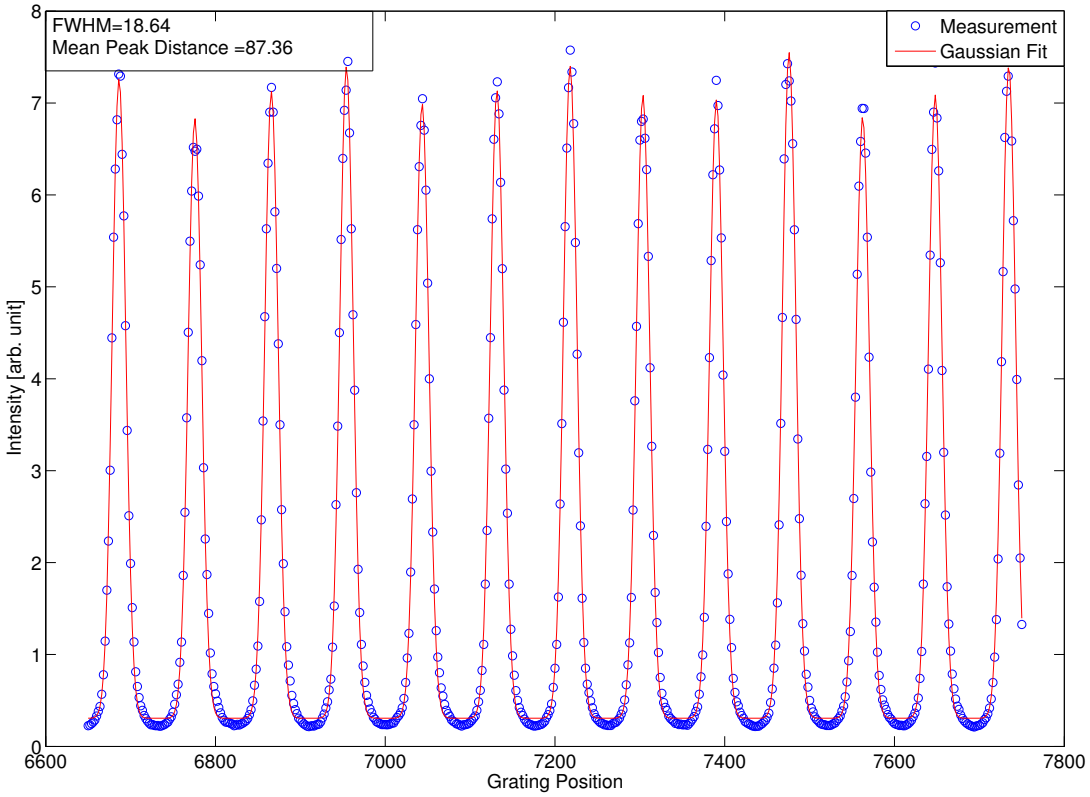

Figure 4.9.: Photodiode measurements of the Fabry-Perot etalon interference pattern and corresponding Gaussian fit.

and the laser line peak which can, according to the measurement in Figure 4.9, be assumed to have a Gaussian shape with a convoluted FWHM of 18.496 Grating Steps. The convoluted FWHM can be calculated as:

$$\Delta\nu_{conv} = \sqrt{\Delta\nu_{laser}^2 + \Delta\nu_{etalon}^2} \quad \text{and therefore} \tag{4.4}$$

$$\Delta\nu_{laser} = \sqrt{\Delta\nu_{conv}^2 - \Delta\nu_{etalon}^2} = \sqrt{18.641^2 - 2.319^2} = 18.496 \text{ Grating Steps} \tag{4.5}$$

The conversion from grating positions to wavenumber or wavelength was determined

Thickness	d_{etalon}	1 mm
Reflectivity	R_{etalon}	0.9 (see Figure A.2)
Refractive Index	n_{etalon}	1.50855 (Suprasil, see Figure A.3)

Table 4.1.: Properties of the Fabry-Perot etalon used in the experiment at 248 nm.

with the help of the OH lines within the recorded spectrum (Figure 4.10). The OH lines are sharply peaked and their positions are known from literature. Using LIFBASE [104], the conversion factor is found to be 0.034311 cm^{-1}/Grating Step.

The FWHM of the laser line width, expressed in wavenumbers is consequently: $\Delta\nu_{Laser} = 0.635\,cm^{-1}$.

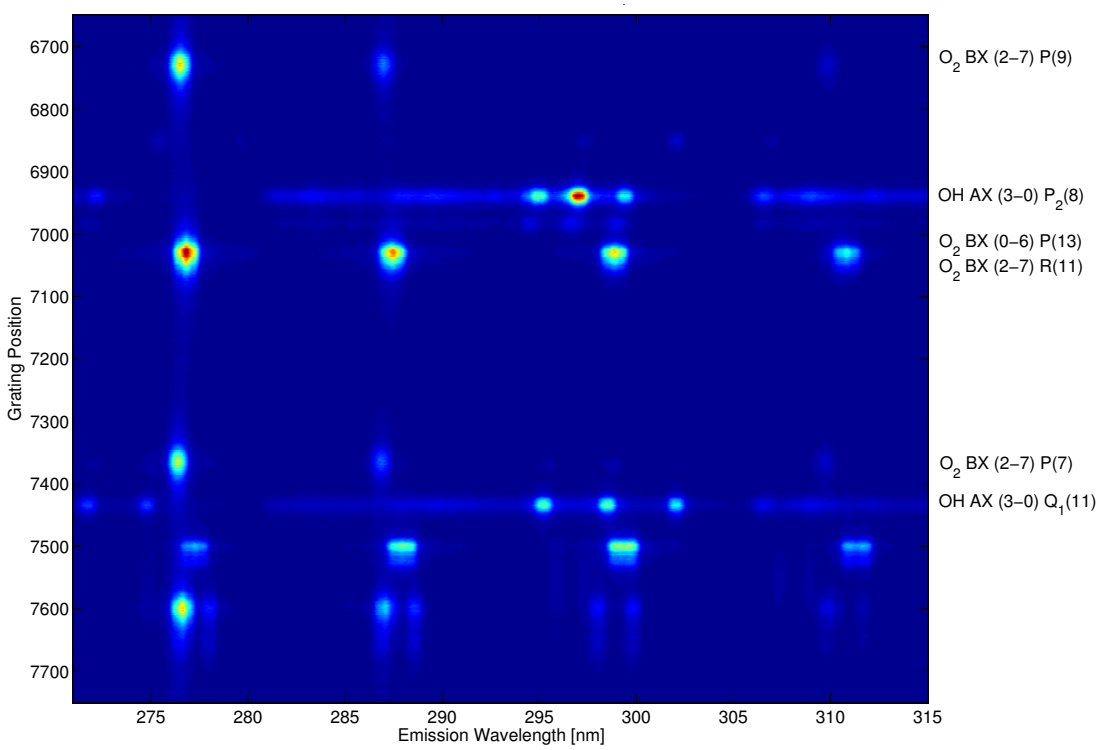

Figure 4.10.: Double resolved emission/excitation spectrum for line width determination.

Determination of the Laser Line Width with LIFSIM

Secondly, I used LIFSIM calculations (Bessler et al. [92]) to determine the laser line width. For this purpose, the measured double resolved emission/excitation spectrum (Figure 4.10) was integrated only at the emission ranging from 275 nm to 278 nm to avoid OH fluorescence, and compared with LIFSIM calculations. Figure 4.11 shows the LIFSIM fit to the measurement. The laser line width is determined to be $\Delta\nu_{Laser} = 0.630\,cm^{-1}$, which is in very good agreement with the calculations from the Fabry-Perot etalon. With regard to the results of this work presented in chapter 7, I emphasize here

that this measurement was conducted at a low laser intensity to minimize the effects of saturation.

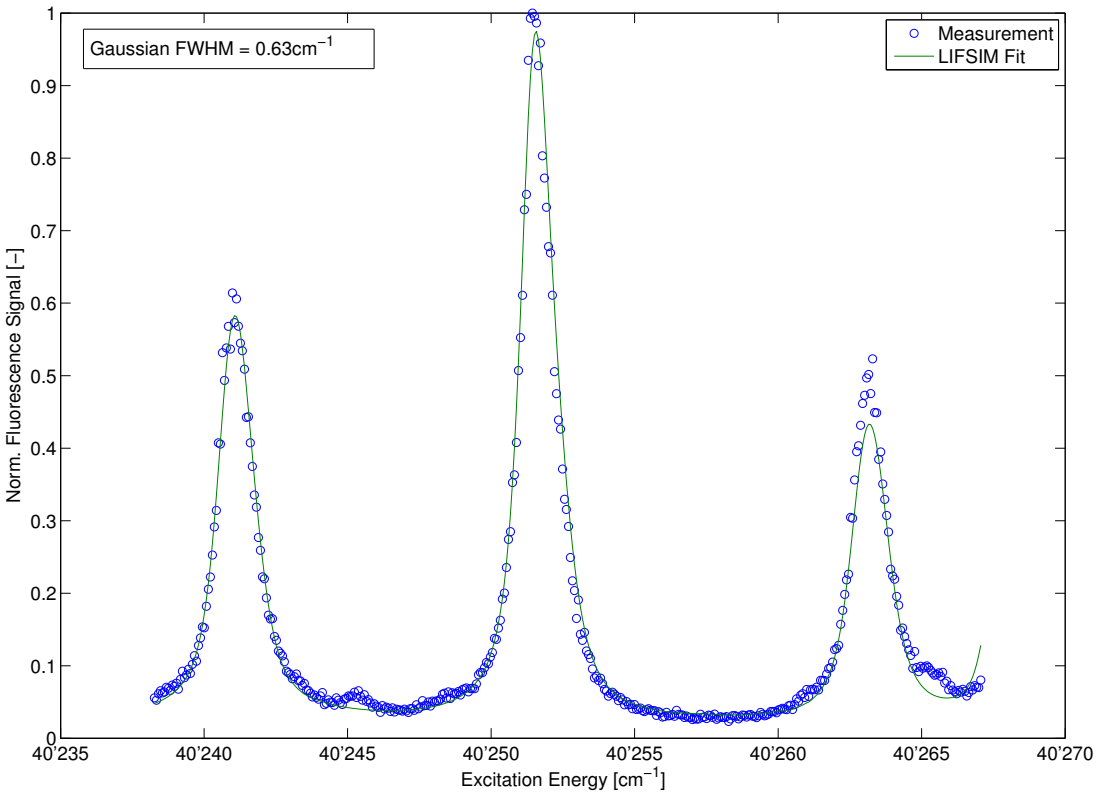

Figure 4.11.: Integrated emission from 275 nm to 278 nm and corresponding fit using LIFSIM [92].

4.3.3. Calculation of the Excitation Rate

The excitation rates of the transitions of interest are an important input to the model calculations of this work. The excitation rates depend strongly on the experimental setup (e.g the bandwidth of the exciting laser beam). Therefore, they need to be adapted to the setup. As the calculation is not straightforward, I explain it here in more detail.
The quantum-mechanical process relevant for excitation is the induced absorption, which is given by the Einstein B coefficient (in $[\frac{m^3}{J \cdot s^2}]$). The B coefficients are defined in terms of a broadband, isotropic radiation field and need therefore to be adjusted to almost monochromatic and directed light ([105]). The excitation rate b_{12} is proportional to the

overlap integral of the absorption line and the laser line and can be written as [14]

$$b_{12}(\nu) = \frac{N_1 B_{12} I}{c} \int g(\nu - \nu_0) h(\nu - \nu_l) d\nu. \tag{4.6}$$

In this equation N_1 is the number of molecules in the electronic state which is excited, B_{12} is the Einstein B coefficient (in $[\frac{m^3}{J \cdot s^2}]$), I is the spectral irradiance ($[\frac{W \cdot s}{m^2}]$), and c is the speed of light ($[\frac{m}{s}]$). $g(\nu)$ and $h(\nu)$ represent normalized line shape functions for the absorption and irradiance ($\int_{-\infty}^{+\infty} g(\nu)d\nu = \int_{-\infty}^{+\infty} h(\nu)d\nu = 1$) relative to the center position of the absorption line ν_0 and the (variable) center position of the laser line ν_l. For the KrF laser $h(\nu)$ can assumed to be Gaussian and its FWHM is determined in the previous section. $g(\nu)$ for the O_2 lines in this work can be calculated as the convolution of line shapes caused by the predissociation lifetime (FWHM denoted with $\Delta\nu_{pred} = 1/(2\pi\tau_{pred})$), Doppler broadening ($\Delta\nu_{dop} = \sqrt{(8ln2)(k_B T/mc^2)}\nu_0$, taken from [106]), and collisional broadening ($\Delta\nu_p$). The natural linewidth can be neglected as $\tau_{pred} << \tau_{spont}$. The predissociation lifetimes are known [10, 92] and Doppler broadening can be calculated but the pressure broadening is unknown. Therefore, I determined it experimentally, by measuring a LIF scan of the O_2 P9(0-6) line at different pressures. It must be considered that the line shape I can measure is a convolution of the O_2 absorption line and the laser line which can be expressed as:

$$\begin{aligned} L(\nu, \Delta\nu_{Laser}, \Delta\nu_{pred}, \Delta\nu_{dop}, \Delta\nu_p) =& (g * h)(\nu) \\ =& \int_{-\infty}^{+\infty} g(\nu) h(\nu - (\nu_l - \nu_0)) d\nu. \end{aligned} \tag{4.7}$$

The energetic separation of the O_2 spin components is too small to excite them separately with the KrF excimer laser (the predissociation line width is larger than the energetic separation), so the measurement summarizes the convolution of the lines of the three spin components with the laser line

$$\begin{aligned} L_c(\nu, \Delta\nu_{Laser}, \Delta\nu^s_{pred}, \Delta\nu_{dop}, \Delta\nu_p) =& \sum_s (g^s * h)(\nu) \\ =& \sum_s \int_{-\infty}^{+\infty} g^s(\nu) h(\nu - (\nu_l - \nu_0)) d\nu. \end{aligned} \tag{4.8}$$

Figure 4.12 shows fits of L_c to measurements of the P9(0-6) line of the O_2 B-X system, in which the collisional broadening denoted with $\Delta\nu_p$ was the fit parameter. The resulting line broadening for different flames which is found to be $0.05\,\mathrm{cm}^{-1}\mathrm{bar}^{-1}$ (with respect to FHWM) is shown in Figure 4.13. Uncertainties in the relative positions of the spin components and experimental uncertainties do not allow to determine the small effect

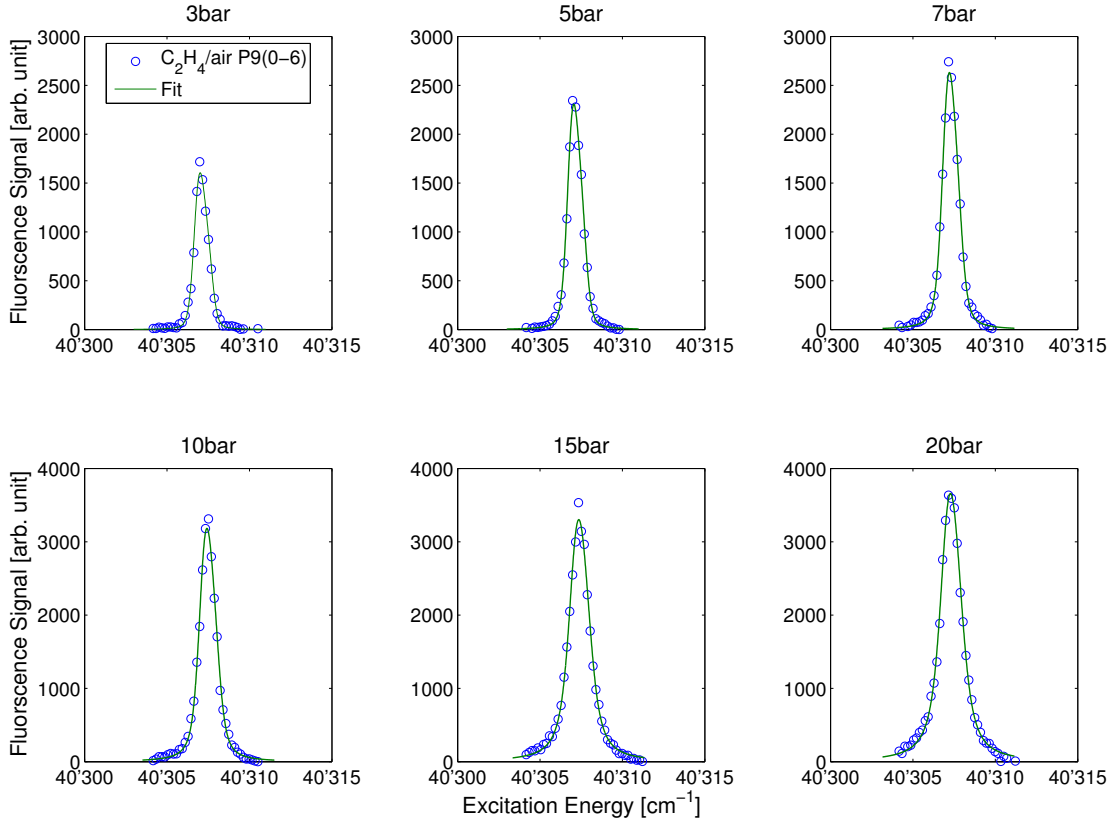

Figure 4.12.: Line shape fits of the P9(0-6) line measured in C_2H_4/air Flames.

of pressure broadening on the line width below 3 bar. The observed line broadening coefficient agrees well with the findings of Sick et al. [45].
With the collisional broadening known, I can calculate the excitation rate for each component according to Equation 4.6 as

$$b_{12}^s(\nu) = \frac{N_1^s B_{12}^s I}{c} \int g^s(\nu - \nu_0) h(\nu - \nu_l) d\nu. \tag{4.9}$$

For all model calculations in this work, the LIF signal is calculated as the sum of the LIF signals from the spin components. For the saturation measurements, I recorded the LIF signal at the excitation wavelength which provided the peak emission intensity. To identify this wavelength as precisely as possible, I calculated the O_2 line shape built up from the three components and matched its maximum. Therefore I can account for the different sizes of the overlap integral for the three spin components and determine b_{12}^s as precisely as possible. Stimulated emission b_{21}^s can be calculated according to

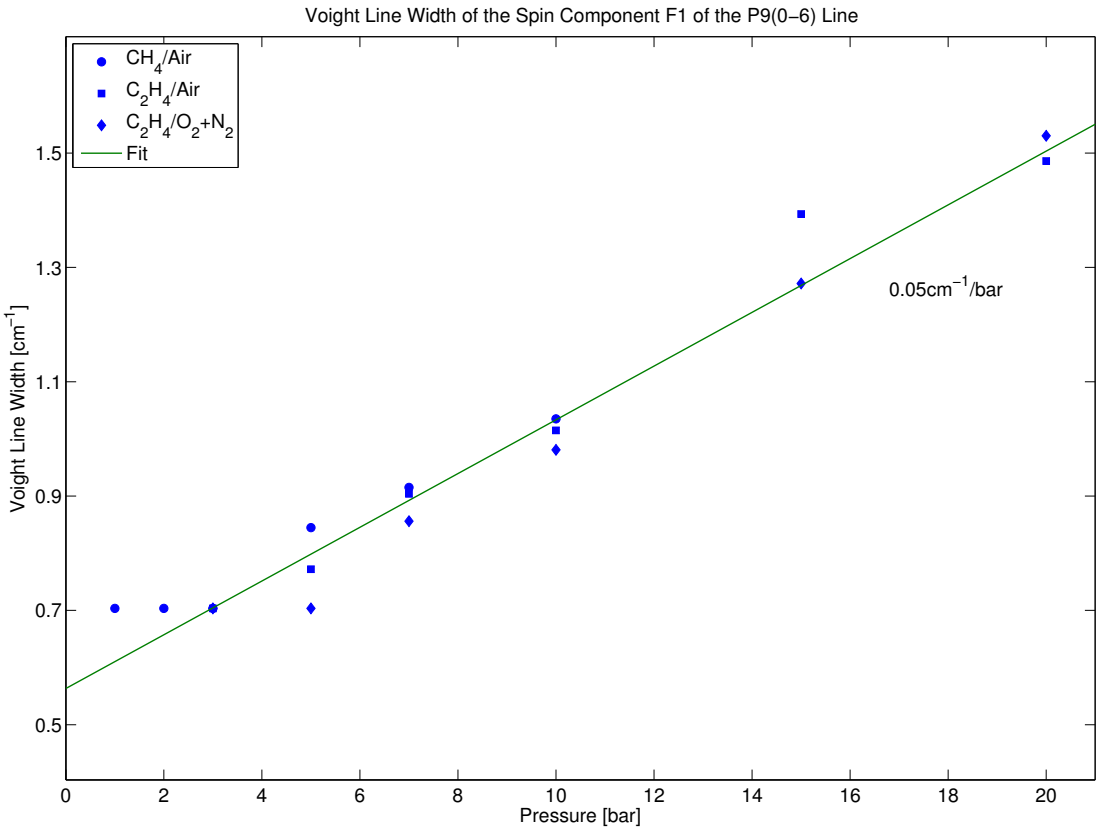

Figure 4.13.: Line broadening caused by collisions measured for the P9(0-6) line in different flames. The green curve depicts a weighted linear fit resulting the collisional line broadening coefficient with respect to FWHM.

Equation 4.9, but the Einstein B coefficient must be adjusted with the degeneracy factors g as

$$B_{21}^{s} = \frac{g_1}{g_2} B_{12}^{s}. \tag{4.10}$$

4.3.4. Beam Profile Measurements

The 2-D beam profile is recorded with a CCD camera. As shown in section 4.1, I measured the beam profile at a position that represents the center of the HPB. Therefore a part of the beam was split off in front of the burner. To reproduce the beam path as precisely as possible, I installed one of the optical windows in this beam path at the corresponding HPB window position, and installed a fluorescence glass at the position where the center of the HPB would be. The fluorescence glass converts UV to visible light, which is then recorded with the beam profiling camera. Figure 4.14 shows a measurement of a 2-D beam profile. For the calculation of the laser intensity, I averaged

the intensity in the region marked in Figure 4.14 and assumed that the laser intensity is zero outside the marked region (resembling a beam profile without wings).

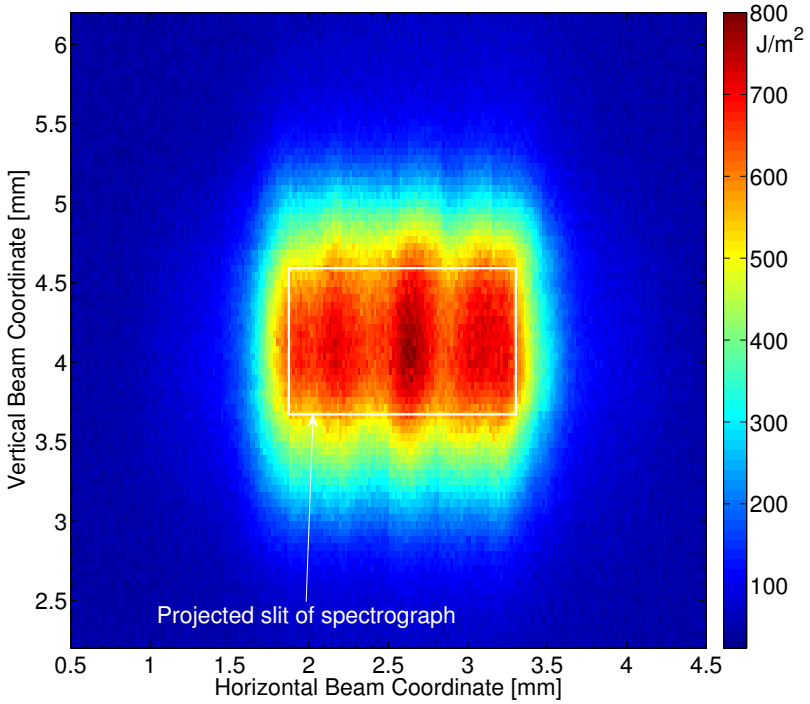

Figure 4.14.: Laser beam profile with measurement region, marked is the projected slit of the spectrograph to record the emission.

5. Flame Front Detection with Planar O_2 LIF in Rich Flames

In this chapter, I present results of the application of 2-D O_2 LIF in a catalytic reactor in order to visualize flame fronts in rich syngas combustion. I will show that with 2-D O_2 LIF, the ignition location of a flame can be derived with similar precision as with traditional OH LIF.

5.1. Reasons for the Use of O_2 LIF

In a joint project in our laboratory, the combustion of H_2-rich syngas was investigated numerically and experimentally. The combustion of such fuels in gas turbines with integrated solid-fuel gasification, combined with pre-combustion carbon capture is a promising technology for reducing greenhouse gas emissions in power generation. In that project the fuel is partly converted catalytically. In the Combustion Fundamentals group, M. Schultze was concerned with the numerical simulations of the combustion chemistry, while our group provided the laser diagnostics in order to verify these simulations experimentally. Traditionally, we use 2D OH LIF to visualize flame fronts and compare the measurements to the OH radical predictions of the simulations. For this experiment, the rich combustible gas mixtures consist of N_2, H_2, CO and O_2. We observed that, when increasing the pressure in the reactor, the OH LIF signal decreased rapidly and fell below the detection limits above 7 bar. In such flames, the mole fraction of OH decreases with increasing pressure [107]. Therefore, the OH LIF signal decreases as well, as the effects of increasing number density and increasing fluorescence quenching on the LIF signal cancel each other. We tried also LIF with CH_2O, which is another key intermediate species in combustion [108], and has been used to visualize flame fronts before [21]. But we were not able to see a sufficient LIF signal at any pressure.
Therefore, we decided to use O_2 LIF. The O_2 molecule is not commonly used in combustion diagnostics due to several issues. In many of our applications the measured LIF signal of excited O_2 is lower e.g. lower compared to the one of OH fluorescence, even though O_2 is much more abundant than OH. This is caused e.g. by the low fluorescence

quantum yield due to the predissociative nature of the excited O_2 states (see section 2.1) and by the strong temperature dependence of the O_2 ground state populations (the lowest vibrational level which can be accessed with standard dye laser systems is $v'' = 4$, while $v'' = 0$ for OH can be excited). Further complications arise from the fact that many excitation lines of O_2 overlap with excitation lines of NO. As their emission also overlaps, we can not distinguish the emission from the two molecules. The diagnostics idea of this project is that O_2 in fuel-rich mixtures is only present before the reaction zone. Within the reaction zone, all O_2 is converted into H_2O and CO_2. The outer boundary of the fluorescence signal when performing spatial O_2 LIF should report the beginning of the reaction zone.

5.2. O_2 Excitation

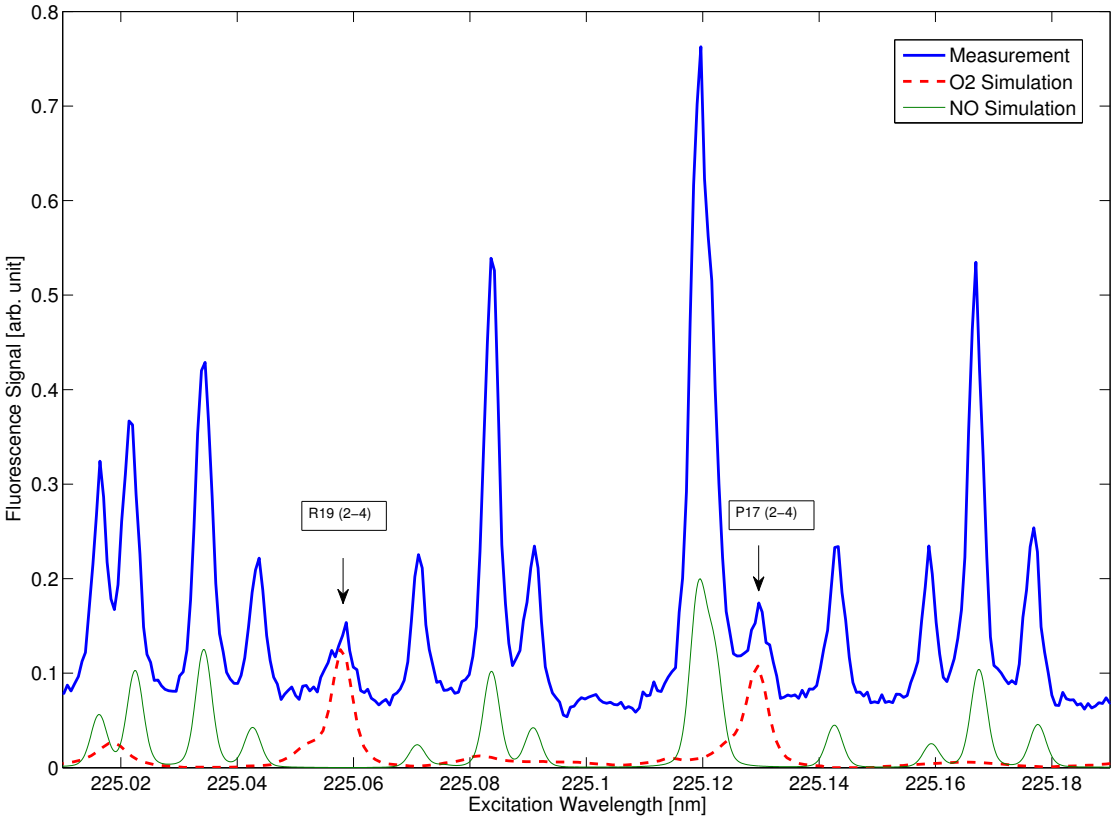

Figure 5.1.: Measured LIF excitation spectrum and LIFSIM [92] simulations of O_2 and NO in the Bunsen flame, emission bandpass approx. 250 nm to 260 nm.

For exciting O_2 we used a combination of a Nd:YAG laser and a Rhodamin 6G/B dye laser to generate tunable UV light around 225 nm (see section 4.2 for details). In this range, we can excite transitions of the (2-4) and (5-5) vibrational bands of the O_2 Schumann-Runge system. As the populations of the vibrational states are Boltzmann-distributed the LIF signal increases quickly with the temperature and we are able to observe emission from the (2-4) bands above approximately 600 K at 1 bar. The Boltzmann fraction of $v'' = 4$ at expected temperatures of approximately 1000 K increases roughly 300 times compared to room temperature, which provides sufficient LIF signal for the measurements. When exciting a $v'' = 4$ transition, a region before the flame front can be made visible with LIF, in which the temperature is already elevated above approximately 600 K. To ensure correct tuning of the laser to an O_2 absorption line and to monitor whether the laser tuning changes during the measurement, we installed a calibration C_3H_8 Bunsen flame to the setup at the exit of the laser. A photomultiplier behind a mercury-line bandpass filter (approximately 250 nm to 260 nm) collected the fluorescence. In this Bunsen flame, the LIF signal of NO was stronger compared to the one of O_2. Moreover, there are about four times more NO excitation lines than O_2 lines within the tunable range of the laser. One of the challenges was to identify the O_2 lines between the NO lines in the Bunsen spectrum. Measurements of a LIF excitation spectrum in the Bunsen flame and LIFSIM [92] simulations of O_2 and NO are shown in Figure 5.1. As can be seen from this plot, the O_2 R19(2-4) line is well separated from the neighboring NO lines and therefore well suitable for the investigations. Relevant spectroscopic properties of the O_2 R19(2-4) line are depicted in Table 5.1.

	Excitation Energy [cm^{-1}]	Predissociation Line width [cm^{-1}]	v”	v’	J”	J’
F1	44432.3789	0.308	4	2	19	20
F2	44432.4180	0.489	4	2	19	20
F3	44433.5430	0.835	4	2	19	20

Table 5.1.: Properties of the O_2 R19(2-4), data is taken from [92].

5.3. Planar O_2 LIF

Figure 5.2 shows a LIF measurement of the O_2 R19(2-4) line in the catalytic reactor at 3 bar. As can be seen from this plot, the O_2 fluorescence has a well-defined shape. The

right outer boundary marks the reaction zone in which all O_2 is consumed. The inner boundary marks the preheated gas mixture which is hot enough that the vibrational state $v'' = 4$ of O_2 is sufficiently populated that we can detect it.

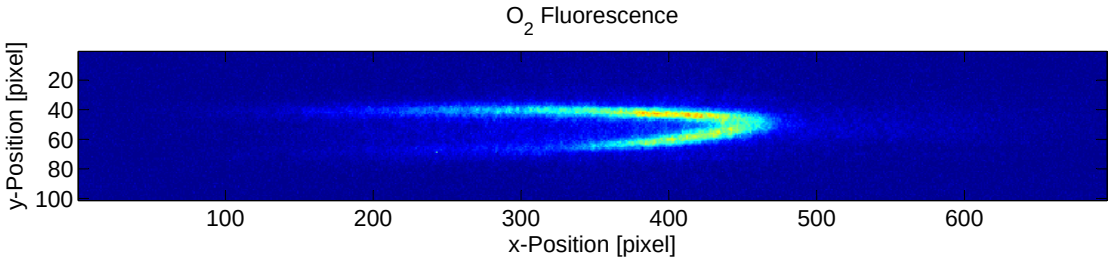

Figure 5.2.: O_2 fluorescence from the excitation of the O_2 R19(2-4) line within the catalytic reactor at 3 bar with an emission bandpass of 260 nm to 285 nm. The x-axis represents the channel length of the reactor and the y-axis the channel height. The upper and lower limits of the fluorescence mark the catalytic walls of the channel. For the image, the emission of 40 laser pulses was integrated on the CCD chip and averaged over 120 pictures.

5.4. Temperature Estimation

To allow for a temperature comparison with the combustion chemistry simulation, I estimated the temperature in the pre-reaction zone, marked with O_2 LIF. By scanning the laser wavelength, we can measure a ro-vibronic LIF excitation spectrum within the catalytic reactor when we average the fluorescence signal in the pre-reaction zone. Figure 5.3 shows a LIF excitation spectrum taken in the pre-reaction zone within the reactor (the exact location of the extraction is shown in Figure 5.4 C). In Figure 5.3, a clear O_2 spectrum can be seen compared to the Bunsen flame spectrum in Figure 5.1. At this distinct combustion condition in the reactor, NO was not present or detectable. The relative intensities of the (2-4) and (5-5) lines are proportional to their lower state populations, which are Boltzmann distributed. The temperature can then be extracted by matching simulations.

To ensure the accuracy of the temperature estimation, and in consideration of the results in chapter 7, it has to be shown that the O_2 LIF signal is not saturated by the laser intensity used. Therefore, a measurement of the LIF intensity versus the excitation intensity has been conducted, in which the beam energy was measured with a photodiode and the LIF signal with a photomultiplier. The beam energy was varied with the help of a beam attenuator. The results from this measurement are plotted in Figure 5.5. From this plot, it can be seen that the O_2 LIF signal increases linearly with increasing

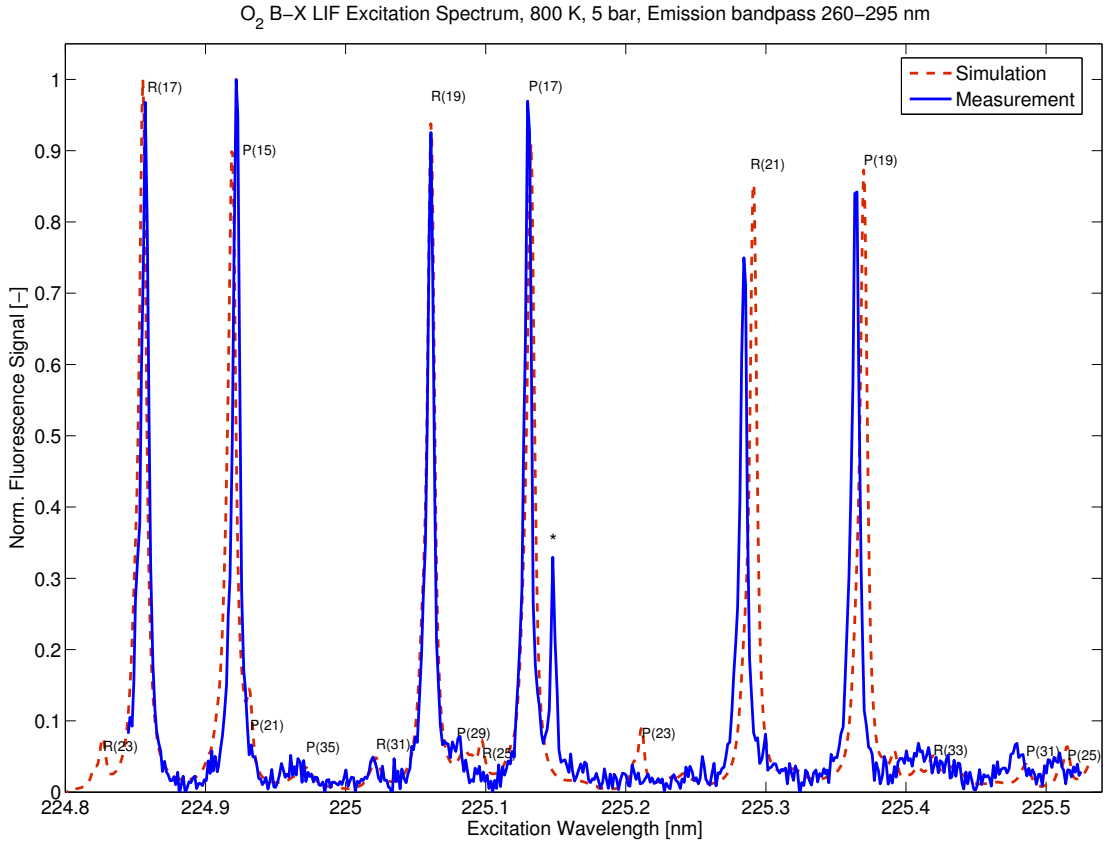

Figure 5.3.: O_2 LIF excitation spectrum measured within the catalytic reactor compared to a LIFSIM [92] simulation at 800 K.

excitation intensity and is therefore not saturated. Assuming the O_2 LIF signal being not saturated, the LIF excitation spectrum can be compared to LIFSIM calculations [92] in order to derive the temperature. I found good agreement with the simulation at approximately 800 K, as shown in Figure 5.3. As the (5-5) lines are barely visible, the accuracy of this temperature estimation is low.

Interestingly, an unexpected signal can be seen next to the P17(2-4) line at 225.15 nm, which does not match known LIF spectra in flames as reported in [109]. For this reason, it is attributed to a species X for the time being. As shown in Figure 5.4 B, the LIF signal from this species X is located towards the reaction zone, compared the the O_2 LIF signal. We could measure peaks of this species at 225.15 nm and 226.02 nm which relates to an energetic gap of 171 $cm^{-1} \pm 2\ cm^{-1}$. The large separation of the two lines indicates it being an atom or a light molecule. We observed a decreasing LIF signal of species X with decreasing CO concentration, which indicates it being a carbon-containing species. A more detailed investigation of this species is proposed for the future (e.g. emission

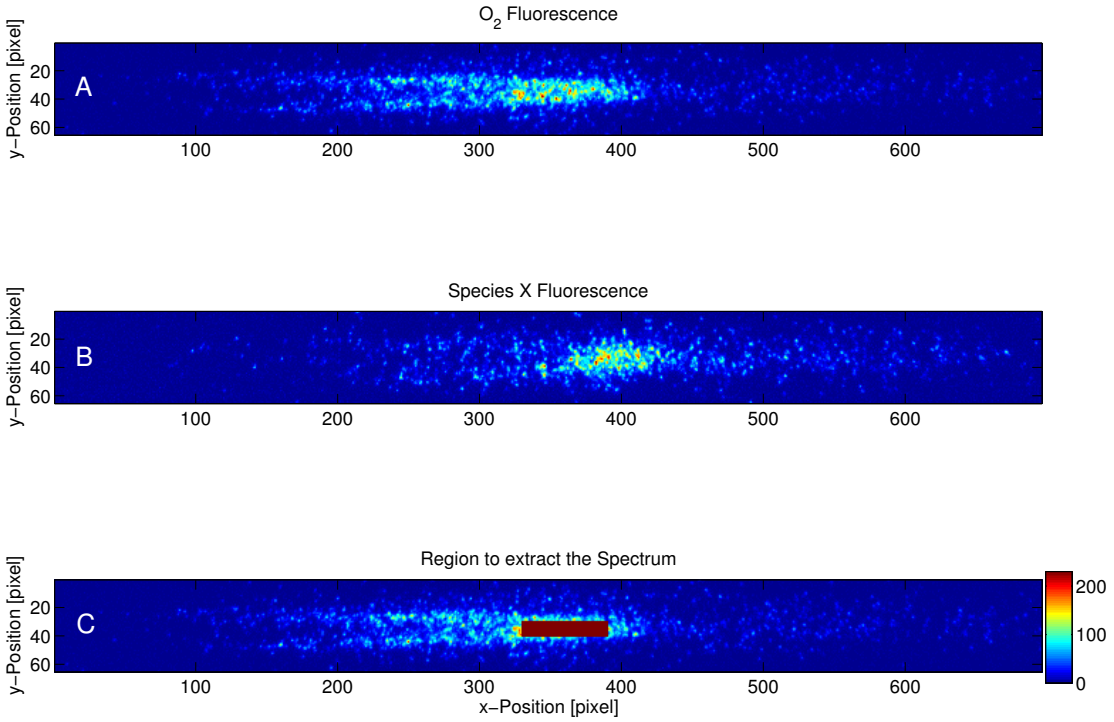

Figure 5.4.: Planar O_2 and species X fluorescence measured within the catalytic reactor and marker of the extraction region for the excitation spectrum taken with an emission bandpass of approx. 260 nm to 285 nm.

characteristics, further visibility) to identify the species and to know more about its applicability in flame diagnostics.

5.5. Comparison between O_2 and OH planar LIF

To verify the spatial position of the flame front measured with O_2 LIF and to relate it to our knowledge about OH LIF, we conducted a combined measurement of O_2 and OH LIF. A stationary operating point of the reactor at 3 bar was chosen which still allowed to detect OH LIF. We measured the fluorescence from O_2 and OH sequentially, which is shown in Figure 5.6. Comparing plots (a) and (b), it can be seen that the definition of the onset of the flame can be extracted from both LIF measurements. The combination of both LIF signals into one plot (c) clearly shows the production of OH downstream the consumption of O_2. To compare the results of the combustion chemistry model of Schultze et al. [110] with the measurements, we calculated the Boltzmann fraction of O_2 molecules in $v'' = 4$ from its 2-D O_2 mole fraction and temperature predictions. Plot (d) of Figure 5.6 shows this O_2 fraction in combination with the predictions of the OH

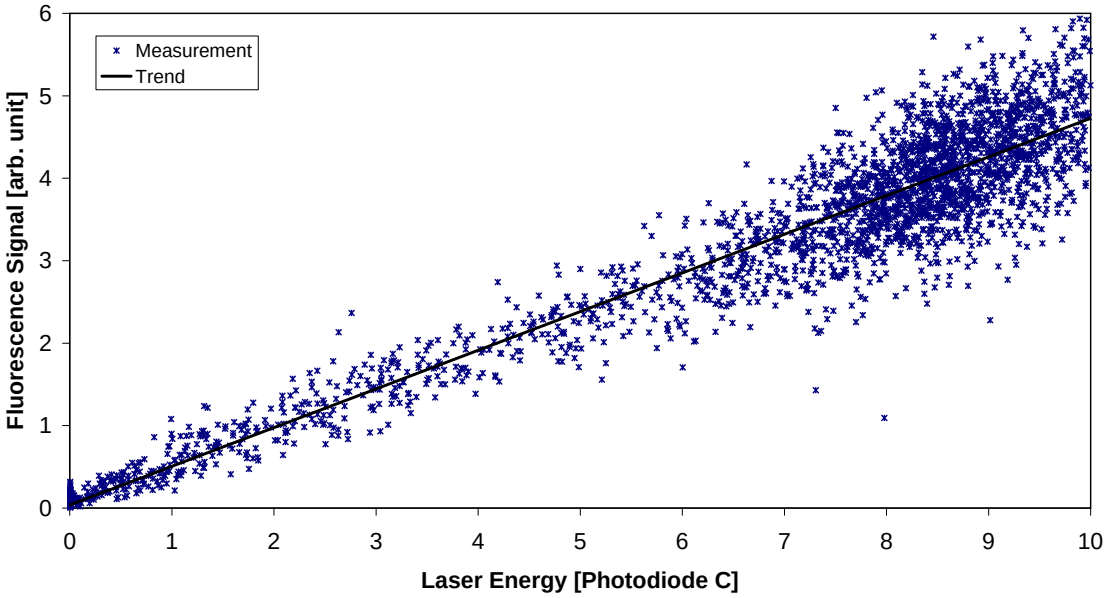

Figure 5.5.: O_2 LIF signal measured in a bunsen flame with a photomultiplier with an emission bandpass of approx. 250 nm to 260 nm versus the laser energy measured with a photodiode.

concentrations. The agreement between simulations and experiment is excellent. This result indicates the validity of the gas phase reaction mechanisms employed in the model by Schultze et al. [110].

5.6. Flame Front Definition with O_2 LIF in Rich Flames

Figure 5.7 shows the definition of the flame front with O_2 LIF in the catalytic reactor at different combustion conditions. It can be seen from this figure that with increasing pressure, the O_2 LIF shape gets more diffuse but we are still able to locate the flame front position with an uncertainty of less than ± 5 mm. Although the O_2 LIF signal increases with the pressure we still have to integrate and average the LIF signal over many laser pulses (at a laser pulse frequncy of 20 Hz, the integration of the LIF signal from 40 pulses and taking the average over 120 pictures the measurement time is roughly 4 min). When only changing the pressure, the O_2 LIF signal increases linearly with the pressure. But as we need to vary the flow rate of N_2 to stabilize the flame, we dilute the fuel mixture and the increase of the O_2 LIF signal is not as large as expected.
With increasing pressure, the absolute flow rate through the burner is also increased and

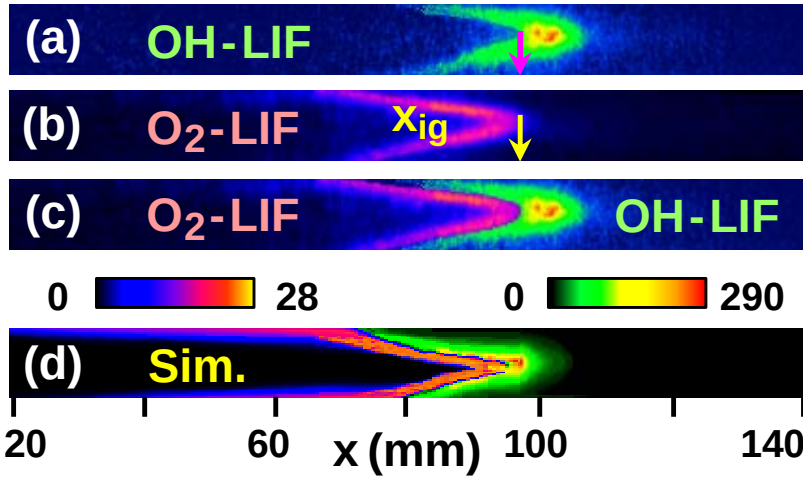

Figure 5.6.: Spatial comparison of planar O_2 and OH LIF within the catalytic reactor (H_2 : CO = 5 : 1, ϕ = 3, p = 3 bar) and additional comparison of the combined LIF to the combustion chemistry simulations [110], color codes indicate species mole fraction in ppm.

the flame starts moving slightly back and forth. From parts 6,7 and 8 in Figure 5.7 it can be seen that the flame stability depends not only on the pressure, but also on the fuel composition.

5.7. Discussion

I have shown that 2-D O_2 LIF can be used to define the ignition position of a flame with equal precision as with OH LIF for the investigated rich syngas flames. Defining the flame front through the vanishing LIF signal restricts this method to rich combustion. In lean flames, the O_2 LIF signal will persist in the reaction zone and within the exhaust. A definition of the beginning of the reaction zone in lean flames with O_2 LIF would be challenging if not impossible, as the competing effects of a decreasing LIF signal due to O_2 consumption and an increasing signal due to the elevated temperature need to be disentangled.

One of the advantages of the flame front detection with O_2 2D-LIF compared to the standard method of OH LIF is that, due to the predissociative nature of O_2, the LIF signal has a low sensitivity towards fluorescence quenching. Therefore we observe an increasing LIF signal with increasing pressure. On the other hand, the low fluorescence quantum yield of O_2 caused by predissociation, the additional frequency conversion

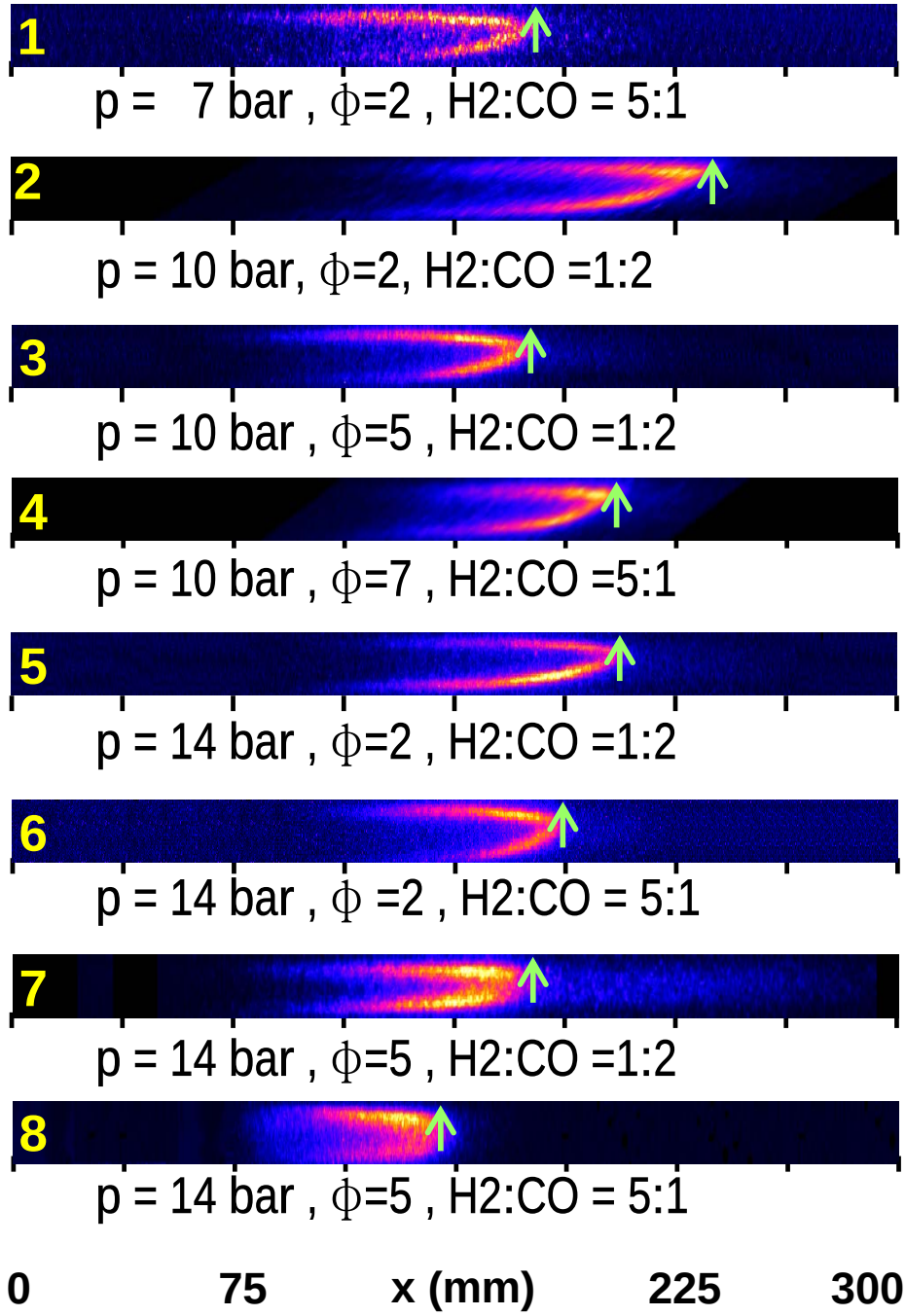

Figure 5.7.: Flame front detection with O_2 LIF in the catalytic reactor for different ratios H_2 : CO, different equivalence ratios ϕ and different pressures p. Color codes indicate O_2 mole fraction in ppm.

stage of the laser which reduces the laser power significantly, and the excitation of $v'' = 4$ resulted in a, for our detection system, rather low LIF signal. While the signal strength of OH LIF allows for single pulse flame front detection, for O_2 LIF the emission from several laser pulses must be summed on the ICCD chip, limiting the application in unsteady combustion.

	$T = 300$ K	$T = 500$ K	$T = 1000$ K	$T = 1500$ K	$T = 2000$ K
$v'' = 4$	$3.8 \cdot 10^{-13}$	$3.1 \cdot 10^{-8}$	$1.6 \cdot 10^{-4}$	$2.4 \cdot 10^{-3}$	$8.8 \cdot 10^{-3}$
$v'' = 5$	$2.4 \cdot 10^{-16}$	$4.2 \cdot 10^{-10}$	$1.8 \cdot 10^{-5}$	$5.7 \cdot 10^{-4}$	$3.0 \cdot 10^{-3}$
$v'' = 6$	$1.8 \cdot 10^{-19}$	$5.6 \cdot 10^{-12}$	$2.1 \cdot 10^{-6}$	$1.4 \cdot 10^{-4}$	$1.0 \cdot 10^{-3}$
$v'' = 7$	$1.3 \cdot 10^{-22}$	$7.5 \cdot 10^{-14}$	$2.4 \cdot 10^{-7}$	$3.2 \cdot 10^{-5}$	$3.4 \cdot 10^{-4}$

Table 5.2.: Boltzmann fractions for O_2 vibrational ground state level for different temperatures.

This drawback of O_2 LIF cannot be easily circumvented. To allow for single pulse O_2 LIF comparable to OH LIF, the LIF signal intensity of O_2 must be increased by roughly a factor of 1000. By changing the dye laser to a KrF excimer laser, the laser intensity can be increased roughly by a factor of 100. But with the KrF laser, only $v'' = 6$ and $v'' = 7$ can be excited. At the measured temperatures of about 1000 K, the Boltzmann fraction of $v'' = 6$ is roughly 100 times smaller compared to $v'' = 4$ (see Table 5.2) and thus we would not observe an increased LIF signal. With increasing temperature , the number density of O_2 decreases as T^{-1} but the Boltzmann fraction increases quickly (see Table 5.2). As a result, at 2000 K the signal for $v'' = 4$ increases 30 times and the one for $v'' = 6$ increases 200 times. The KrF excimer laser would be beneficial at higher temperatures: starting from 1500 K, the Boltzmann fraction of $v'' = 6$ is comparable to the one of $v'' = 4$ at 1000 K. The maximum signal we can expect with our setup would be at a flame temperature of 2000 K, considering the Boltzmann fraction of $v'' = 6$ and the KrF excimer laser. In this case, the O_2 LIF signal intensity could be increased by about a factor of 100, which is still not enough for single pulse measurements. But missing just a factor of 10 at these conditions is at least close to realizability. A detailed optimization of every individual component of the laser and the detection setup might allow improvements in this order. For the catalytic burner, these are hypothetic thoughts as it resists temperatures only up to 1300 K.
The overlap of the excitation and the emission of O_2 and NO requires an additional identification procedure to ensure the correct tuning of the laser to a spectrally separated O_2

excitation line. To optimize the O_2 LIF detection, we had to collect the light of several emission lines. Such a broad emission bandpass can not be realized with a combination of colored glass filters, we realized it instead with a setup of several reflection filters.

Summarizing, I can conclude that the definition of the flame front with O_2 LIF works well and precisely in the case of rich syngas combustion presented in this work. This method extends our capabilities for flame front detection to fuel compositions and combustion conditions where traditional LIF techniques as OH can not be applied anymore. However, when OH LIF is possible, I would recommend to use it instead of O_2 LIF, as OH LIF has a simpler setup, allows for single pulse measurements and can be applied in both fuel-lean and fuel-rich combustion.

6. Decomposition of O_2 Spectra by Non-Negative Matrix Factorization

In this section, I present results of the decomposition of an O_2 excitation spectrum into the contributions of its different vibronic transitions using a non-negative matrix factorization (NMF) algorithm and discuss the applicability for quantitative analysis.

6.1. Spectral Considerations

6.1.1. Excitation

For the following investigations, I used a tunable narrowband KrF excimer laser to excite O_2. Unless otherwise stated, the spectra are measured in a CH_4/air flame with $\lambda = 1.2$. The KrF excimer laser can directly produce UV light in the range of approximately 248 nm − 249 nm. In this excitation range O_2 transitions belonging to the ($v' = 0 \leftarrow v'' = 6$) and the ($2 \leftarrow 7$) bands of the O_2 B-X transition are dominant. Weaker O_2 transition from the $(1-6)$ and $(4-7)$ can also be observed as well as OH A-X $(3-0)$ transitions. Figure 6.1 shows a double-resolved emission/excitation LIF spectrum (as described in subsection 4.3.1) of the transitions which can be excited with the KrF laser. Compared to the 225 nm excitation with the YAG-Dye laser combination from the previous section, which provides about 2 mJ/pulse, the KrF laser provides up to 200 mJ/pulse. The higher laser energy allows for a wider adjustment of the laser intensity, which is important for the saturation investigation shown in chapter 7.

6.1.2. Emission

We can observe the emission from the above mentioned O_2 transitions in the range of approximately 220 nm - 330 nm. For the following measurements I used a spectrograph to resolve the emission. The grating I used with 1200 grooves per millimeter allowed to cover a range of about 45 nm. I chose to record the emission between 270 nm - 315 nm. For both excited states ($v' = 0, 2$) the emission to four ground state vibrational levels is captured (for $v' = 0 \rightarrow v'' = 9, 10, 11, 12$ and for $v' = 2 \rightarrow v'' = 10, 11, 12, 13$) in this

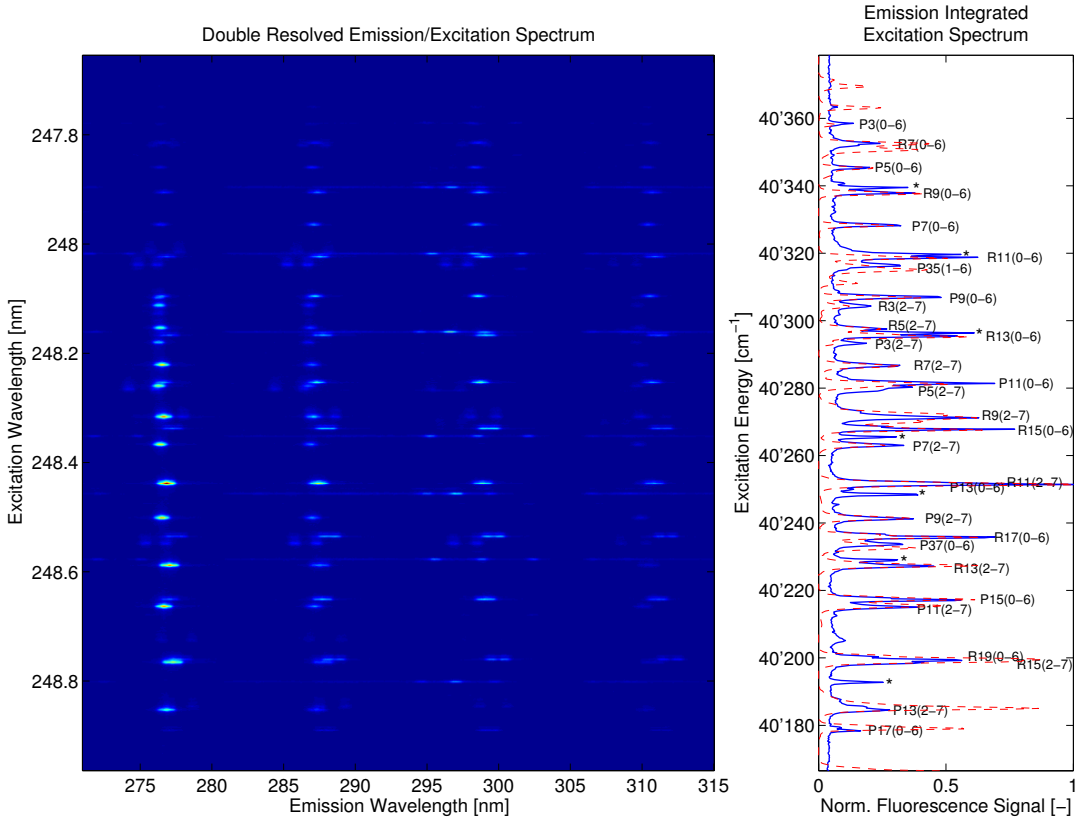

Figure 6.1.: Double-resolved emission/excitation spectrum and emission integrated excitation spectrum, measured with a KrF laser in the hot exhaust of a CH_4/air flame, emission bandpass approx. 270 nm − 315 nm. Asterisks mark OH transitions belonging to the A-X $(3-0)$ band.

range, which is shown in Figure 6.2. The emission of the $v' = 2 \rightarrow v'' = 12$ transition is three orders of magnitude weaker than the emissions of $v' = 2 \rightarrow v'' = 10, 11$, or 13 due to the lower Franck-Condon factor (see Figure A.1). This characteristic is helpful to identify and separate the emission from the two different excited vibrational states.

6.2. Reasons for the Decomposition

In one of the sparse literature results concerning pressure dependent O_2 LIF, Sick et al. [45] proposed a method how O_2 LIF spectra taken at different pressures can be used to investigate quantitatively fluorescence quenching of different vibrational levels of the predissociative $B^3\Sigma_u^-$ state of O_2. The idea is to excite two ro-vibronic transitions leading to states with different predissociation rates. The excited state with the lower predissociation rate has the longer lifetime and is stronger affected by fluorescence quenching.

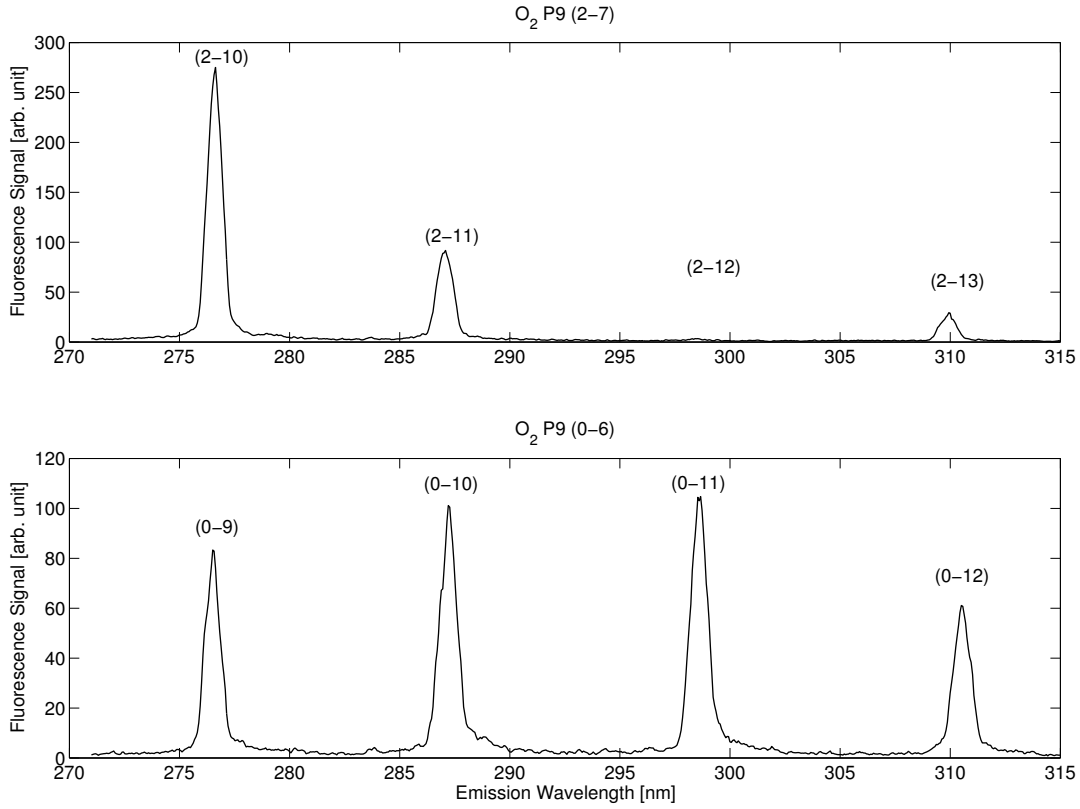

Figure 6.2.: Comparison of emission spectra for different ro-vibronic O_2 excitations, measured with a KrF laser in the hot exhaust of a CH_4/air flame.

The difference in predissociation rates is used as an internal clock to estimate quenching rates. Transitions of the (0-6) and (2-7) bands of the O_2 B-X Schumann Runge bands can be used for this investigation, as the predissociation rate of $v' = 0$ is three times smaller than the one of $v' = 2$ (the data are taken from Bessler et al. [92]). Therefore, as fluorescence quenching increases with pressure, the relative intensity of the (0-6) band should decrease.

The important part of this investigation is to extract the fluorescence contribution of the different transitions from the spectrum. One way would be to always extract the peak LIF intensities of the transitions, providing the line widths are known. This can only be done for non-overlapping lines, which decreases the amount of comparable lines significantly. The peak intensity is very sensitive to the laser tuning, experimentally it is very difficult to ensure the tuning for all lines to their exact maximum. The consequent extraction of the intensity slightly off the peak can result in large errors. Another way would be to compare the measured spectra to model calculations with LIFSIM [92]. For every excitation line a fit to the measurements would be required, which allows to

extract the integrated fluorescence. Being able to compare the integrated fluorescence instead of the peak intensity would be an improvement as the integrated fluorescence is less sensitive to laser tuning, and overlapped transitions can be disentangled. On the other hand, this method requires knowledge of the wavelength-dependent transmission characteristics of the emission detection setup to be able to compare the results of the fits. I propose another method, in which the spectrum can be decomposed with a non-negative matrix factorization algorithm (NMF, described in section 3.1). This method has been successfully applied in very different tasks, e.g. text mining for email surveillance or in spectroscopy for so-called spectral unmixing problems [98] e.g. for spatially non-resolved space object characterization or particle identification in atmospheric chemistry. To the best of my knowledge, this method has not yet been applied in LIF investigations. The advantage of this method is that no spectral knowledge or experimental transmission properties need to be known.
The aim of this investigation is to see, whether the NMF decomposition can provide equally accurate results of the LIF intensity ratios compared to e.g. the measurements in Sick et al. [45]. They calculated the fluorescence by integrating the emission spectra at the peak intensity of a transition.

6.3. NMF of Synthetic Spectra

To estimate the quality of the decomposition with the NMF method, I created double resolved emission/excitation spectra built up from the measured (0-6) and (2-7) emission spectra shown in Figure 6.2 and synthetic excitation spectra as shown in Figure 6.3 A. The synthetic excitation consists of eight Gaussian peaks which I used for the (0-6) transitions and ten Gaussian peaks for the (2-7) transition. I varied the overlap of the peaks from complete overlap (pair 1 in Figure 6.3 A) over partial overlap (pairs 2-7) to no overlap (pair 8). For simulating the experimentally expected unequal peak intensities, the integral of the peaks for the (2-7) transitions is twice as large as the ones for the (0-6) transitions. To resemble measurement conditions I added a randomized noise of 3 % proportional to the signal and a background signal of 2 % of the maximum signal value to the excitation spectra.
For the verification of the convergence of the NMF, I created a constant emission spectrum (shown in Figure 6.3 B) that contains the two emissions of (0-6) and (2-7). I used the NMF to identify two different emission spectra ($k = 2$ in Figure 3.1, called spectral signatures in Berry et al. [98]). I could assign the identified spectral signatures to (0-6) or (2-7) by the position of their highest emission peak. Afterwards I fitted Gaussian functions to the identified spectral contributions for the different vibronic emission.

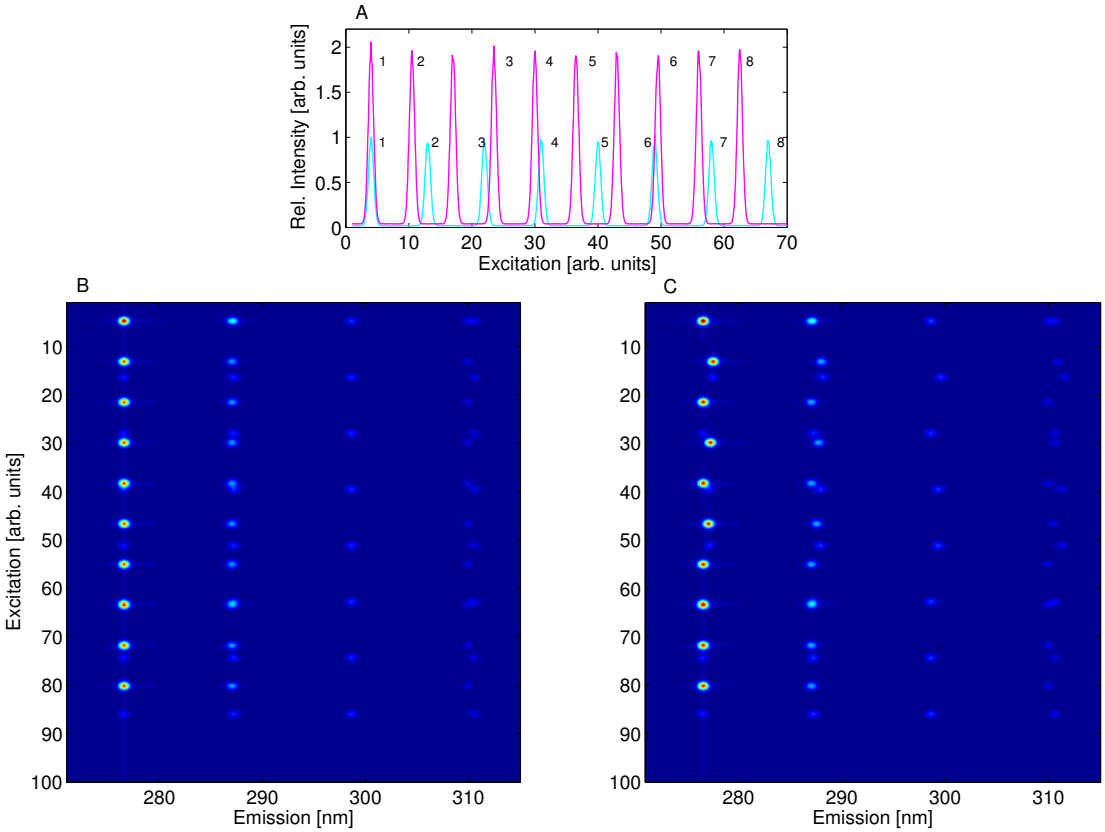

Figure 6.3.: Artificially generated spectra to test the decomposition of O_2 spectra with the NMF method.

Then I calculated the ratios of the integral intensities for the peak pairs as annotated in Figure 6.3 A. The deviation from the given ratio of two relates to the accuracy of the NMF (the introduced random noise has an influence of less than 0.5 % and can therefore be neglected). For this spectrum, the NMF identifies the spectral signatures with almost no variation to the given emissions. The graphical results are shown in Figure A.5. The statistical analysis of 100 decompositions of the spectrum is shown in Table 6.1.
The decomposition works best for separated lines (pairs 2,5,7 and 8). The largest deviation of 11 % is found for the completely overlapped lines of pair 1. The very low values of the standard deviation indicate that for the chosen synthetic spectrum, the NMF converges always to very similar results.
To achieve a more realistic spectrum, in which the emission is shifted in wavelength for the P- and R-branches and due to different rotational quantum numbers, I created a spectrum in which the given emission spectra are also shifted, as shown in Figure 6.3 C. For the statistical analysis I also recreated the random noise and background signal for

Pair	1	2	3	4
Peak Ratio	1.81 ± 0.006	1.96 ± 0.004	1.93 ± 0.004	1.88 ± 0.006
Relative Error	9.5 ± 0.3 %	1.8 ± 0.2 %	3.7 ± 0.2 %	6.2 ± 0.3 %
Pair	5	6	7	8
Peak Ratio	2.01 ± 0.004	1.80 ± 0.006	1.99 ± 0.004	1.98 ± 0.004
Relative Error	0.5 ± 0.2 %	10.1 ± 0.3 %	0.5 ± 0.2 %	1.0 ± 0.2 %

Table 6.1.: Extracted peak pair ratios ± the standard deviation resulting from the decomposition of the artificial spectrum shown in Figure 6.3 B with the NMF method (the peak pairs from which the ratios are built are depicted in Figure 6.3 A). The relative error is based on the given peak ratio of 2.

each of the 100 decompositions. I used the NMF to identify six spectral signatures, which I assigned to (0-6) and (2-7) by their highest peak location. For this spectrum, the NMF normally identified two (0-6) and four (2-7) spectral signatures. The analysis of the 100 decompositions is shown in Table 6.2.

For this case including shifted emission, it can be seen that the decomposition deviates up to 70 % from the given value, which is too high to be able to draw meaningful conclusions from the decomposition. The standard deviation is also strongly increased. A detailed analysis of the single decompositions showed that the NMF converges not always to spectrally meaningful signatures. Also spectral signatures are identified which are a mixture of the two given signatures and which can therefore not clearly be attributed to one of them. By a comparison of the relative peak intensities of the spectral signatures with the given emission spectra I defined a criterium to judge whether the identified signatures are physical: for this synthetic spectrum I compared the emission of the first peaks around 278 nm for the identified (0-6) spectral signatures. I considered as unphysical if the intensity of these peaks varied more than 25 %. Checking the NMF results with this criterium showed that for the present spectrum, about 40 out of 100 NMF decompositions provided physically correct decompositions. It needs to be mentioned that the number of decompositions that provide correct results also depends on the number of spectral signatures the NMF is given to identify. I found that for four or six signatures the NMF provided physical results most often. For a chosen higher number of signatures the NMF identified physically correct signatures significantly less often.

In the lower part of Table 6.2, I show NMF results for 100 decompositions that passed the above mentioned criterium.

Pair	1	2	3	4
Peak Ratio	2.26 ± 2.18	3.00 ± 0.14	2.30 ± 1.08	2.62 ± 0.18
Relative Error	13 ± 109 %	50 ± 7 %	15 ± 54 %	31 ± 9 %
Pair	5	6	7	8
Peak Ratio	2.69 ± 0.20	2.26 ± 2.18	2.20 ± 1.10	2.20 ± 1.06
Relative Error	34 ± 10 %	13 ± 109 %	10 ± 55 %	10 ± 53 %

Unphysical decompositions sorted out

Pair	1	2	3	4
Peak Ratio	2.05 ± 0.16	2.72 ± 0.06	2.17 ± 0.14	2.33 ± 0.06
Relative Error	2.5 ± 8.2 %	36 ± 3.1 %	8.7 ± 6.8 %	16 ± 3.0 %
Pair	5	6	7	8
Peak Ratio	2.36 ± 0.06	2.05 ± 0.16	2.11 ± 0.12	2.12 ± 0.12
Relative Error	18 ± 3.0 %	2.6 ± 8.1 %	5.7 ± 6.2 %	6.0 ± 6.0 %

Table 6.2.: Extracted peak pair ratios ± the standard deviation resulting from the decomposition of the artificial spectrum shown in Figure 6.3 C with the NMF method (the peak pairs from which the ratios are built are depicted in Figure 6.3 A). The relative error is based on the given peak ratio of 2. Decompositions which yield unphysical spectral signatures were not considered in the results shown in the lower table.

It can be seen that such a selection improves the NMF method significantly. Even the completely overlapped lines can be well decomposed with an uncertainty of about 15 %. The highest deviation is found for pair 2 of about 35 %. The graphical decomposition shown in Figure A.6 indicates that for pair 2 the decomposition cannot be clearly attributed to one of the spectral signatures. This pair indicates a limitation of the NMF capabilities with respect to the decomposition. But for the present synthetic spectrum and the experimental spectra discussed in the following sections, a graphical comparison with the initial data allows to identify such incorrectly decomposed pairs (see Figure A.6 D and F). For the quantitative analysis those pairs must not be considered. The standard deviation decreased to less than 10 % for all decomposed pairs.
Summarizing I can state that, when the decomposition using the NMF converges to physical results, well separated lines can be reproducibly decomposed with an uncertainty in the order of $5 - 15$ %. Even totally overlapped lines can be meaningfully decomposed.

The challenge is to identify a physically meaningful decomposition with an appropriate criterium using the experimental data.

6.4. Decomposition of Measured O_2 Spectra

For the following decomposition, I used a part of the spectrum shown in Figure 6.1 from 248.0 nm - 248.9 nm with the largest transition intensities. Concerning the decomposition, several observations can be made from Figure 6.1. Different emission spectra (or spectral signatures Berry et al. [98]) of the O_2 (0-6) and (2-7) transitions can be recognized. The emission of OH shows a different spectral signature compared to the O_2 transitions. This is beneficial for the NMF method, as the more different the spectral signatures are the better they can be distinguished. It can also be seen that some of the spectral signatures are very close to each other, partially they even overlap in the 2-D spectrum. In the emission integrated spectrum this overlap is even more pronounced.
For the spectral decomposition in this study, I want to differentiate between three contributions to the spectrum: O_2 emission from $v' = 0$, $v' = 2$ and OH emission. Empirically, I found that the identification of six spectral signatures produced the best decomposition, with two signatures converging to each emission spectrum of O_2 (0-6), (2-7) and OH.
Choosing a higher number of spectral signatures to be identified caused the problem that the decomposition converged to spectral signatures, which I could not clearly attribute to one of the emission spectra of a present transition.
Figure 6.4 shows the six spectral signatures identified with the NMF method, grouped by a comparison with the emission spectra in Figure 6.2 and their contributions to the emission-integrated excitation spectrum. The contributions from weaker transitions, as well as the background contributions are distributed over the spectral signatures of the dominant transitions. To estimate the quality of the decomposition, I compare in Figure 6.5 the contributions of the decomposed species against the excitation spectrum. From this plot, it can be seen that the NMF separates the spectrum well, even partly overlapping emissions as e.g. the P11(2-7)/P15(0-6) lines or the P7(2-7)/R9(2-7)/R15(0-6)/OH lines and the completely overlapping R11(2-7)/P13(0-6) transitions. The P9(2-7) line can be used to estimate whether the identified spectral signatures are mixed (which means unphysical decomposition) or correctly separated. On the other hand, it can be seen that for all OH peaks, a small contribution is attributed by the decomposition to randomly one of the O_2 transitions. Also, e.g. the weak P37(1-6) transition is in parts attributed to all base vectors.

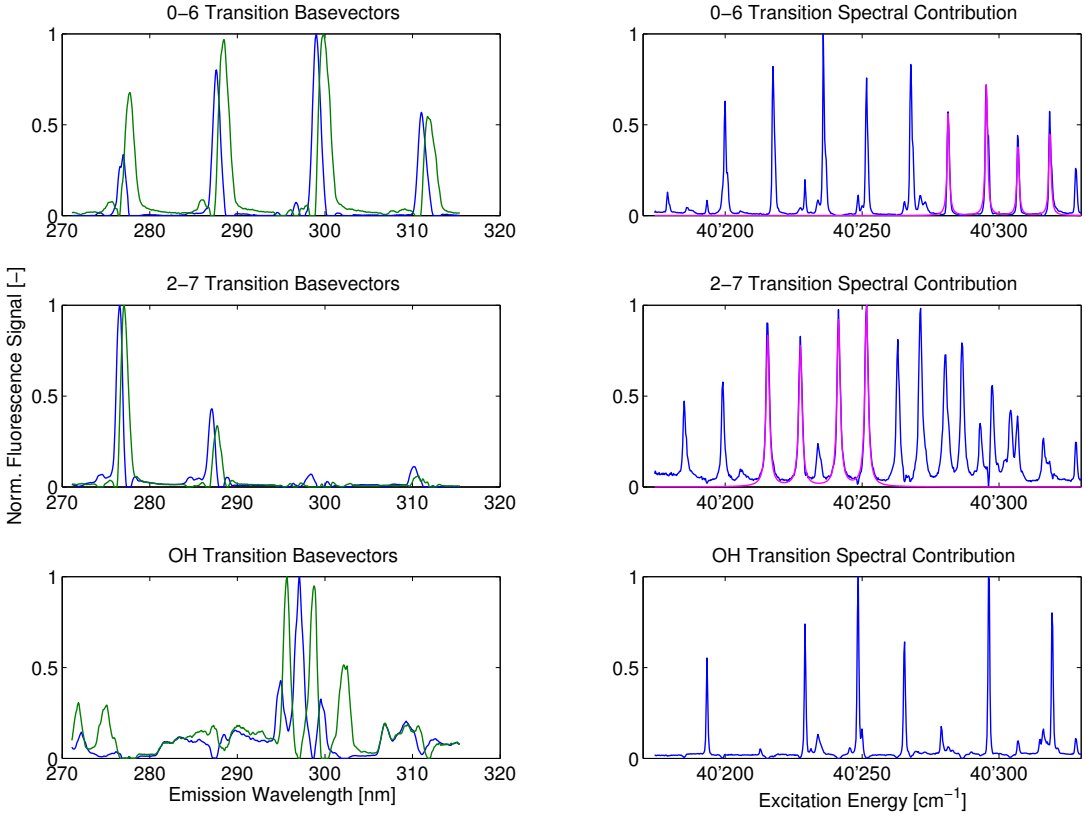

Figure 6.4.: NMF decomposition into six spectral signatures qualitatively grouped according to Figure 6.2 and the corresponding spectral contribution. Lorentzian fits to the spectral contributions are shown in magenta.

6.5. Separation of Species Spectra with NMF

One of the possible applications of the NMF decomposition is to extract the spectrum of a single species. In Figure 6.6 I show the extracted O_2 spectrum and compare it to the measurement. It can be seen that besides the OH contribution, also parts of the background and the weak (1-6) transitions are subtracted. As mentioned above, these contributions are spread over all the spectral signatures, but in the present case the OH contribution includes the largest share for the background signal. The overall line intensities as well as the peak intensities of the NMF extracted O_2 spectrum are almost not affected by the decomposition, which enables a precise quantitative analysis.

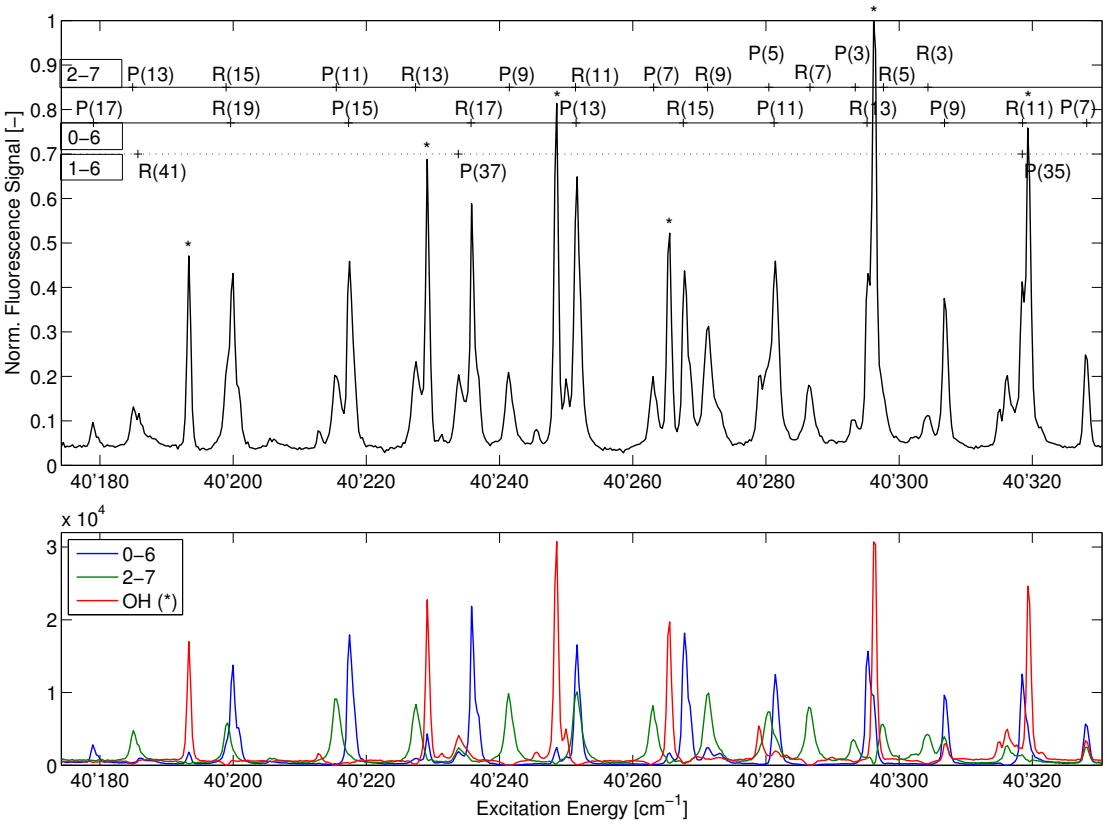

Figure 6.5.: Comparison of the NMF decomposed spectral contribution with the emission integrated excitation spectrum from the measurement in which the transitions are identified with LIFSIM calculations [92].

6.6. Comparison of the Fluorescence from Two O_2 Emission Bands

To compare results of the NMF decomposition with the findings from Sick et al. [45], I recorded a series of double-resolved emission/excitation spectra at different pressures. All the spectra were decomposed to extract the contribution of the two different O_2 bands. Then I fitted a Lorentzian function (see Figure 6.4) to each excitation line in order to integrate the fluorescence. The ratios of the fluorescence from different ro-vibronic transitions are shown in Figure 6.7, for two series of measurements with different laser intensities. To minimize the influence of the rotational state on the observed quenching rates, I compared the same rotational transitions from different vibronic bands (P9, P11, R11, R13. Their relevant spectroscopic properties are listed in Table A.2). As the same rotational transitions for $v' = 0$ and $v'' = 2$ are are observed at very different excitation

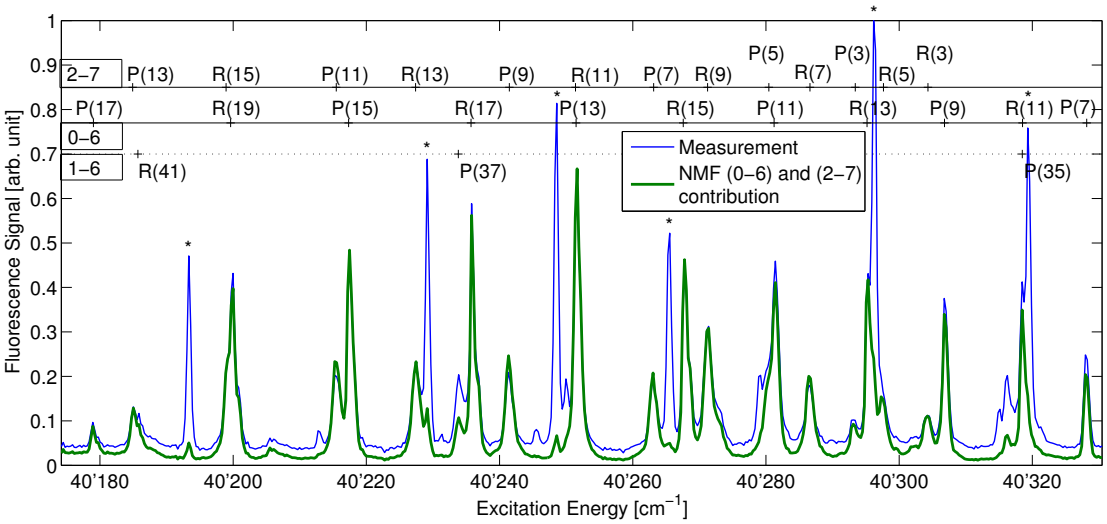

Figure 6.6.: NMF decomposed spectrum without the contribution of OH (*) compared to the emission integrated excitation spectrum with transitions referenced.

positions (see Figure 6.4, towards the lower and upper boundaries of the excitation range), I need to account for the frequency-dependent transmission characteristics of the experimental setup. Therefore, the ratios in this plot have been normalized with the mean value of the corresponding ratio of the lower laser intensity measurement. From Figure 6.7, it can be seen that ratios measured with a higher laser intensity decrease with increasing pressure, whereas the ratios measured with the lower laser intensity do not exhibit a clear trend.

6.7. Discussion

I have shown that the qualitative decomposition with the NMF method of the flame spectrum into the different contributions of O_2 and OH provided good results. For this investigation, the emission spectra were already known for O_2 transitions [92], which allowed to group the spectral signatures accordingly and on the other hand to confirm that the identified spectral signatures have a physical justification. The OH emission spectra, which are clearly different from the O_2 emission spectra were also identified. Thus, I can assume that a decomposition with the NMF method can be used also to determine different spectral signatures even when they are unknown.
The fluorescence ratios shown in Figure 6.7 can be used to estimate the accuracy of the NMF for quantitative analysis. From a theoretical point of view, the fluorescence ratios taken for ro-vibronic transitions of the (0-6) and (2-7) bands are independent

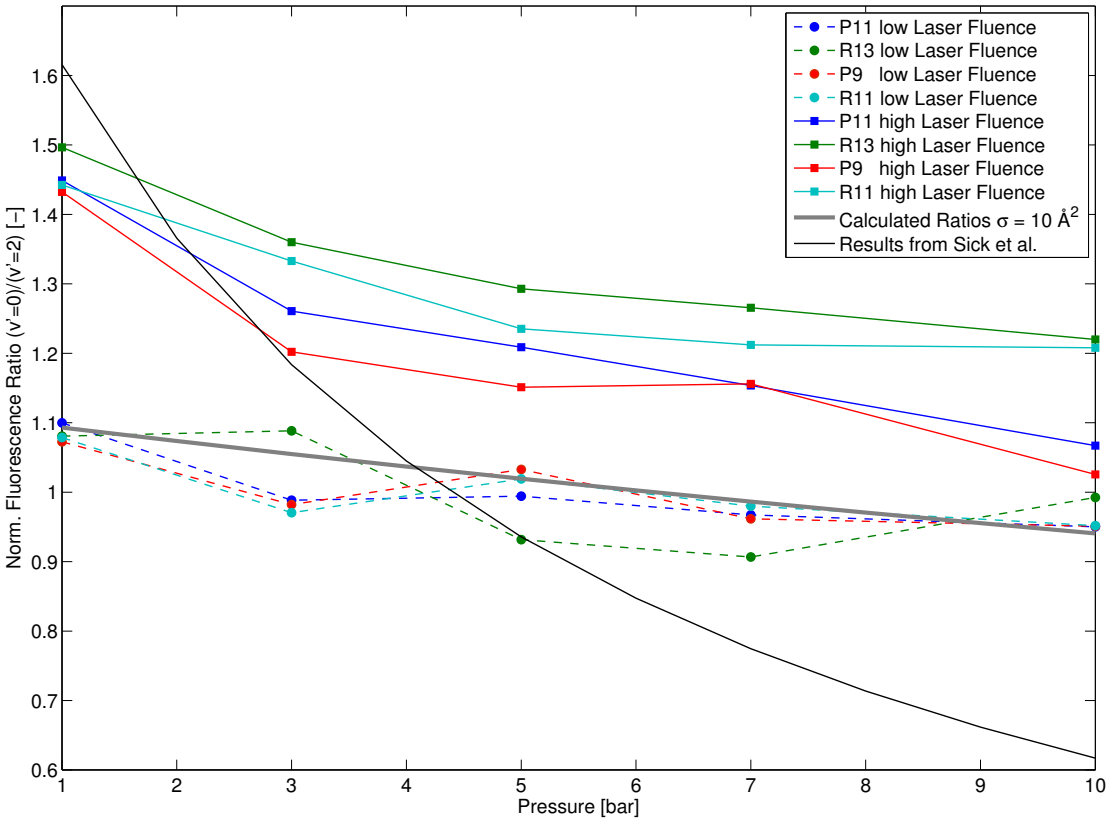

Figure 6.7.: Comparison of the ratios of integrated fluorescence calculated with the NMF method for different laser intensities. The ratios are taken for (0-6) and (2-7) transitions with same J and compared to the results from Sick et al. [45].

from J at the same pressure, as the ratios of the LIF relevant physical quantities (e.g Einstein A and B coefficients, predissociation lifetime) are the same. Therefore, the variation of the ratios of the different ro-vibronic transitions at the same pressure can be related to the accuracy of the NMF method. A contribution to the variation is the above mentioned random attribution of the background and the minor transitions to the dominant spectral signatures. Thus, I can estimate the accuracy to be $\pm 6\,\%$.

Sick et al. [45] proposed to use the fluorescence ratios shown in Figure 6.7 to obtain the pressure dependent quenching rate constant Q. The idea is, to use the difference in predissociation lifetime of $v' = 2$ and $v' = 0$, which is about a factor of three, as internal clock. The ratio of the fluorescence from $v' = 2$ and $v' = 0$ described by the quantum yield $\varphi = A/(A + P + Q)$ would be independent from the pressure for quenching rates much smaller than the predissociation rates P ($P >> Q$), as A and P are pressure-independent molecular constants [10, 45]. If Q is in the order of P,

the ratios of quantum yields would exhibit a pressure dependence. The reason why I investigated the fluorescence ratios at two different laser intensities, as depicted in Figure 6.7, arises from the fact that Nguyen and Paul [29] have shown that depletion of the ground state population can have an influence on the quantitative analysis of predissociative O_2 LIF with high energy lasers, such as the KrF laser. The depletion of the ground state, which causes the saturation of the LIF signal depends on the laser intensity and on the pressure. From Figure 6.7 it can be seen that the fluorescence ratios measured with the higher laser intensity ($0.64\,\mathrm{mJ/mm^2}$ or $3 \cdot 10^{10}\,\mathrm{W/m^2}$) decrease with increasing pressure, but the decrease is not nearly as strong as Sick et al. [45] have reported who used a higher laser intensity of $10\,\mathrm{mJ/mm^2}$ or $50 \cdot 10^{10}\,\mathrm{W/m^2}$. For the lower laser intensity ($0.13\,\mathrm{mJ/mm^2}$ or $0.6 \cdot 10^{10}\,\mathrm{W/m^2}$) the decrease of the fluorescence ratios with increasing pressure almost vanishes. This observation indicates that the decrease of the fluorescence ratios $\varphi(v' = 0)/\varphi(v' = 2)$ is related to saturation and not to quenching. Following the approach of Sick et al. [45], I added to Figure 6.7 calculations of the fluorescence quantum yield ratios to match the measurements with the lower laser intensity, which are the least influenced by saturation. This allows me to derive an upper bound for the quenching rate, assuming that the decrease of the fluorescence ratios is solely due to quenching. I found good agreement for $Q = 5 \cdot 10^8\,\mathrm{s^{-1}bar^{-1}}$, assuming that the quenching cross section is equal for both excited vibrational states. This can be translated according to Equation 2.14 to an upper limit of the quenching cross section at $10\,\mathrm{Å}^2$.
This result differs strongly from the values found by Sick et al. [45] who report $\sigma_Q(v' = 0) \approx 100\,\mathrm{Å}^2$ and $\sigma_Q(v' = 2) \approx 30\,\mathrm{Å}^2$ and I explain this discrepancy with the fact that they did not consider saturation in their work.

Summarizing the results above I can conclude that the NMF allows well for a qualitative decomposition of the measured excitation/emission spectrum into contributions of different O_2 vibronic bands and OH. The NMF is also well suited for quantitative analysis. The disagreement of the results with the work of Sick et al. [45] lead to a detailed study of the laser intensity caused saturation effect of O_2 LIF presented in the following sections.

7. Quantitative Analysis of Saturated O_2 LIF

In this section, I introduce a modeling scheme for the saturation of O_2 LIF. A three-level model is proposed for the analysis and its validity and applicability are discussed. A quantitative analysis of RET resulting from the comparison between measurements and model calculations is reported and discussed.

7.1. Spectral Considerations

7.1.1. Selection of Transitions

For an accurate measurement of the LIF saturation of a certain O_2 transition, the laser has to be tuned to the position, where the emission intensity peaks. To avoid the excitation and therefore an influence of the transitions in the vicinity, transitions with a clear separation from neighboring lines are preferably used for the measurements. From the spectrum in Figure 6.1 can be seen that the P9(2-7) line and the P9(0-6) line are well suitable for measurements due to the good separation from neighboring lines. This pair of lines allows to compare the identical rotational transition of different vibronic bands. To compare different rotational transitions of the same vibronic band, I chose for the same reasons additionally the P15(0-6) line. The relevant spectroscopic properties of these transitions are listed in Table A.1.

7.1.2. Laser Intensity

When investigating the LIF saturation effect of an O_2 transition, the laser intensity (in $[\,\mathrm{W/m^2}]$) is the parameter to be varied The upper limit is a combination of the maximum laser energy and tight focusing. The KrF laser provided about 200 mJ/pulse maximum output energy. To increase the intensity the beam was focussed. For the calculation of the laser intensity, I assume the same intensity for the whole observed area. The more strongly the beam is focused, the more Gaussian-shaped the beam profile becomes, which means the larger the so-called wings of the beam [14] become, in

which the laser intensity will partially not be sufficient to saturate. Two aspects of this effect need to be considered. If focusing is too strong, a large part of the fluorescence comes from the non-uniform wings and only a small part from the region of the beam which is able to saturate. The other aspect relates to strong saturation. When the laser intensity is much stronger than the saturation intensity as defined by Eckbreth [14], the LIF signal should be independent of the laser intensity. But even if the wings are very small, the LIF signal will change when varying the laser intensity, which does in this case not allow to quantify the saturation correctly. Therefore, the maximum laser intensity is a compromise between focussing strong enough to observe saturation and ensuring that the wings of the beam profile have a minimal effect on the measurement. The lower limit of the laser intensity is defined by the dynamic range of the attenuator to about 10 % of its maximum value.

7.1.3. Characteristics of the Saturation

For measuring the saturation of O_2 LIF, I recorded the O_2 fluorescence integrated between 270 nm-315 nm while varying the laser power with a beam attenuator (see section 4.1). Figure 7.1 shows saturated O_2 LIF measured at different pressures and for different ro-vibronic transitions. Several important characteristics of the saturation can be seen in this plot. With increasing pressure, the saturation of the P9(2-7) transition decreases. As shown by Rothe et al. [30] for OH, the saturation is a consequence of ground state RET, and RET increases with pressure (see subsection 2.3.1). Therefore, the saturation decreases with pressure. Another important characteristic is that the saturation effect is differently pronounced for the (0-6) and (2-7) transitions. The Franck-Condon factor and therefore the excitation rate for the (0-6) band is roughly 30 times smaller compared to the (2-7) band. As a consequence, at 1.5 bar, saturation is weak for the the (0-6) transitions compared to the (2-7) transitions. Therefore, I had to measure the saturation of the (0-6) transitions at sub-atmospheric pressures.

7.2. Evaluation of a Kinetic Model for Saturated O_2 LIF

In this section, I discuss which kinetic model for the population exchange of O_2 LIF and which boundary conditions are suitable to represent the saturation curves. Model fits to measurements are presented and compared for a three-level kinetic model and a more detailed RET model based on rotational state-to-state rates.

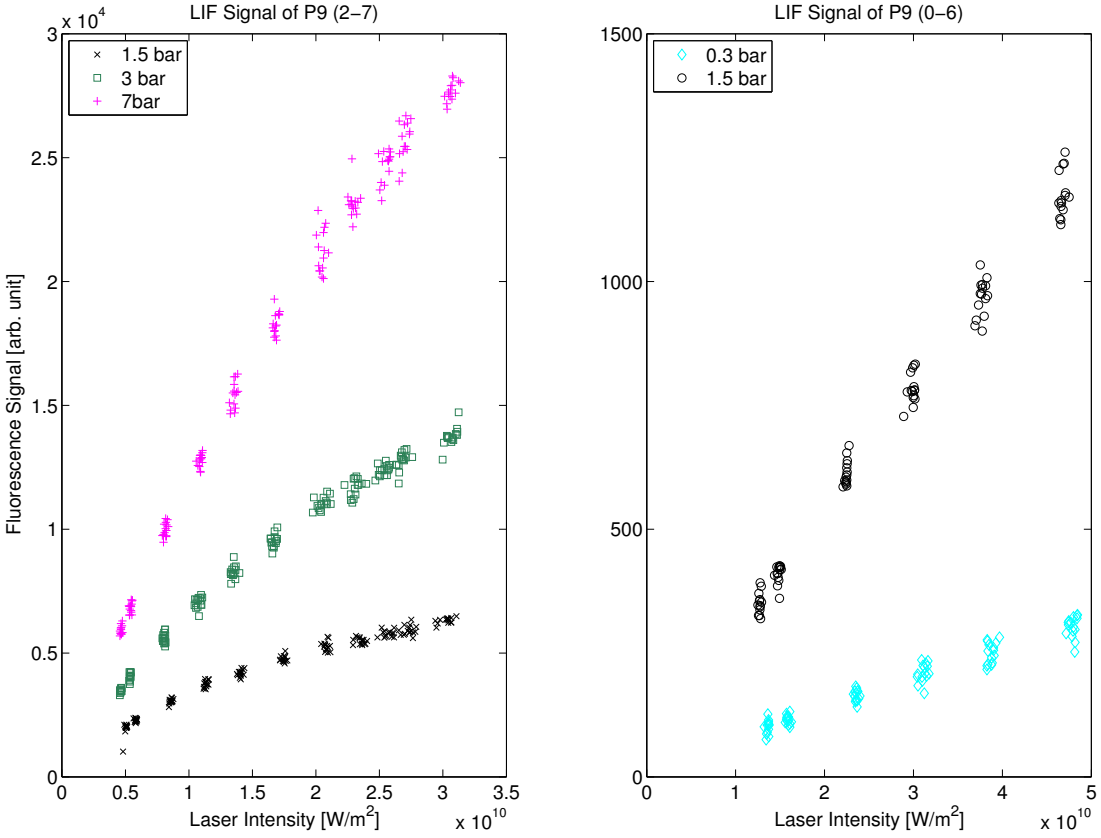

Figure 7.1.: Comparison of O_2 LIF signals vs. laser intensity for a (2-7) and a (0-6) transition at different rressures, same pressure values are shown with same colors.

7.2.1. Comparison between Measurements and Models

Figure 7.2 shows exemplarily a model fit to a saturated O_2 LIF measurement of the P9(2-7) line. The model calculation is the result of a least-squares fit of the three-level model with unlimited-pool approximation to the measurements with as the fitting parameters Q_{RET} and the fluorescence constant FC (see section 3.2). As a comparison, the red-dashed line shows the hypothetic unsaturated case under these conditions.

7.2.2. Three-Level Model with Limited-Pool State

As shown in section 3.2, the O_2 LIF can be described by a three-level model. The determination of the pool state size for the limited-pool assumption is based on the knowledge of the Boltzmann distribution of the rotational states (Equation 3.8). For the O_2 molecule, the rotational states are split up into three components, caused by the

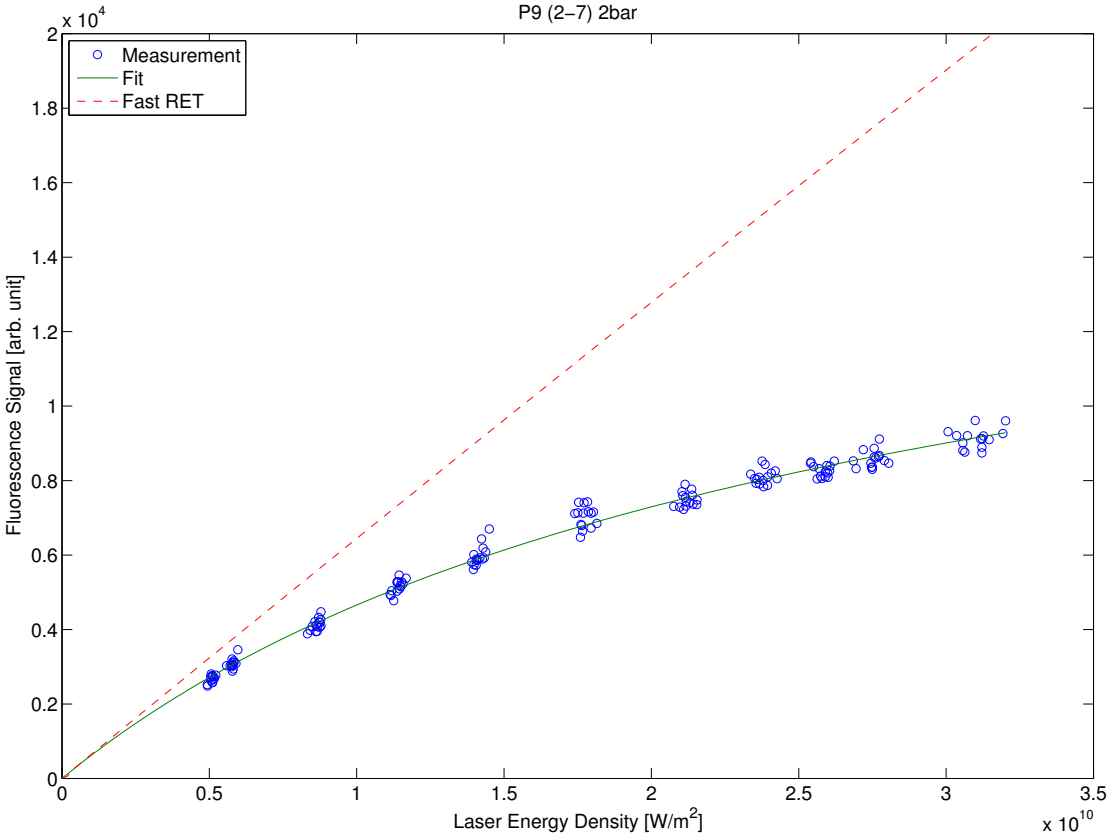

Figure 7.2.: Comparison of a three-Level model calculation with unlimited pool state fit to a saturated LIF measurement of the P9(2-7) Line at 2 bar and to the hypothetic unsaturated LIF signal.

spin-rotation coupling (components are denoted with superscript s, $s = F1, F2, F3$). Figure 7.3 shows the Boltzmann fractions of one spin component of the rotational states of O_2 molecules for the vibrational state $v'' = 7$ at 2000 K and as a reference, the fractions at room temperature. For the P9(2-7) transition at 2000 K, the population of the $J^s = 9$ state $N^{s0}_{J=9} = 1/30$ of the total population, therefore the pool can be estimated to be approximately $29N^{s0}_{J=9}$.

Figure 7.4 shows results of three-level model fits with a limited pool to measurements at different pressures. It can be seen that model is able to fit data at 1.5 bar and 3 bar well. For pressures above 3 bar the model over-predicts the LIF signal for lower laser energy densities and under-predicts it for higher laser energy densities. With increasing pressure, the discrepancy between model and measurements gets larger. Interpretatively spoken, it can be seen that especially for higher laser intensities more fluorescing molecules are measured than can be predicted by the model.

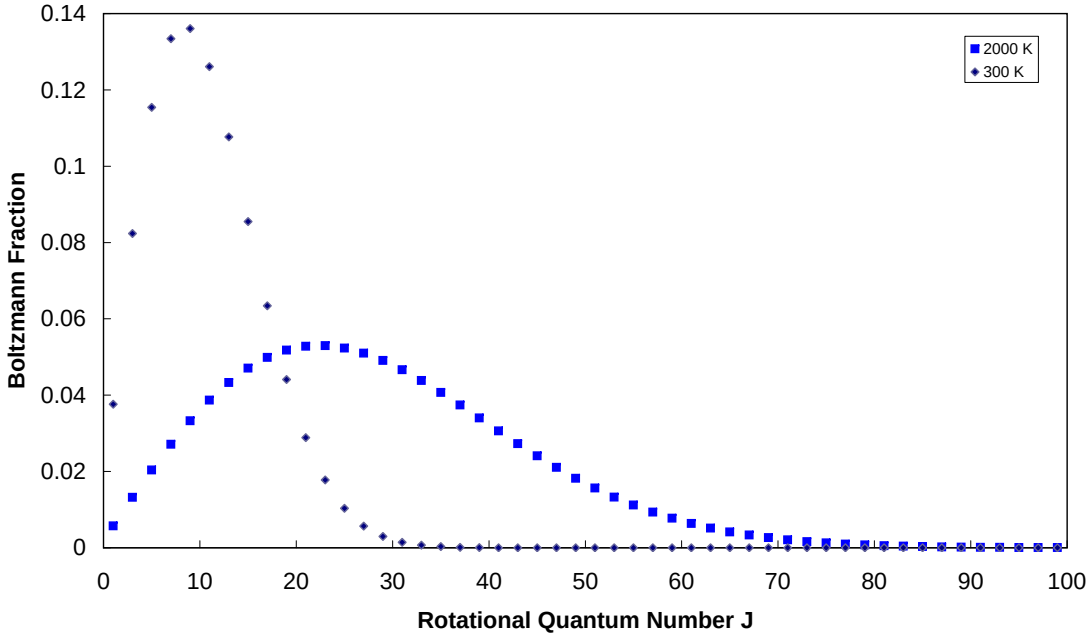

Figure 7.3.: Rotational Boltzmann distribution of O_2, $v'' = 7$ for $T = 2000\,\mathrm{K}$, neglecting the spin components.

In Figure 7.4, I used the RET value found by Nguyen and Paul [29] which is $Q_{RET} = 6 \cdot 10^9\,\mathrm{s^{-1}bar^{-1}}$, as the model predictions do not change significantly if the Q_{RET} constant is taken ten times larger or smaller (see Figure A.7).
A reason for the unsatisfactory fit results could be the simplification of defining a single refill rate constant Q_{RET} in combination with a single pool state that neglects different state-to-state RET rates, resulting in a too quick depletion of the ground state as a whole. To investigate this, a model that resolves RET in more detail is proposed in the next section.

7.2.3. Detailed RET Model

A more detailed description of RET can be achieved by considering rotational state-to-state energy exchange processes. As described in subsection 2.3.1 there are several model approaches to describe RET. For this study, I modeled the state-to-state RET rates with a modified exponential gap (MEG) law as proposed by Koszykowski et al. [35] (Equations 3.9 and 3.10). The model with parameters from Millot et al. [100] (see Table 3.1) has shown good agreement with Raman and CARS [39] measurements for N_2-O_2 and O_2-O_2 collisions. With air as an oxidant, collisions with N_2 happen the most

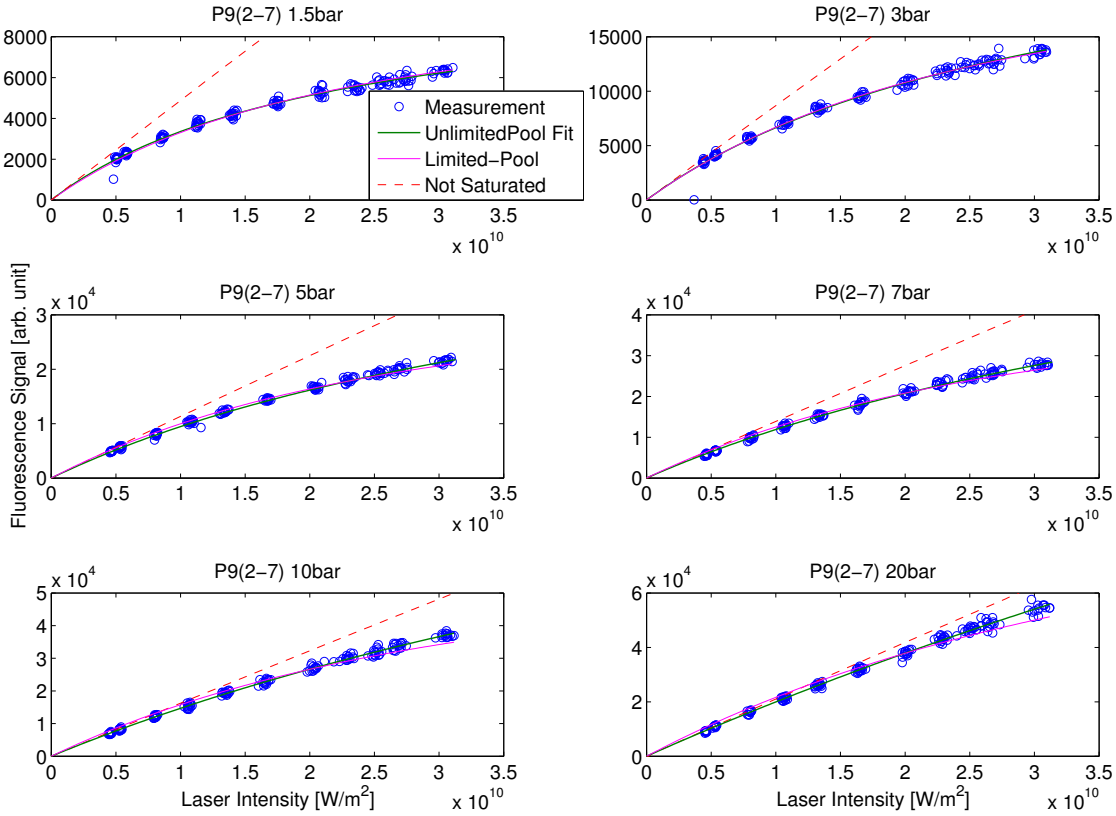

Figure 7.4.: Comparison of three-level model fits with limited pool and unlimited-pool assumptions to saturated O_2 LIF measurements of the P9(2-7) line for different pressures and to the hypothetic unsaturated LIF.

frequently, so the constants can be used for the present study.

Judging from the rotational Boltzmann distribution of the ground state (see Figure 7.3), the inclusion of 50 rotational states each for the ground state and the excited state is sufficient. When comparing the detailed RET model to the measurements, only the fluorescence constant FC is a fit parameter. Figure 7.5 shows model fits to the same measurements as in subsection 7.2.2 and compares them to the limited-pool three-level model fits discussed above. For a better comparison, I calculated the detailed RET model with a fluorescence constant so that both model calculations coincide for the lower energy densities. It can be seen from this plot that the fits from the detailed RET model match the measurements even worse than the results from the limited-pool three-level model. The constants for the MEG law were determined by Millot et al. [100] and used by Seeger et al. [39] quite precisely and experimentally validated for a maximum temperature of 1000 K. To account for uncertainties of the extrapolation to

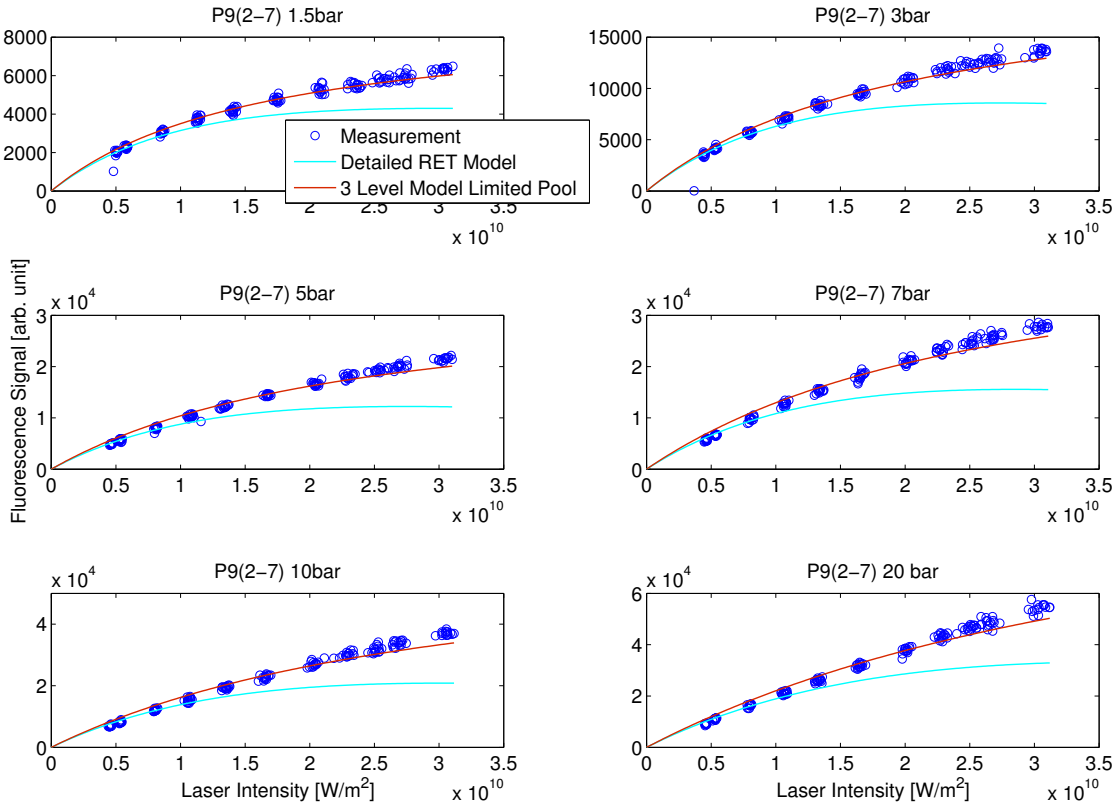

Figure 7.5.: Comparison of the detailed RET model fits and three-level model limited-pool fits to saturated O_2 LIF measurements of the P9(2-7) line for different pressures.

my conditions of about 2000 K, I tested state-to-state rates ten times larger and smaller than proposed by Millot et al. [100]. The results with these state-to-state rates did not change the fits notably, the comparison is shown in Figure A.8.
This observation is known from the three-level model. Also the detailed RET model can not provide enough fluorescing molecules and the RET is not the limiting factor. The description of RET with a more detailed state-to-state rate RET model cannot improve the agreement between calculations and measurements.

7.2.4. Unlimited-Pool State Size

Rothe et al. [30] observed for their three-level model investigations of the OH radical LIF saturation that an unlimited-pool state fits their measurements better. For an unlimited-pool state the solution of the three level model (Equations 3.4 - 3.6) gets quasi-stationary for the investigated experimental conditions of fast excitation and fast Q_{RET} compared

to the laser pulse lenght ($\tau_{exc} = \frac{1}{b_{12}} << 20\,\text{ns}$ and $\tau_{RET} = \frac{1}{Q_{RET}} << 20\,\text{ns}$) Thus, the calculation of the LIF signal F reduces to:

$$F = FC \cdot \frac{1}{\tau} \frac{b_{12} Q_{RET}}{b_{12} + Q_{RET}} \tag{7.1}$$

I also observed a much better agreement of results of the three level model with the measurements, when using a very large pool size, see Figure 7.4. The three-level model with unlimited-pool approximation provides well-defined Q_{RET} values, which are discussed in section 7.3. Thus the three-level model is the only model that can represent the measurements in a meaningful way. A physical rationale for an unlimited-pool approximation yet remains unclear and will be discussed in the next section.

7.2.5. Discussion

So far I have shown three approaches to model saturated O_2 LIF with different results. A surprising finding was that the detailed RET model, which is supposed to describe RET better, provides less good results than the three-level model with limited pool, although the pool size is the same. To understand the different results, I want to compare the refill process of the state which is excited, as described with the two models. Since the models use different parameters, I introduce for the direct comparison of the models the effective refill rate Q_{Refill}, defined as the total amount of molecules supplied by RET divided by the laser pulse length. As an example, I show the temporal evolution of the refill rate, extracted from the detailed RET model during a laser pulse in Figure 7.6. The integral time average Q_{Refill} I use for the comparison is marked as the red-dotted line in Figure 7.6. In Figure 7.8, I show how Q_{Refill} for different models changes with the pressure. For the three-level model with limited pool assumption I show the possible span of Q_{Refill}, I investigated based on the results of Nguyen and Paul [29], as discussed above. It can be seen from this plot that even though the state-to-state RET rates and Q_{RET} for the three-level model with limited-pool increase linearly with pressure, Q_{Refill} quickly levels off due to the limitation of available molecules. The models with limited pool have in common that independently from the value of the RET rates, Q_{Refill} has an upper bound, determined by the total amount of available molecules, which is shown as the red line in Figure 7.8. Thus, the model fits of the detailed RET model do not depend on the choice of the MEG model, all other state-to-state approaches, as explained in section 3.3, would be identically limited. To better understand the curves from Figure 7.8, I calculated the depletion of the rotational populations of the ground state with the detailed RET model. Figure 7.9 shows the initial and final ground state

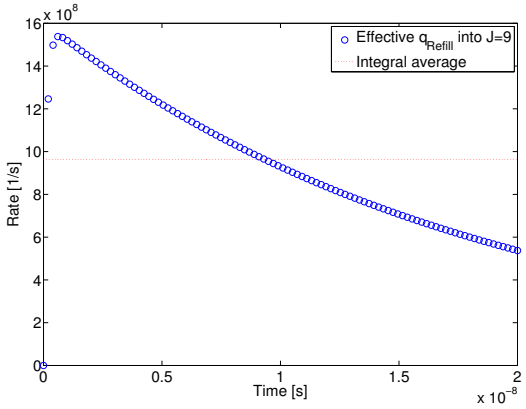

Figure 7.6.: RET rate into $J'' = 9$ at $p = 1.5$ bar, calculated with the detailed RET model for a laser excitation rate of $2.5 \cdot 10^9\ \mathrm{s}^{-1}$ $(3.1 \cdot 10^{10}\ \mathrm{W/m^2}$ for the P9(2-7) transition).

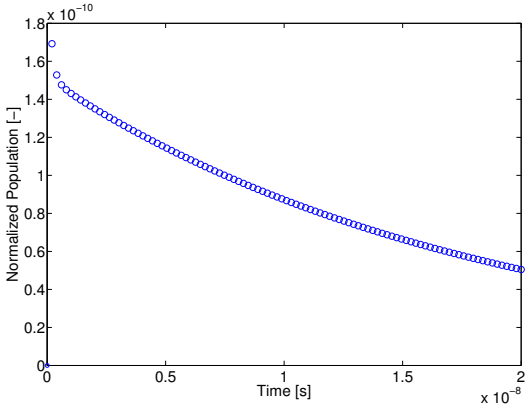

Figure 7.7.: Population of the excited state $J' = 8$ at $p = 1.5$ bar calculated with the detailed RET model, laser excitation rate of $2.5 \cdot 10^9\ \mathrm{s}^{-1}$ $(3.1 \cdot 10^{10}\ \mathrm{W/m^2}$ for the P9(2-7) transition.

populations of a laser pulse for different pressures. From this plot it can be seen that the upper limit of Q_{Refill} is arises from a maximal number of of accessible molecules, which is defined by the combination of laser excitation and thermal equilibration. At 0.5 bar about half of the population gets depleted during the laser excitation. At 5 bar, the depletion increases to about 70 % of the initial total population and does not increase much further at 25 bar. The effect of the depletion of the ground state molecules on the LIF signal can be seen from the population of the excited state. In Figure 7.7 the temporal population evolution of the excited state during the laser pulse is shown. In agreement with the ground state refill (Figure 7.6) the population of the excited state firstly rises quickly and then decreases with increasing pulse duration. Figure 7.10 shows the resulting rotational populations of the excited state at the end of the laser pulse. From this plot it can be seen that RET distributes the molecules in the excited state significantly at higher pressures. We observe such a distribution for higher pressures in the measurements (see subsection 4.3.1) which can be seen as an independent confirmation that we investigate RET rates in a reasonable order of magnitude.

I have added in Figure 7.8 Q_{Refill} of the three-level model with unlimited-pool assumption as the solid green line with the fit results of Q_{RET}. It can be seen from this plot that Q_{Refill} for this model increases more strongly with the pressure and exceeds the values of the other (limited-pool) models ultimately approaching the excitation rate. Therefore, only the model with unlimited pool can represent the observation that saturation

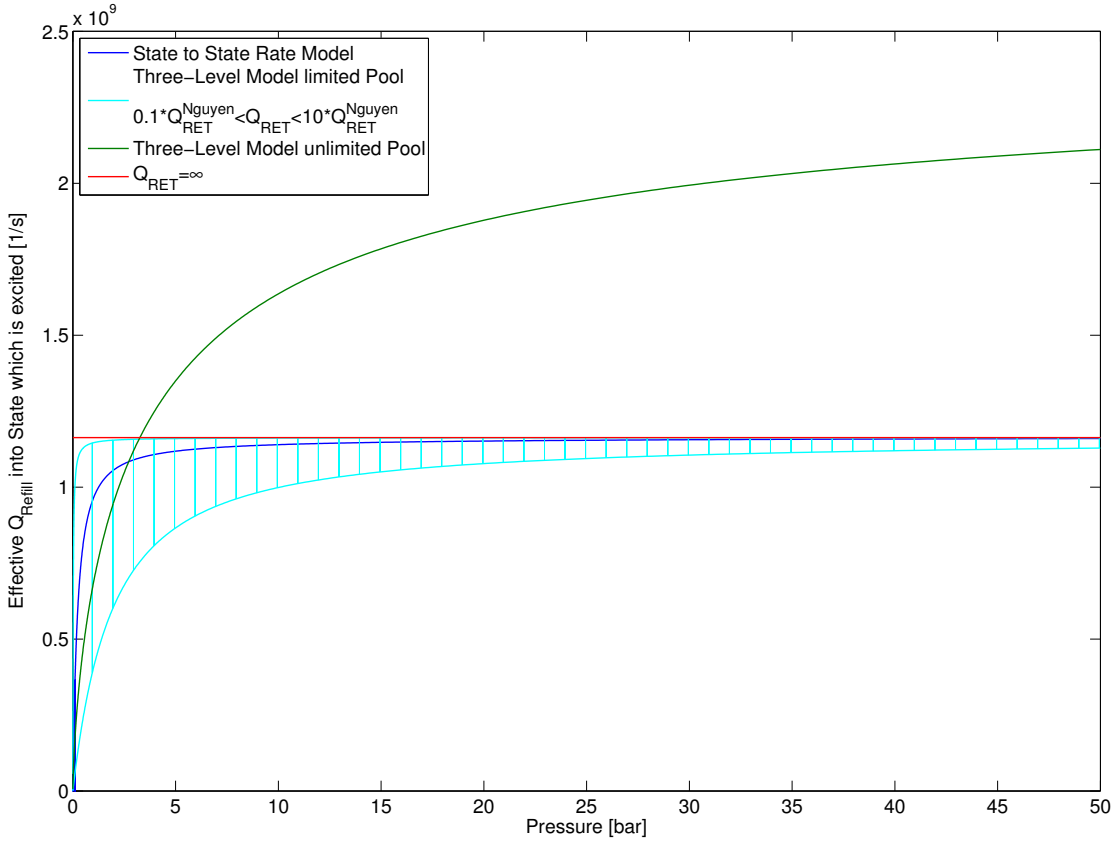

Figure 7.8.: Q_{Refill} compared for different models, calculated with a laser excitation rate of $2.5 \cdot 10^9\ \mathrm{s}^{-1}$ ($3.1 \cdot 10^{10}\ \mathrm{W/m^2}$ for the P9(2-7) transition). For the detailed model, state-to-state rates are calculated with the constants of [100], the limited three-level model is calculated with $Q_{RET}^{Nguyen} = 6 \cdot 10^9\ \mathrm{s}^{-1}$ [29] and the unlimited three level model with the fit results.

decreases with increasing pressure. The limited pool models exhibit the same saturation trends at higher pressures.

One of the possible explanations why a model with an unlimited pool fits the measured data better, is that the rotational pool is filled quickly through another process. Vibrational Energy Transfer (VET, see subsection 2.3.2) can be considered as a refill process. But for the excited state Sick et al. [45] have not observed VET and also theoretical and experimental data from Coletti and Billing [46], Esposito and Capitelli [47] and Huestis [111] indicate that the fastest rates for O_2 - O_2, O_2 - O and H_2O - O_2 VET are about two to three orders of magnitude smaller than RET rates. Even considering larger populations of the neighboring vibrational levels, VET is too small to fill the rotational pool.

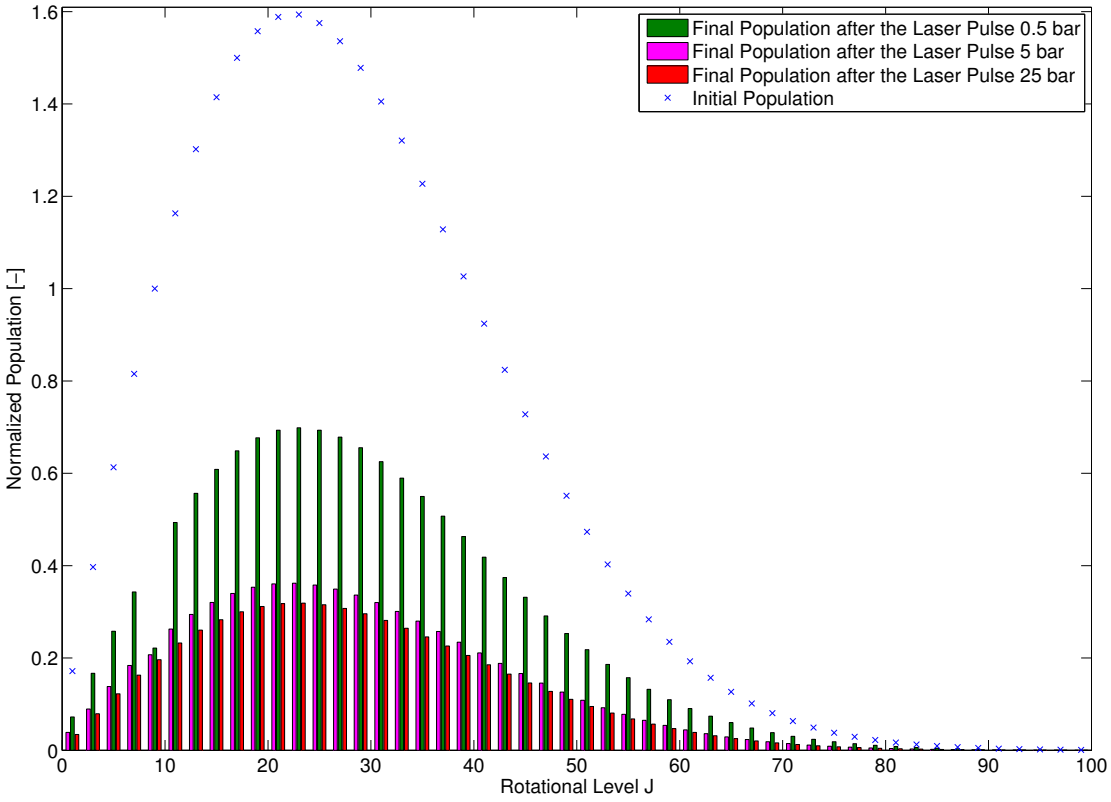

Figure 7.9.: Ground state populations before and after the laser pulse for different pressures, calculated with the detailed RET model for a laser excitation rate of $2.5 \cdot 10^9\ \mathrm{s}^{-1}$ ($3.1 \cdot 10^{10}\ \mathrm{W/m^2}$ for the P9(2-7) transition).

Recombination of O atoms (which result from the photodissociation) could also be considered. As mentioned by Rothe et al. [30] for OH, several consequent collisions are needed for the recombination. Besides that, the recombined O_2 molecule will probably end up in a different vibrational state. Therefore, refill from the recombination of O atoms can also not be large.

Other processes (e.g. resonance-enhanced Raman scattering or electronic energy transfer) have to the best of my knowledge not been reported to be able to account for such a refill.

Summarizing the discussion above, I can say the following: the three-level model with unlimited-pool describes the measured data well, and significantly better than limited pool models and therefore I will use it for the further investigation. The reason, why an unlimited pool should be justified remains unclear. In the three level model there are only two variable parameters in the three-level model, which have an influence on the

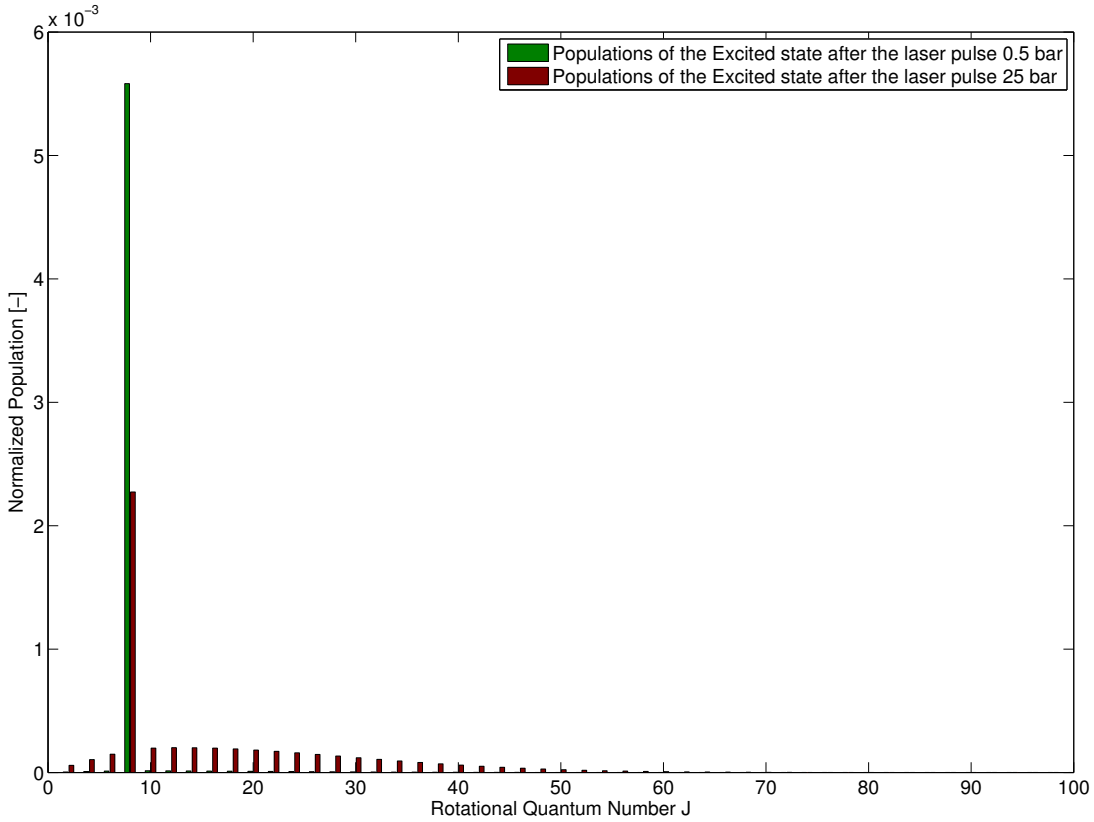

Figure 7.10.: Excited state populations after the laser pulse compared for 0.5 bar and 25 bar, calculated with the detailed RET model for a laser excitation rate of $2.5 \cdot 10^9\ \mathrm{s}^{-1}$ ($3.1 \cdot 10^{10}\ \mathrm{W/m^2}$ for the P9(2-7) transition).

result, the excitation rate and the size of the pool state. Should the excitation rate be significantly smaller or the pool larger the measurements could also be described by a limited pool model. The calculation of the excitation rate is explained in subsection 4.3.3 and is comparable to values reported by Nguyen and Paul [29] or Rothe et al. [30]. To determine the rotational pool from the Boltzmann distribution of the populations is also often reported and applied, e.g Rothe et al. [65]. A fast enough refill process can not be identified and systematic experimental errors are not seen to introduce the observed trends.

7.3. Quantitative Analysis of Q_{RET}

Following the results of the previous section, the quantitative analysis of the O_2 saturation is based on the comparison between the three-level model with unlimited-pool

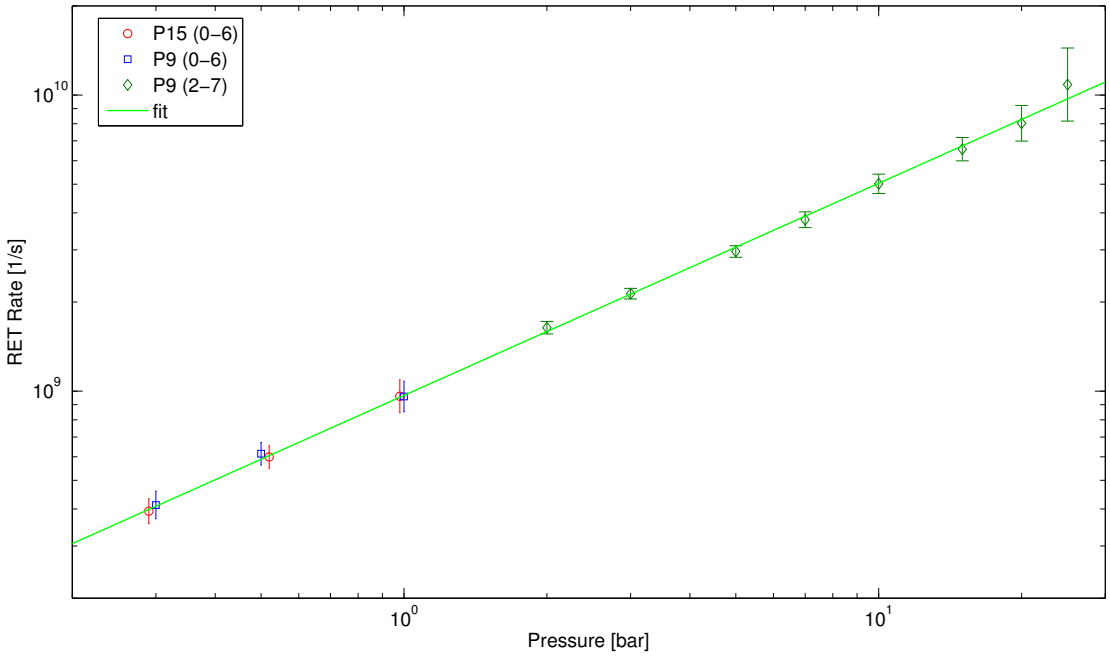

Figure 7.11.: Q_{RET} Fitted with the three-level model with unlimited pool to saturated LIF measurements in a CH_4/air Flame with $\lambda = 1.2$ for different pressures and excitation lines. Error Bars indicate the 95 % confidence intervals of the fit.

assumption and measurements. As I have to assume a RET pool which is much larger than it should be according to the Boltzmann distribution, the parameter Q_{RET} does not necessarily include just RET. Therefore I will call Q_{RET} the effective RET rate constant for the remainder of this work. Figure 7.11 shows the resulting Q_{RET} for model fits to measurements at different pressures and for different excitation lines. I fitted Q_{RET} for the P9(2-7) line in the range of 1.5 bar - 25 bar and for the (0-6) band transitions below 1 bar.

From this double logarithmic plot can be seen that the dependence of Q_{RET} on the pressure follows a power law according to Equation 7.2. With the P9(0-6) and the P9(2-7) line, I investigated the same rotational transitions in two vibronic bands, while with the P9(0-6) and the P15(0-6) lines, I could investigate two identical vibronic transitions with different rotational levels. Within the accuracy of the measurements, Q_{RET} for the three different rotational and vibrational transitions can be described with the same set of parameters a and b (given in Table 7.2).

A surprising result of this investigation is that the effective RET rate Q_{RET} does not depend linearly on the pressure as it is expected for the RET process. This will be

discussed in detail in section 7.4.

$$Q_{RET} = a \cdot \left(\frac{p}{p_0}\right)^b \quad \text{with } p_0 = 1\,\text{bar} \tag{7.2}$$

Variation of the Flame Gas

RET and other collisional processes depend on the gas composition. To study how the observed Q_{RET} depends on the gas composition, I investigated different flames in which the ratio of CO_2/H_2O in the exhaust was varied by changing the fuel and N_2 in air was substituted by Ar. N_2 is the main collisional partner with air as an oxidant, and I expect to estimate its influence on Q_{RET} if I replace it by Ar. CO_2 and H_2O are both efficient RET partners, so I chose fuels with different C to H ratios to estimate their influence on Q_{RET}. To exclude the temperature dependence, I calculated the compositions with the GRI 3.0 mechanism [18] and an equilibrium code of the CHEMKIN II package [19] to give the same adiabatic flame temperature. The results of the calculations are shown in Figure 7.12. It can be seen that the largest theoretical variation of the temperature is roughly 6 K which can be regarded to be negligible with respect to the adiabatic flame temperature of about 2000 K. The lower heat capacity of Ar compared to N_2 causes

Name	Fuel	Dt[1]	λ	$\chi(CO_2)$	$\chi(H_2O)$	χ(Dt[1])	$\chi(O_2)$	T_{ad}(1bar)
CH_4 /air	CH_4	N_2	1.2	8.0 %	16.1 %	72.7 %	3.2 %	2042 K
CH_4/O_2+Ar	CH_4	Ar	1.2	5.6 %	11.2 %	81.0 %	2.2 %	2044 K
C_2H_4/O_2+N_2	C_2H_4	N_2	1.2	9.7 %	9.7 %	77.8 %	2.9 %	2045 K
C_2H_4/air	C_2H_4	N_2	1.37	9.7 %	9.7 %	75.2 %	5.4 %	2046 K
C_2H_4/O_2+Ar	C_2H_4	Ar	1.2	6.6 %	6.6 %	84.8 %	2.0 %	2043 K

Table 7.1.: Exhaust gas composition and mole fraction of major species of the investigated flames.

a higher mole fraction of Ar for a flame with the same adiabatic flame temperature. Thus, it is not possible to completely separate the effects of collision partners. Table 7.1 shows an overview of the exhaust gas composition, where LIF is measured. Figure 7.13 shows the pressure dependence of Q_{RET} for the flames described in Table 7.1, measured for the P9(2-7) line. The parameters a and b to describe the power law dependence of Q_{RET} on the pressure for the different flames are listed in Table 7.2. It can be seen from Figure 7.13 that for different flame gas compositions the power-law dependence

[1] Diluent

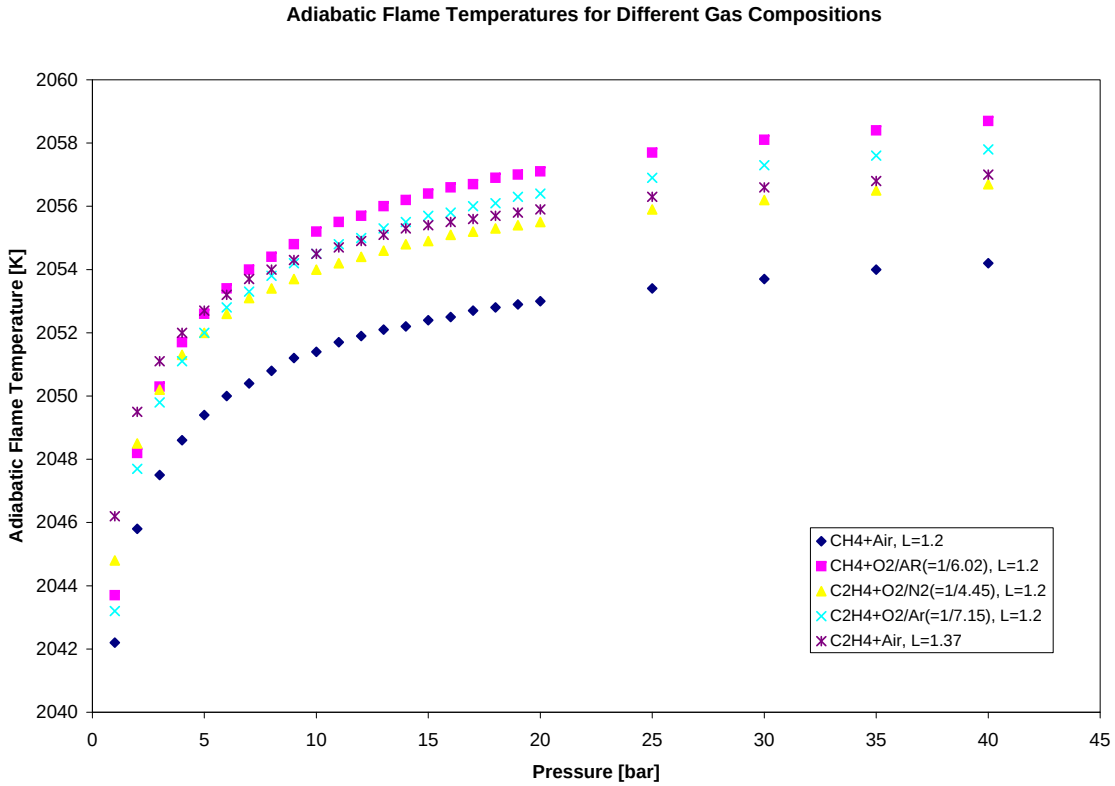

Figure 7.12.: Adiabatic flame temperatures calculated with the GRI 3.0 mechanism [18] and an equilibrium code of the CHEMKIN II package for different flame gas compositions.

of effective RET rate Q_{RET} on the pressure changes. The differences relate to both parameters of the power law.

7.4. Discussion of Q_{RET} Rate Results

Other authors have reported RET rates measured in CH_4/air flames at atmospheric pressure. Rothe et al. [30] have found a RET rate for OH to be $1.8 \cdot 10^9\,\mathrm{s}^{-1}$, which agrees well with my measurements. Nguyen and Paul [29] have found RET for O_2 for an atmospheric CH_4/air with an equivalence ratio of $\phi = 0.7$ to be $(6 \pm 2)10^9\,\mathrm{s}^{-1}$. This value is considerably larger compared to my findings of $Q_{RET} = 1 \cdot 10^9\,\mathrm{s}^{-1}$ at 1 bar and needs therefore to be discussed in more detail. They investigated two different strengths of laser intensity at 1 bar and compared them to a five-level model with limited-pool. I have shown in Figure 7.4 that at atmospheric conditions, a limited-pool model can

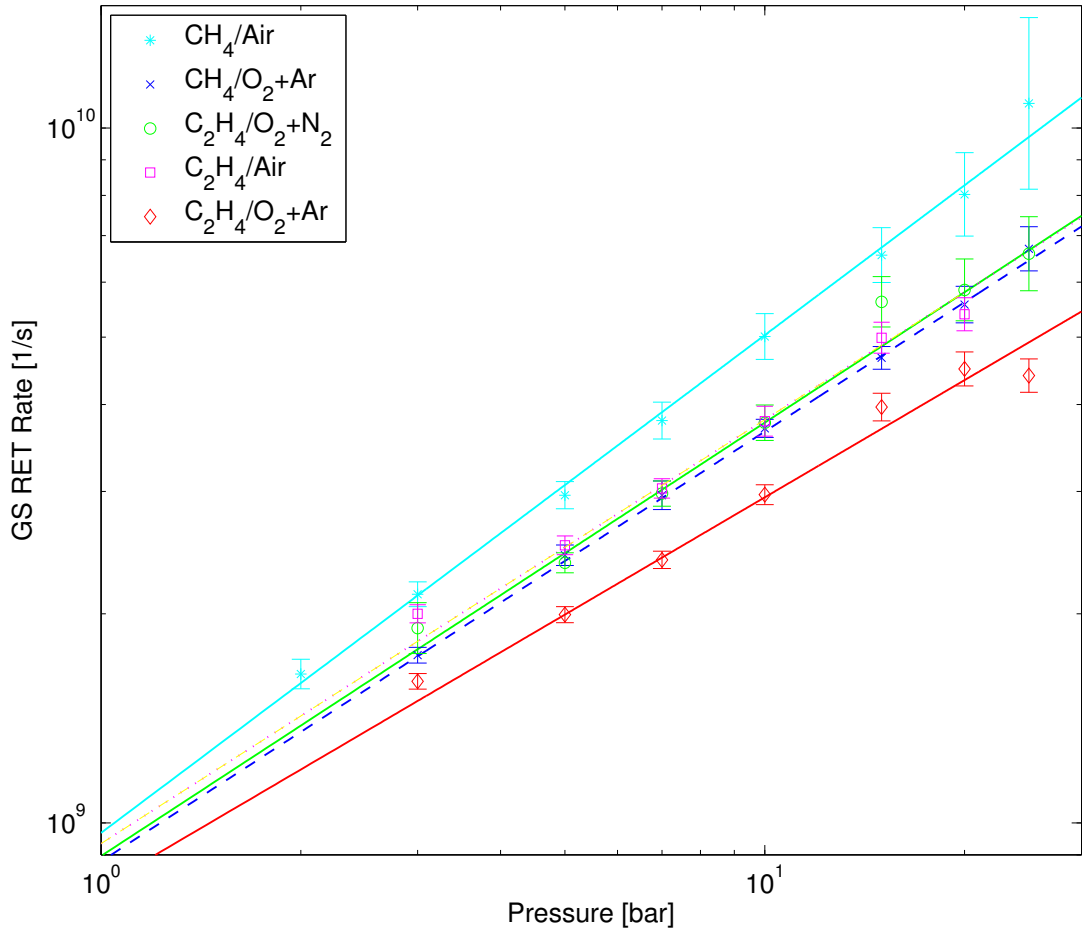

Figure 7.13.: Q_{RET} fitted with the three-level model with unlimited pool to saturated LIF measurements of the P9(2-7) line for different pressures and flame gas compositions (listed in Table 7.1). Error bars indicate the 95 % confidence interval of the fit.

provide reasonable fits with their value of Q_{RET}. On the other hand, I have also shown in section 7.2 that increasing their value of Q_{RET} by a factor of ten does not change the fit result. (At 1 bar the three-level model with limited pool can be fitted to the measurements within a wide range of Q_{RET}.) Decker [13] has found $Q_{RET} \approx (2.4 \pm 1) \cdot 10^9\ \mathrm{s}^{-1}$ but he used Q_{RET} to depend linearly on the pressure and overestimated RET compared to his measurements above 10 bar.

One of the surprising findings of this work is that the effective RET rate Q_{RET} does not depend linearly on the pressure. Collision rates are proportional to the pressure, as the gas density increases. State-to-state RET rates are reported e.g in Seeger et al. [39] to be proportional to the pressure over a large pressure range up to 100 bar. Compared to

Flame	$a[10^9\,\mathrm{s}^{-1}]$	b
CH_4/air	0.97 ±0.04	0.72 ±0.03
CH_4/O_2+Ar	0.91 ±0.02	0.61 ±0.01
C_2H_4/O_2+N_2	0.90 ±0.03	0.62 ±0.02
C_2H_4/air	0.93 ±0.02	0.61 ±0.02
C_2H_4/O_2+Ar	0.81 ±0.03	0.56 ±0.02

Table 7.2.: Power law parameters a and b for $Q_{RET}(p)$, a and b are the result of a least-squares fit procedure weighted with the error bars of Q_{RET}.

them, the experimental conditions are different in my investigations, as the strong excitation depletes the state which is excited significantly. I have shown in section 7.2 that even though the underlying state-to-state RET rates increase proportional to the pressure, the measurements cannot be matched with limited-pool models. The consequent introduction of an unlimited pool results in the above mentioned power-law dependence of Q_{RET} on the pressure. This implies that the typically used formalism of collisional cross sections cannot be used to describe Q_{RET}. This also implies that a linear analysis of the major exhaust gas species and their contribution to Q_{RET} is not possible due to the non-linearity of the Q_{RET}.

What can be seen, however, from the comparison of the pairs of flame conditions CH_4/air and C_2H_4/air as well as CH_4/O_2+Ar and C_2H_4/O_2+Ar is that the fraction of H_2O goes down, whereas the other major exhaust gas species fractions stay constant or increase. In both cases Q_{RET} decreases significantly, which indicates that H_2O is very efficient concerning the Q_{RET} process.

Q_{RET} for the flames C_2H_4/O_2 and N_2 and C_2H_4/air is within the accuracy of the measurement identical. This is expected as the exhaust gas composition is nearly identical, but it shows that the results are reproducible.

I investigated Q_{RET} at 2000 K. In technical applications, CH_4/air combustion with different fuel to air ratios can span a temperature range of $\approx 1500\,\mathrm{K} - 2200\,\mathrm{K}$. Concerning applications like two-line O_2 thermometry it is important to know the temperature dependence of Q_{RET}. From the state-to-state rate model, I know that the single state-to-state rate depends on the temperature as $(T/295\,\mathrm{K})^N$, with $N = 1.31$ for O_2 - O_2 and O_2 - N_2 collisions. On the other hand I have shown that the increase of the state-to-state rates with the pressure does not affect Q_{RET} in the same way. This could be translated to the dependence of Q_{RET} on the temperature indicating that Q_{RET} will not change significantly with the temperature.

7.5. Prediction of O_2 Spectra

The result from the previous section, that Q_{RET} is the same for the investigated rovibronic transitions P15(0-6), P9(0-6) and P9(2-7) can be generalized, assuming that Q_{RET} is the same for all transitions within the KrF excitation range. This allows to predict the effect of Q_{RET} on the LIF signal of these transitions and hence, predictions for saturated O_2 spectra are possible. For this purpose, I have developed a simulation code to model the O_2 LIF signal using the three-level model with unlimited-pool assumption (see section 3.4). To validate the predictions of the code developed here, I simulated an

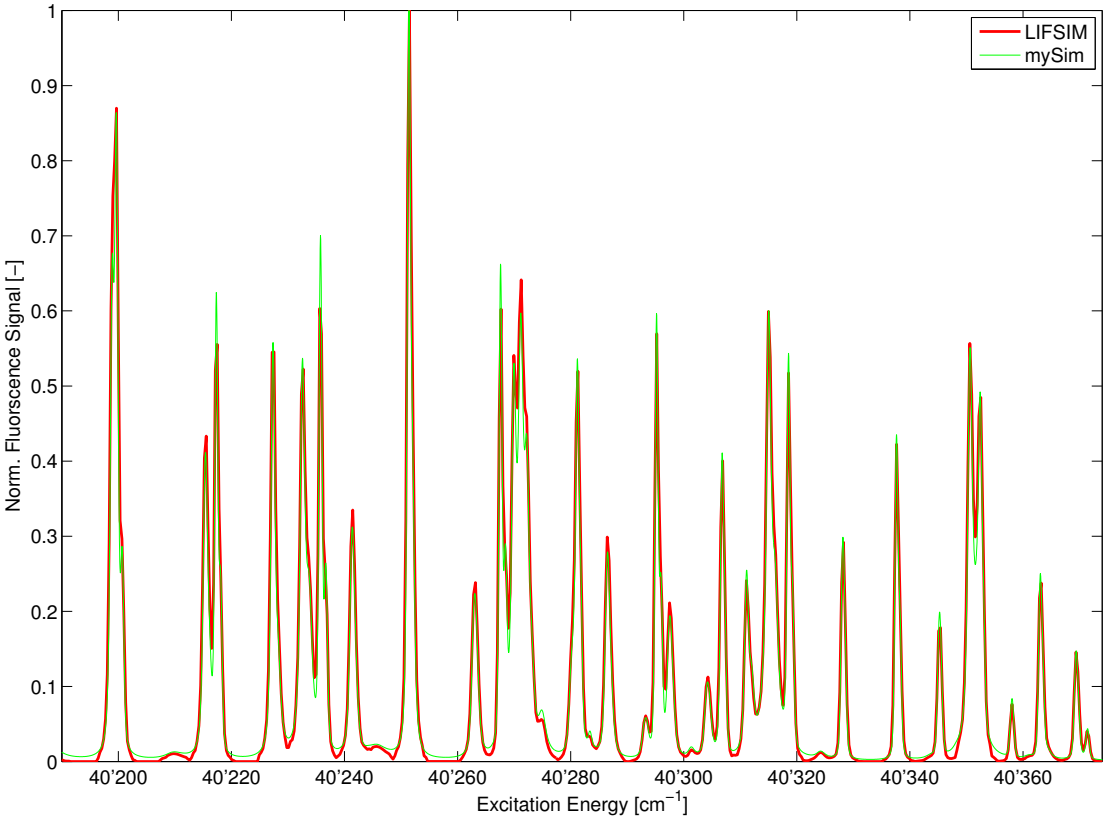

Figure 7.14.: Simulation of an unsaturated O_2 spectrum with the developed code compared to a LIFSIM calculation [92], simulation parameters are listed in Table 7.3.

O_2 LIF spectrum for a low laser intensity, when saturation does not occur. Figure 7.14 compares this simulation to a LIFSIM spectrum with identical input parameters (which are listed in Table 7.3). For the comparison, the LIF signal was normalized with the maximum signal in each spectrum. From this plot it can be seen that the two spectra are nearly identical, indicating the validity of the code developed. One possible explanation

for the slight differences can be found in the calculation of the excitation rate described in subsection 4.3.3. I use experimental data for the collisional broadening factor while Bessler et al. [92] do not explain how they account for pressure broadening.

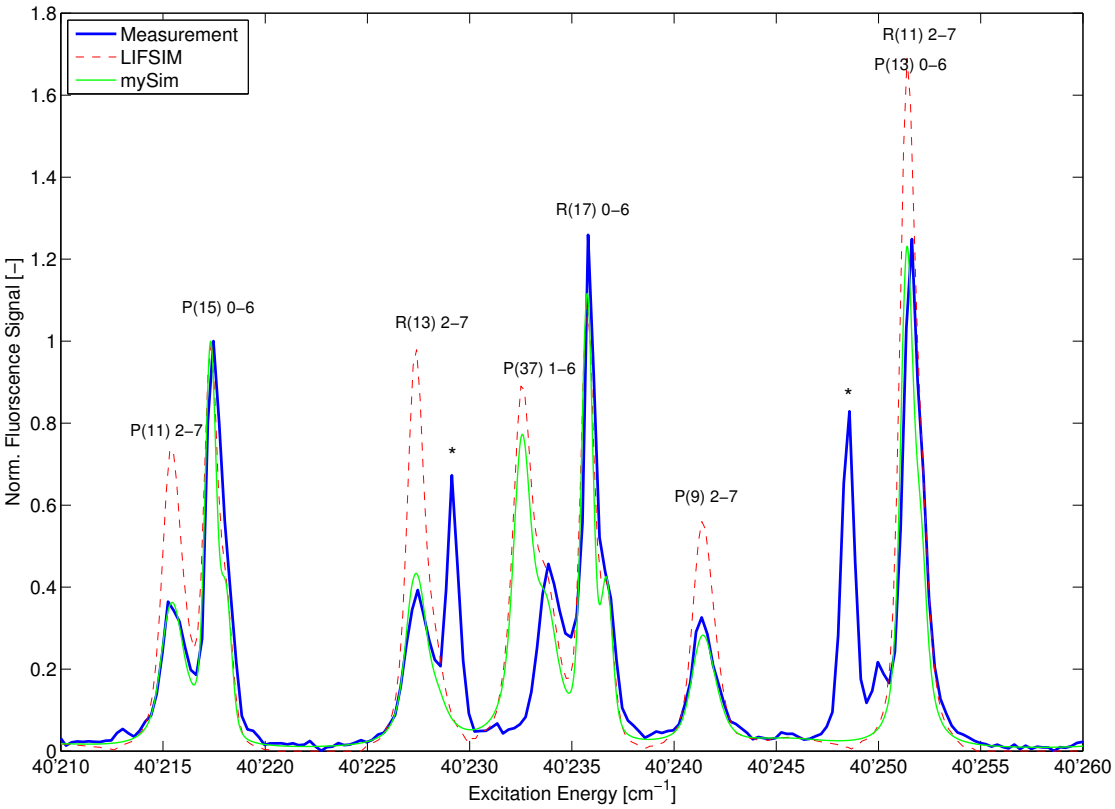

Figure 7.15.: Simulation of a saturated O_2 spectrum with the developed code compared to a measurement and a LIFSIM calculation [92], experimental conditions and simulation parameters are listed in Table 7.3.

After showing that my code is validated, the next step is to compare my simulations to measurements of saturated O_2 LIF and see, whether my code can provide better results as LIFSIM. In Figure 7.15 I show a comparison of O_2 LIF spectra between my simulation and a measurement with a high laser intensity so that the (2-7) transitions are saturated. The conditions of the measurement and the parameters of the simulation are given in Table 7.3. A LIFSIM calculation, which does not take saturation into account is also added in this plot. For the comparison, I normalized the LIF signals with the fluorescence of the P15(0-6) transition. From Figure 7.15 can be seen that the calculation including the saturation mechanism can represent the measurement significantly better than LIFSIM. Compared to the unsaturated case, represented by LIFSIM, the relative intensity of the (2-7) lines is decreased, which is correctly reproduced with my

code. The combined R11(2-7)/P13(0-6) line, which is useful for two line thermometry is also correctly represented by my simulation. In the plot, I marked two peaks of the measurement with an asterisk (*). These are OH transitions belonging to the A-X(3-0) band. Both simulation codes do not take care of other species than O_2, therefore these peaks are not included in the simulation. There is disagreement for the P37(1-6) line for both simulations with the measurement. The original source of the line position and transition parameters [10, 11] indicate larger uncertainties for these data for rotational quantum numbers $J > 30$. Therefore the small error in the position and the intensity of the P37(1-6) line is not unexpected.
Summarizing the results above, I can conclude that my simulation of O_2 spectra with a three-level model, including the results from the previous section concerning saturation of O_2 LIF, can improve the prediction of O_2 spectra significantly. These results can be helpful when it comes to measurements, where the different LIF intensities are used to conclude physical properties e.g. like concentration measurements or two-line thermometry.

Flame	CH_4/air, $\lambda = 1.2$	
Emission Bandwidth	285 nm − 290 nm	
Laser FWHM	$0.6\,\mathrm{cm}^{-1}$	
Temperatur	2000 K	
Pressure	1 bar	
Laser Intensity	$\underbrace{1.0 \cdot 10^7\,\mathrm{W/m^2}}_{\text{unsaturated}}$	$\underbrace{1.3 \cdot 10^{10}\,\mathrm{W/m^2}}_{\text{saturated}}$
Q_{RET}	$0.97 \cdot 10^9\,\mathrm{s}^{-1}$	

Table 7.3.: Simulation parameters for unsaturated and saturated O_2 Spectra.

7.6. Quenching Analysis with the Three-Level Model

In chapter 6 I have estimated an upper limit for the quenching cross section of the excited $v' = 0, 2$ B-states of O_2 from a comparison of measurements of the fluorescence from different ro-vibronic transitions with the same J. The results of the quantitative saturation analysis in the previous section show that the measurements in chapter 6 with the lower laser intensity (about $0.6 \cdot 10^{10}$ W/m^2), were slightly saturated at least for the (2-7) band transitions at 1.5 bar and 3 bar. Therefore the decrease of the fluorescence ratios with the pressure depends even less on quenching and the upper limit of the quenching cross section is even lower than the estimated value of $\sigma_Q \approx 10$ Å^2 (see chapter 6).

The investigations with the three-level model allow for an independent analysis of the quenching cross section. As explained in section 3.2, in the construction of the three-level model, I did not consider quenching as a loss term. If quenching occurs, it will only depend on the pressure and not on the laser intensity. Therefore, the fit parameter called the fluorescence constant FC will adjust accordingly and include the effects of quenching. In the ideal case, if no quenching is present, FC should grow linearly with the pressure as the gas density increases. A deviation from the linear dependence may indicate quenching. Figure 7.16 shows the extraction of the fluorescence constant for the different flame gas compositions investigated in section 7.3. In these measurements the P9(2-7) transition was investigated at different pressures. Several observations can be made in this figure: FC does not linearly depend on the pressure, I can represent this dependence with a power law according to Equation 7.2. The constants resulting from a least-squares fit are listed in Table 7.4. The curves vary especially in the b parameter. The error bars, indicating the 95 % confidence interval are smaller, compared to the ones of the Q_{RET} fits.

7.6.1. Discussion

The deviation from a linear dependence of FC on the pressure can be calculated for the CH_4/air flame at $p = 10$ bar as $\Delta FC = ((\frac{p}{p_0})^1 - (\frac{p}{p_0})^{0.68})/(\frac{p}{p_0})^1 \approx 50$ % (with $p_0 = 1$ bar). Assuming that the entire loss of signal can be accounted to quenching, I can calculate an upper bound of the quenching cross section by comparing the fluorescence quantum yield (defined as $A/(A + P + Q)$) with $Q(p) = \bar{Q} \cdot p$ at both pressures. The problem is then solved for the quenching rate constant $\bar{Q}$ that provides half the signal at 10 bar

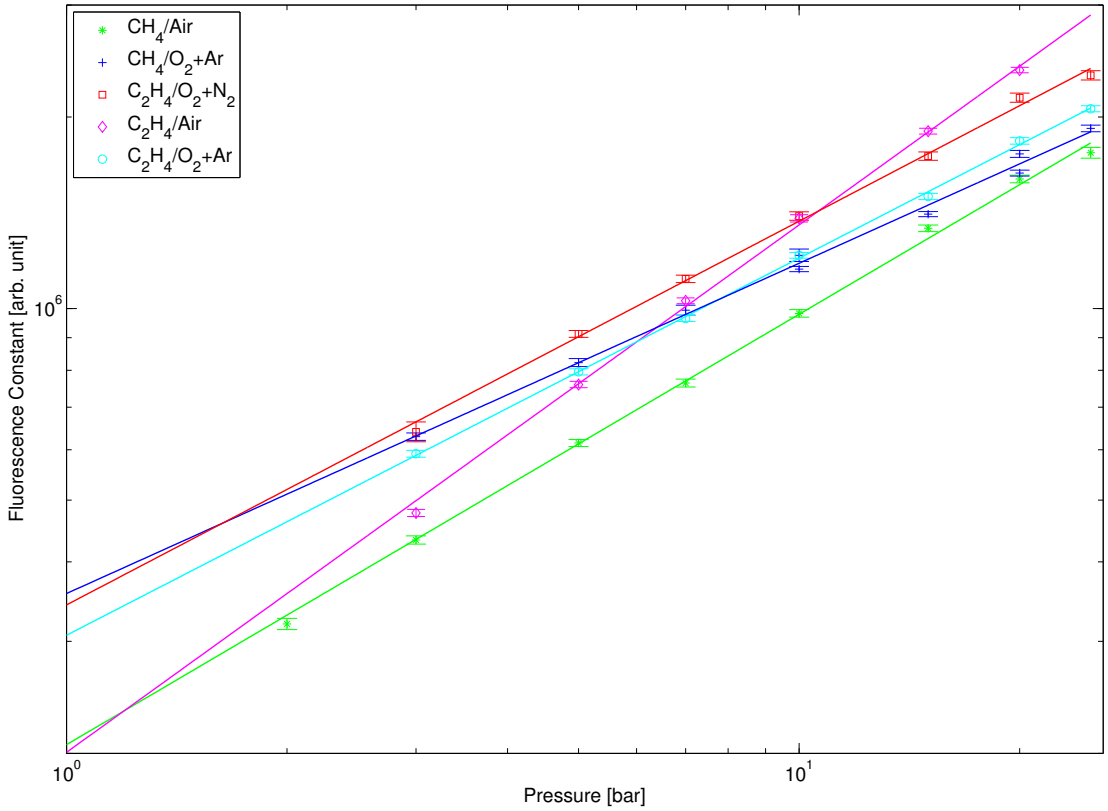

Figure 7.16.: Fluorescence constants of the corresponding Q_{RET} fits from Figure 7.13.

compared to 1 bar as shown in Equation 7.3.

$$\frac{\varphi(10\,\text{bar})}{\varphi(1\,\text{bar})} = 0.5 = \frac{A(A+P+Q(1\,\text{bar}))}{A(A+P+Q(10\,\text{bar}))} \tag{7.3}$$

This equation results in an upper bound for the quenching rate constant $Q(1\,\text{bar}) = 1/8P$, and yields a quenching cross section of $\sigma_Q < 180\,\text{Å}^2$. This value is considerably larger than the value found from the NMF investigation ($\sigma_Q < 10\,\text{Å}^2$). Thus, the assumption that the entire deviation from the linear case can be used to conclude an upper bound for quenching is not practical. There are other reasons for a weaker signal, e.g absorption of the emitted light which increases with increasing pressure can also account for a loss in signal.

Concerning the shape of the curves, I cannot explain, why $FC(p)$ should follow a power law. What can be seen from the C_2H_4 curves is a correlation of the O_2 mole fraction in the exhaust and b, which results that for the C_2H_4/air curve b is considerably larger than

for the other C_2H_4 flames. When comparing the two FC curves of the CH_4 flames, it is reasonable that FC is larger for the Ar flame, as Ar is supposed to be a bad quenching partner. But why the curves approach each other around 25 bar remains unclear. This can be seen as another reason, why the quenching cannot account for the differences of the curves.
Summarizing, I can conclude that an upper bound of the quenching cross section of $\sigma_Q < 180\,\text{Å}^2$ can be estimated with the three-level model fit approach, but the approach with the NMF method is more appropriate.

Flame	$a[10^6$ arb. unit]	b
CH_4/air	0.21 ±0.02	0.68 ±0.02
CH_4/O_2+Ar	0.36 ±0.02	0.52 ±0.01
C_2H_4/O_2+N_2	0.34 ±0.03	0.60 ±0.02
C_2H_4/air	0.20 ±0.03	0.83 ±0.02
C_2H_4/O_2+Ar	0.31 ±0.02	0.59 ±0.02

Table 7.4.: Power law parameters for the pressure dependence of FC.

8. Conclusion and Outlook

8.1. Conclusion

In this work, I have addressed and investigated several issues concerning O_2 LIF in combustion-related environments.

Planar O_2 LIF in Rich Flames

I have shown that planar O_2 LIF can be used to locate flame fronts in rich syngas combustion. The accuracy is experimentally found to be comparable with traditionally applied OH LIF. This method extends the capabilities of flame front detection in combustion environments where traditional methods as OH or CH_2O LIF fail. The investigated fuel compositions are chosen to resemble the result of pre-combustion carbon capture techniques and are thus expected to become more and more important in the future. Results gained with planar O_2 LIF flame front detection have been used to verify combustion chemistry mechanisms of Schultze et al. [110].
Due to the low fluorescence signal from the excited O_2, which arises from the combination of a low fluorescence quantum yield of the predissociative O_2 excited states, the rather low UV laser energy and the strong temperature dependence of the O_2 LIF signal, this method is restricted to stationary flames. By the definition of the flame front with vanishing of the O_2 LIF signal, this method is also restricted to fuel-rich combustion.

Quenching Analysis of Excited O_2 with Non-Negative Matrix Factorization

In this work, I have successfully applied non-negative matrix factorization to decompose double-resolved emission/excitation spectra. I showed that this decomposition can be used to disentangle the contribution of different species of the spectra, O_2 and OH in this case. I also showed that with respect to O_2 contributions to the spectra, different rovibronic transitions could be separated. From this decomposition, I was able to conclude an upper bound for the O_2 $B^3\Sigma_u^-$ state quenching cross section at $10\,\text{Å}^2$. This result is significantly lower than previously reported values. I could show that the previously

reported analysis of the quenching cross section was affected by the saturation of O_2 LIF.

Saturation of O_2 LIF

I have quantitatively addressed the pressure dependence of saturation of O_2 LIF in flames, when using high-power excimer lasers. For this purpose, I have prepared an experimental setup and a corresponding data acquisition routine that allow for accurate measurements of saturated O_2 LIF. The key point of these measurements is to precisely measure and vary the laser intensity simultaneously to recording the LIF signal. I showed that the saturation of O_2 LIF can be represented with a relatively simple three-level model and discuss its validity and applicability by a comparison to other models. I could show that the saturation arises from the competition of the depletion of the ground state by laser excitation and an effective Q_{RET} refilling it. With the model I could show that within the precision of the measurements, Q_{RET} does not depend on the vibrational or rotational state but varies with the pressure and for different flame gas compositions. The dependence of Q_{RET} on the pressure is not linear, as one could expect from a collisional process, but can be described with a power law.
To integrate all these results, I have developed a simulation code, with which the saturation of O_2 LIF can be predicted, based on the known spectral properties of the O_2 B-X transitions and additionally the knowledge of the laser intensity and Q_{RET}. The code is validated by a comparison of non-saturated spectra with state-of-the-art LIFSIM [92] simulations (which can not represent saturation). The comparison of my simulations to measurements including saturation exhibit a significant improvement over LIFSIM [92] simulations of O_2.

Quenching Analysis of Excited O_2 with the three-level model

I also used a fit parameter of the three-level model to estimate an upper bound of fluorescence quenching cross section of excited O_2. With this approach I was able to estimate an upper bound at 180 $Å^2$ which is much larger than the one from the NMF analysis. But the assumptions made for this approach are more affected by experimental variations and thus the NMF approach is the more appropriate way to estimate quenching.

8.2. Outlook

The present work has led to new questions which should be addressed in the future.

Planar O_2 LIF in Rich Flames

The detection of flame fronts with O_2 LIF works well in stationary rich flames. A detailed analysis and optimization of the individual LIF setup components might reduce the number of laser pulses the LIF signal needs to be integrated. It might also be interesting to know, whether and under which combustion conditions in the catalytic burner a high power KrF excimer laser would be useful, which allows to excite the ground-state vibrational levels $v'' = 6$ and $v'' = 7$.
The unidentified species, which was observed in the catalytic reactor can be investigated in more detail especially with regard to its emission spectrum, to eventually identify it. It would be worth investigating whether the species can have a useful application in combustion diagnostics.

Non-Negative Matrix Factorization

For the non-negative matrix factorization a method of automated identification of the spectral signature recognition would be helpful. This would allow on the one hand side to better find the optimal number of base vectors in which the spectrum should be decomposed. On the other hand it would allow to improve the NMF results as the decomposition could be executed multiple times to allow for statistics and also to filter out adequately spurious spectral signatures.

Saturated O_2 LIF

I showed that the three-level model with unlimited pool describes saturated O_2 LIF best. A physical justification of the unlimited pool remains still open. To improve the fundamental understanding of the involved processes, this issue should be investigated in more detail. That would probably require different experimental setups and investigation methods as well as sophisticated modeling ideas. In hand with this, a more detailed investigation on the non-linear dependence of Q_{RET} on the pressure is suggested.
For the more practical aspects with respect to application, the temperature dependence of Q_{RET} should be investigated to extend the capabilities of the simulation code also to this parameter. With this dependence known, the accuracy of saturated O_2 predictions with respect to two-line thermometry purposes should be investigated. It would be also helpful to investigate further fuels, to have a table of commonly used fuels and their

corresponding effective Q_{RET} values.

Quenching Rate Analysis

I have shown that the different characteristics of the saturation of the ro-vibronic transitions have an influence on the quenching analysis where the predissociation times are used as an internal clock. As the laser intensity needed to avoid saturation is too low to yield a sufficient signal especially at pressures below 5 bar, the simulation code (presuming the above mentioned improvements) can be used to simulate these spectra and the NMF method can be used to investigate the integrated fluorescence with regard to quenching.

A. Appendix

A.1. Spectroscopic Data

		Excitation Energy [cm^{-1}]	Predissociation Line width [cm^{-1}]	v”	v’	J”	J’
P9(2-7)	F1	40241.4766	0.4255	7	2	9	8
	F2	40241.1641	0.4635	7	2	9	8
	F3	40241.9609	0.6488	7	2	9	8
P9(0-6)	F1	40306.8125	0.1113	6	0	9	8
	F2	40306.6719	0.1756	6	0	9	8
	F3	40307.2773	0.1578	6	0	9	8
P15(0-6)	F1	40217.3281	0.1049	6	0	15	14
	F2	40217.3281	0.1871	6	0	15	14
	F3	40218.0781	0.1743	6	0	15	14

Table A.1.: Properties of the O_2 transitions relevant for the analysis in chapter 7, data is taken from LIFSIM [92].

		Excitation Energy [cm^{-1}]	Predissociation Line width [cm^{-1}]	v”	v’	J”	J’
P9(2-7)	F1	40241.4766	0.4255	7	2	9	8
	F2	40241.1641	0.4635	7	2	9	8
	F3	40241.9609	0.6488	7	2	9	8
P9(0-6)	F1	40306.8125	0.1113	6	0	9	8
	F2	40306.6719	0.1756	6	0	9	8
	F3	40307.2773	0.1578	6	0	9	8
P11(2-7)	F1	40215.4805	0.4	7	2	11	10
	F2	40215.2188	0.467	7	2	11	10
	F3	40216.0664	0.681	7	2	11	10
P11(0-6)	F1	40281.2266	0.109	6	0	11	10
	F2	40281.1328	0.179	6	0	11	10
	F3	40281.7852	0.163	6	0	11	10
R11(2-7)	F1	40251.4922	0.377	7	2	11	12
	F2	40251.3008	0.4704	7	2	11	12
	F3	40252.2266	0.7126	7	2	11	12
R11(0-6)	F1	40318.5313	0.1068	6	0	11	12
	F2	40318.5078	0.1828	6	0	11	12
	F3	40319.2266	0.1685	6	0	11	12
R13(2-7)	F1	40227.3906	0.3564	7	2	13	14
	F2	40227.2539	0.474	7	2	13	14
	F3	40228.2305	0.7437	7	2	13	14
R13(0-6)	F1	40295.1797	0.1049	6	0	13	14
	F2	40295.1992	0.1871	6	0	13	14
	F3	40295.9688	0.1743	6	0	13	14

Table A.2.: Properties of the O_2 transitions relevant for the analysis in chapter 6 data is taken from LIFSIM [92].

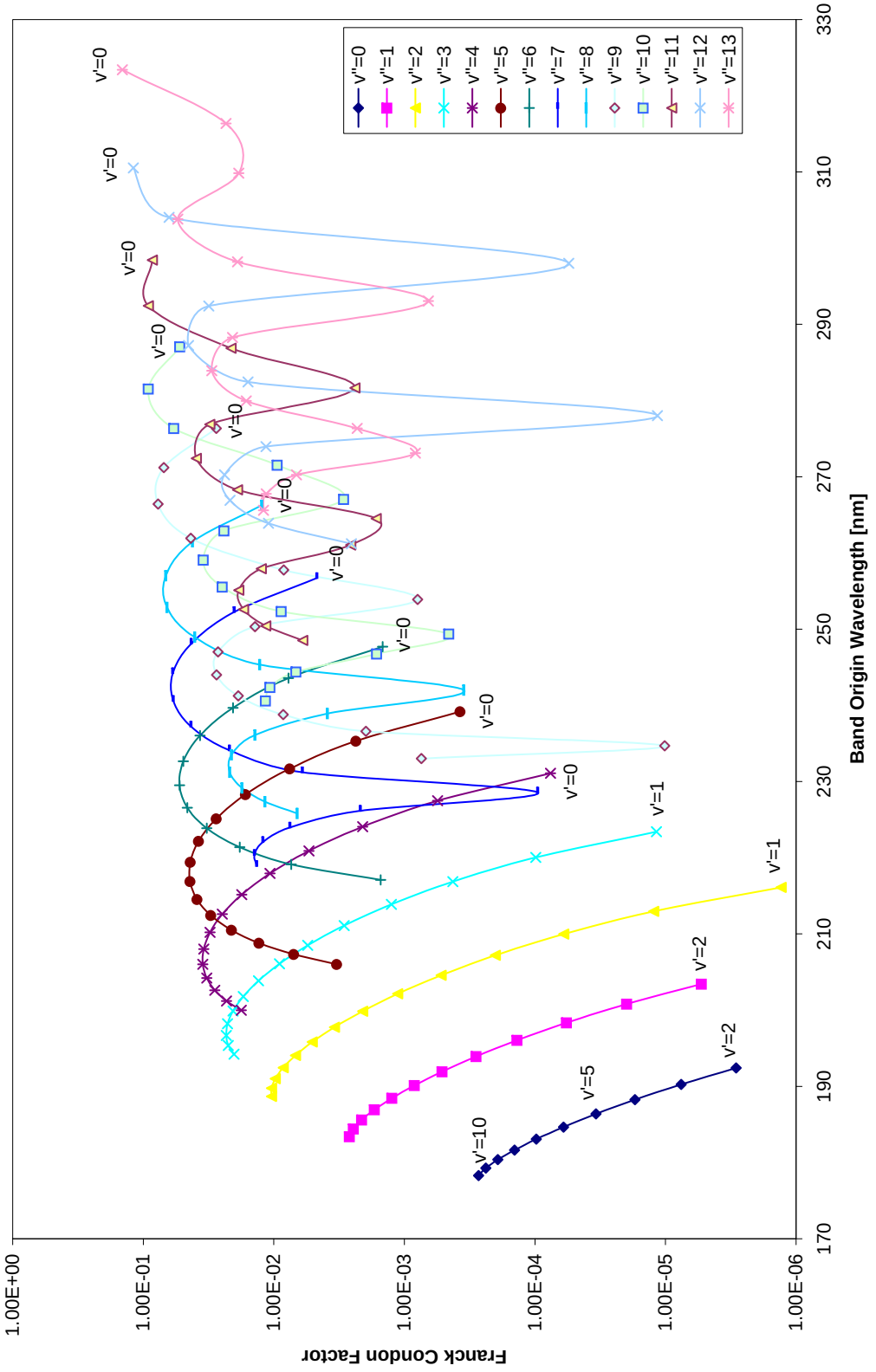

Figure A.1.: Selected Franck Condon Factors of the Schumann-Runge system, data taken from Albritton et al. [112].

A.2. Experimental Data

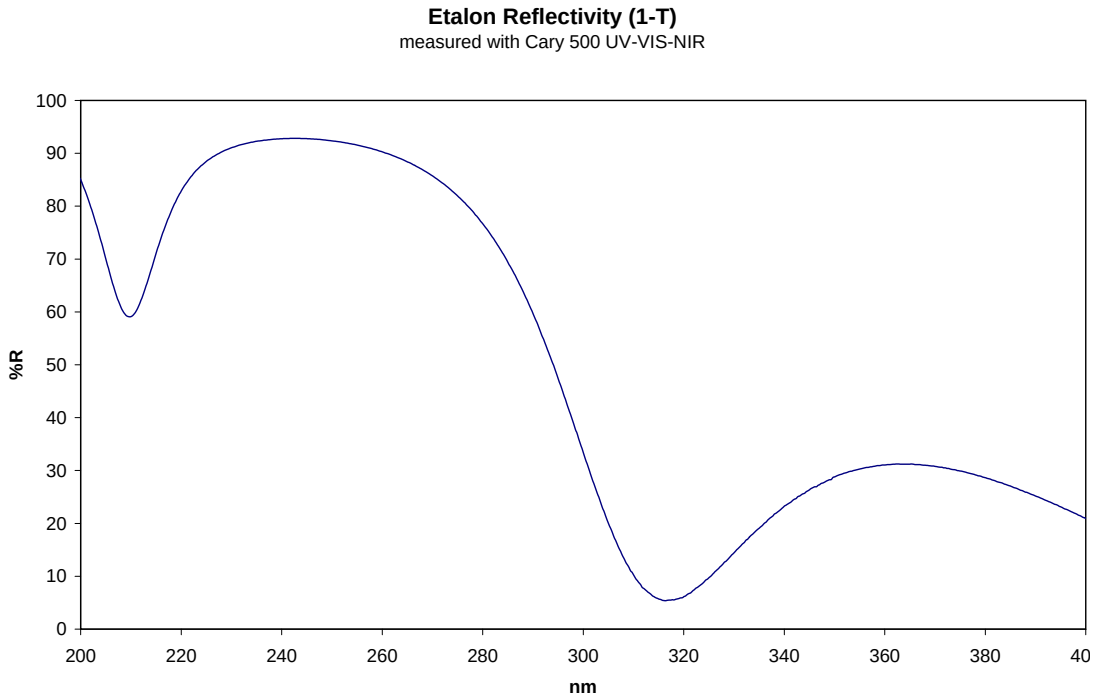

Figure A.2.: Fabry-Perot Etalon Reflectivity measured with a Cary 500 UV-VIS-NIR.

n_c = 1.45637 at 656.3 nm
n_d = 1.45846 at 587.6 nm
n_F = 1.46313 at 486.1 nm
n_g = 1.46669 at 435.8 nm
n = 1.50855 at 248 nm

At 20°C, 1 bar atmospheric pressure
Accuracy: $\pm 3 \cdot 10^{-5}$

Figure A.3.: Suprasil refractive index from Heraeus fact sheet.

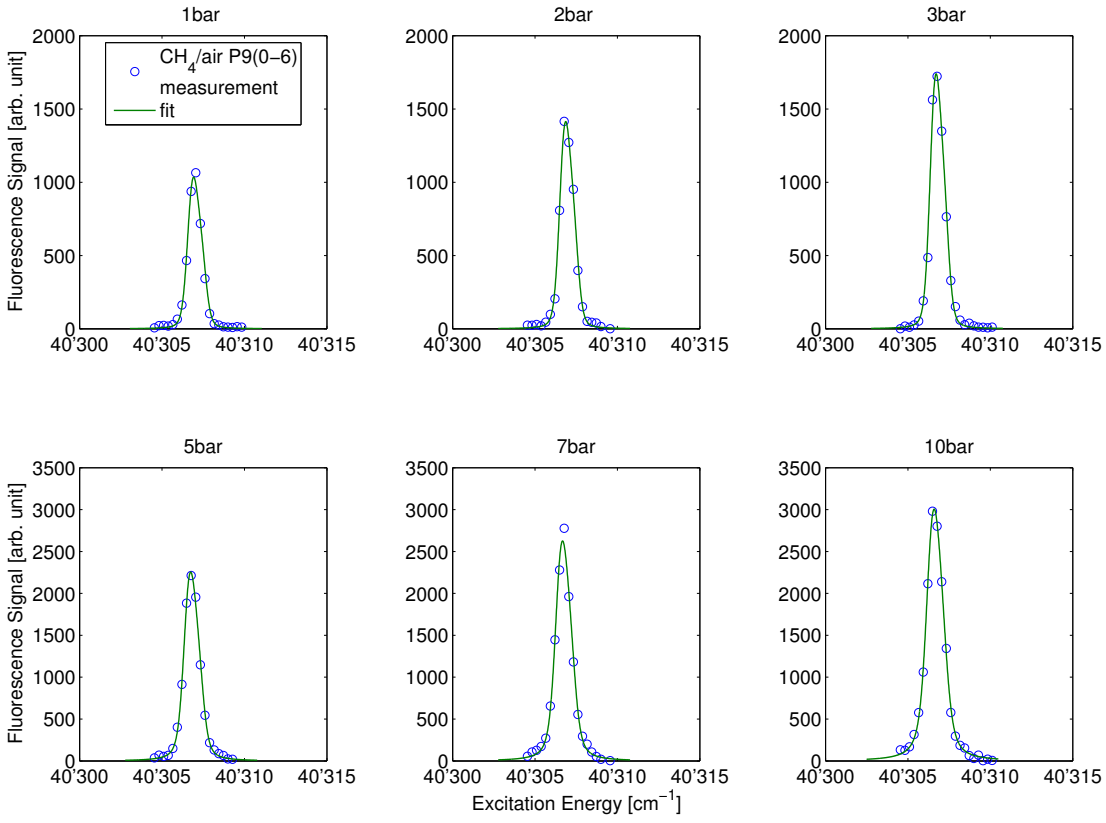

Figure A.4.: Lineshape fits of the P9(0-6) line measured in CH_4/air Flames.

A.3. Decomposition with NMF

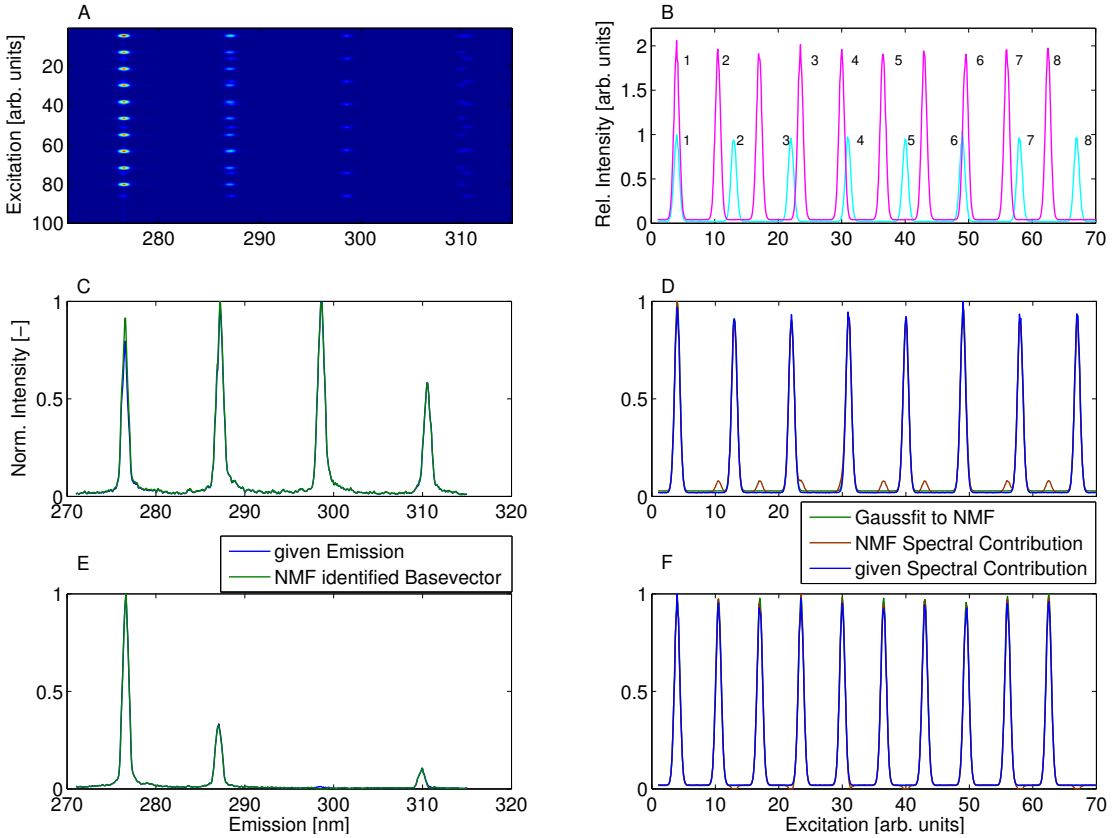

Figure A.5.: Decomposition with NMF of an artificial spectrum with fixed emission locations.

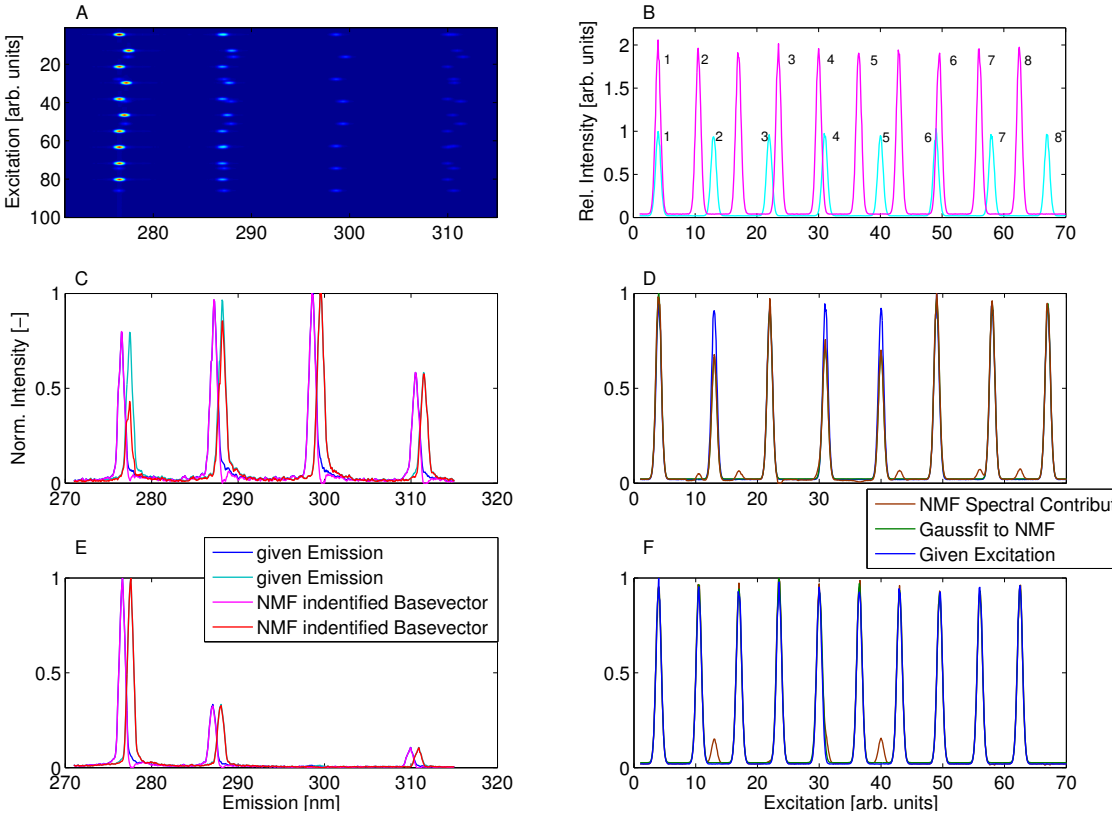

Figure A.6.: Decomposition with NMF of an artificial spectrum with shifted emission locations.

A.4. MEG comparison

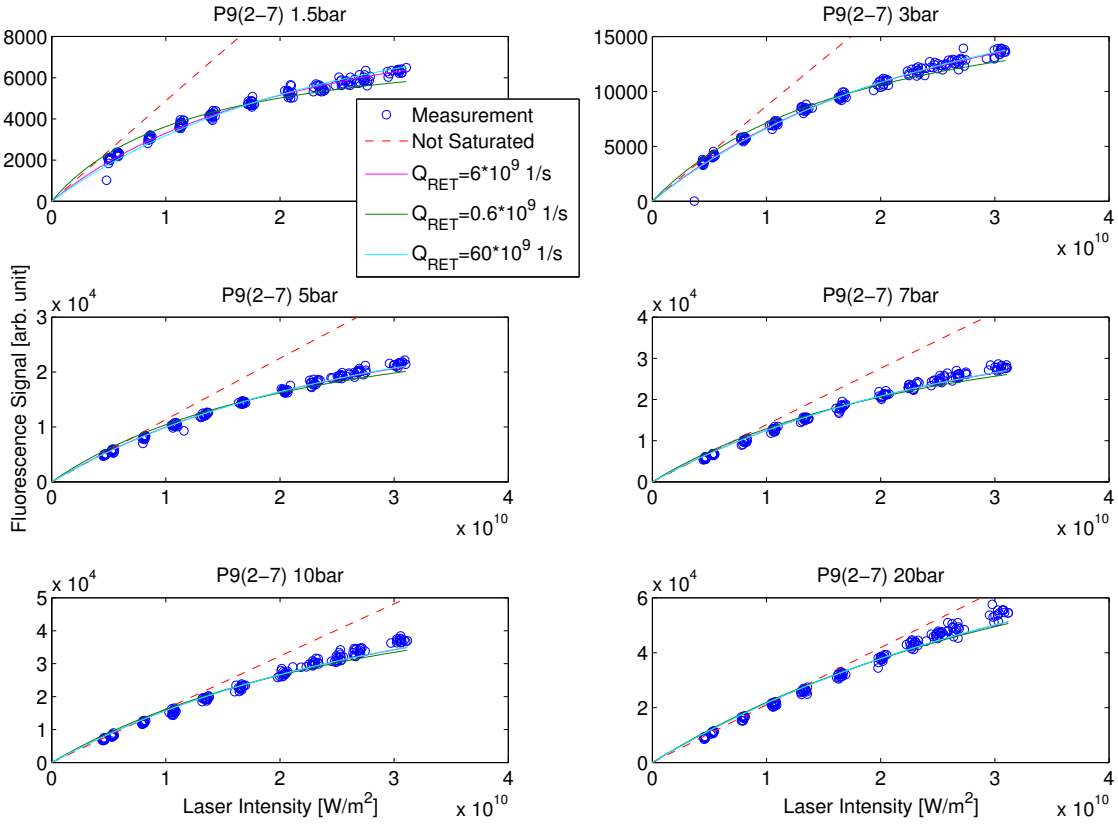

Figure A.7.: Three-level model fits compared for different Q_{RET}.

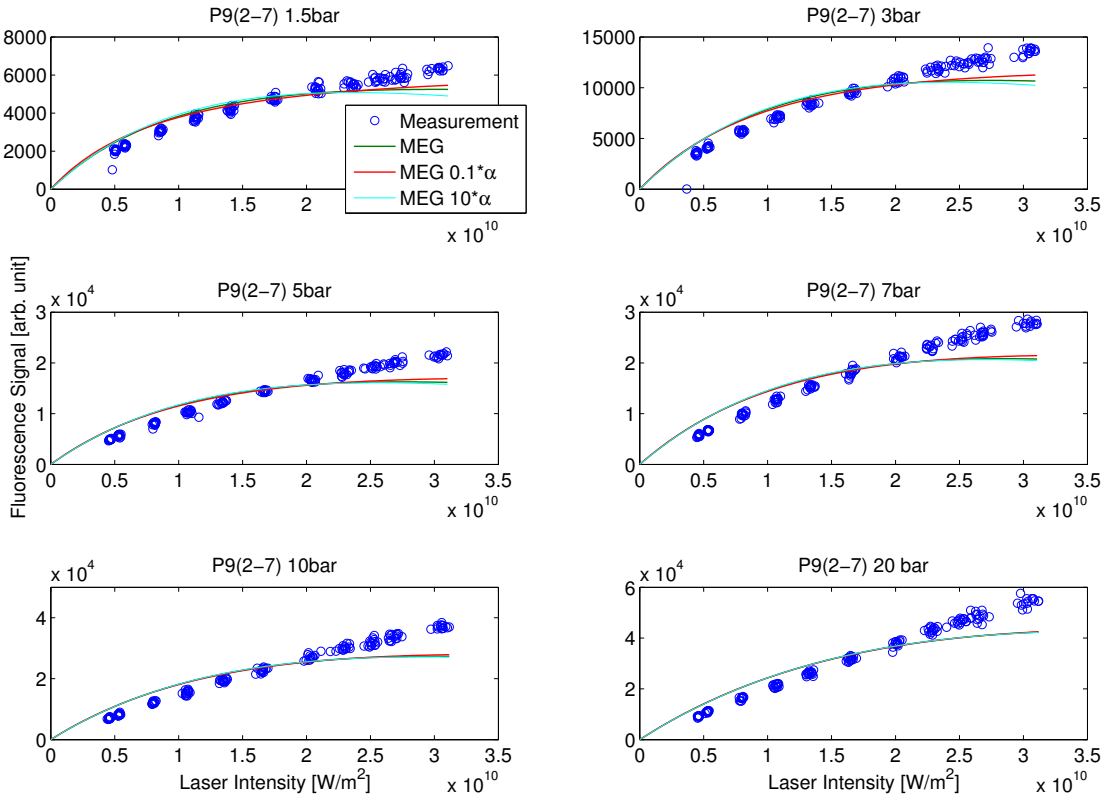

Figure A.8.: State-to-state rate model fits compared for different α.

Bibliography

[1] World Energy Council. World Energy Resources 2013 Survey, 2013. URL `www.worldenergy.org`.

[2] IPCC, 2013: Summary for Policymakers. In *Climate Change 2013: The Physical Science Basis. Contribution of Working Group I to the Fifth Assessment Report of the Intergovernmental Panel on Climate Change*. Stocker, T.F., D. Qin, G.-K. Plattner, M. Tignor, S. K. Allen, J. Boschung, A. Nauels, Y. Xia, V. Bex, P.M. Midgley (eds.), Cambridge University Press, Cambridge, United Kingdom and New York, NY, USA, 2013.

[3] R. Bombach and B. Käppeli. Simultaneous visualisation of transient species in flames by planar-laser-induced fluorescence using a single laser system. *Applied Physics B*, 68(2):251–255, 1999.

[4] P. H. Krupenie. The spectrum of molecular oxygen. *Journal of Physical and Chemical Reference Data*, 1:423, 1972.

[5] V. Schumann. On the absorption and emission of air and its ingredients of wavelenghts from 250nm to 100nm. *Smithsonian contributions to knowledge*, 29:1413, 1903.

[6] C.D. Runge. Physica 1, 254, 1921.

[7] J. Curry and G. Herzberg. Über die ultravioletten Absorptionsbanden des Sauerstoffs (Schumann-Runge-Banden). *Annalen der Physik*, 411(7):800–808, 1934.

[8] D. M. Creek and R. W. Nicholls. A comprehensive re-analysis of the O_2 Schumann-Runge band system. *Proceedings of the Royal Society A: Mathematical, Physical and Engineering Sciences*, 341(1627):517–536, 1975.

[9] T. G. Slanger and P. C. Cosby. Oxygen spectroscopy below 5.1 eV. *The Journal of Physical Chemistry*, 92(2):267–282, 1988.

[10] B. R. Lewis, S. T. Gibson, and P. M. Dooley. Fine-structure dependence of predissociation linewidth in the Schumann-Runge bands of molecular oxygen. *The Journal of Chemical Physics*, 100(10):7012, 1994.

[11] V. Sick and M. Szabadi. Einstein coefficients for oxygen B-X transitions used in LIF experiments with tunable KrF excimer lasers. *Journal of Quantitative Spectroscopy and Radiative Transfer*, 54(5):891 – 898, 1995.

[12] L. Bytautas, N. Matsunaga, and K. Ruedenberg. Accurate ab initio potential energy curve of O_2. II. Core-valence correlations, relativistic contributions, and vibration-rotation spectrum. *The Journal of Chemical Physics*, 132:074307, 2010.

[13] M. Decker. *Einfluss von Stossprozessen auf die zweidimensionale Temperaturfeldbestimmung mittels laserinduzierter Fluoreszenz an molekularem Sauerstoff unter Hochdruckbedingungen.* PhD thesis, Ruprecht-Karls-Universität Heidelberg, 1995.

[14] A. C. Eckbreth. *Laser Diagnostics for Combustion Temperature and Species.* Gordon and Breach Publishers, Combustion Science & Technology Book Series, Vol. 3, second edition, 1996.

[15] K. Kohse-Höinghaus. Laser techniques for the quantitative detection of reactive intermediates in combustion systems. *Progress in Energy and Combustion Science*, 20(3):203–279, 1994.

[16] K. Kohse-Höinghaus. *Applied combustion diagnostics.* Taylor and Francis, 2002.

[17] C. E. Frouzakis and K. Boulouchos. Analysis and reduction of the CH_4-air mechanism at lean conditions. *Combustion Science and Technology*, 159:281–303, 2000.

[18] G. P. Smith, D. M. Golden, M. Frenklach, N. W. Moriarty, B. Eiteneer, M. Goldenberg, C. T. Bowman, R. K. Hanson, S. Song, W. C. Gardiner Jr., V. V. Lissianski, and Z. Qin. URL `http://www.me.berkeley.edu/gri_mech/`.

[19] R.J. Kee, F.M. Rupley, and J.A. Miller. Chemkin II: A Fortran chemical kinetics package for the analysis of gas-phase chemical kinetics, Report No. SAND89-8009B, 1996.

[20] C. D. Carter, J. M. Donbar, and J. F. Driscoll. Simultaneous CH planar laser-induced fluorescence and particle imaging velocimetry in turbulent nonpremixed flames. *Applied Physics B*, 66(1):129–132, 1998.

[21] P. H. Paul and H. N. Najm. Planar laser-induced fluorescence imaging of flame heat release rate. *Symposium (International) on Combustion*, 27(1):43–50, 1998.

[22] J. H. Grinstead, G. Laufer, and Jr. J. C. McDaniel. Single-pulse, two-line temperature-measurement technique using KrF laser-induced O_2 fluorescence. *Applied Optics*, 34(24):5501–5512, 1995.

[23] P. Andresen, A. Bath, W. Gröger, H. W. Lülf, G. Meijer, and J. J. ter Meulen. Laser-induced fluorescence with tunable excimer lasers as a possible method for instantaneous temperature field measurements at high pressures: checks with an atmospheric flame. *Applied Optics*, 27(2):365–378, 1988.

[24] T. Lee, W. G. Bessler, C. Schulz, M. Patel, J. B. Jeffries, and R. K. Hanson. UV planar laser induced fluorescence imaging of hot carbon dioxide in a high-pressure flame. *Applied Physics B*, 79(4):427–430, 2004.

[25] J. O. Berg and W. L. Shackleford. Rotational redistribution effect on saturated laser-induced fluorescence. *Applied Optics*, 18(13):2093, 1979.

[26] R. P. Lucht, D. W. Sweeney, and N. M. Laurendeau. Balanced cross-rate model for saturated molecular fluorescence in flames using a nanosecond pulse length laser. *Applied Optics*, 19(19):3295–300, 1980.

[27] D. Stepowski and M. J. Cottereau. Time resolved study of rotational energy-transfer in A $^2\Sigma^+(\nu' = 0)$ state of OH in a flame by laser-induced fluorescence. *Journal of Chemical Physics*, 74(12):6674–6679, 1981.

[28] M. P. Lee, B. K. McMillin, and R. K. Hanson. Temperature measurements in gases by use of planar laser-induced fluorescence imaging of NO. *Applied Optics*, 32(27):5379–96, 1993.

[29] Q.-V. Nguyen and P. H. Paul. KrF laser-induced photobleaching effects in O_2 planar laser-induced fluorescence signals: experiment and model. *Applied Optics*, 36(12):2675–2683, Apr 1997.

[30] E. W. Rothe, Y. W. Gu, and G. P. Reck. Laser-induced predissociative fluorescence: dynamics and polarization and the effect of lower-state rotational energy transfer on quantitative diagnostics. *Applied Optics*, 35(6):934–47, 1996.

[31] D. Secrest. Theory of rotational and vibrational energy-transfer in molecules. *Annual Review of Physical Chemistry*, 24:379–406, 1973.

[32] J. H. Grinstead, G. Laufer, and J. C. Mcdaniel. Rotational temperature-measurement in high-temperature air using KrF laser-induced O_2 fluorescence. *Applied Physics B*, 57(6):393–396, 1993.

[33] T. Brunner and D. Pritchard. Fitting laws for rotationally inelastic collisions. *Dynamics of the excited state*, 50:589–641, 1982.

[34] J. C. Polanyi. Mechanism of rotational relaxation. *The Journal of Chemical Physics*, 56(4):1563, 1972.

[35] M. L. Koszykowski, L. A. Rahn, R. E. Palmer, and M. E. Coltrin. Theoretical and experimental studies of high-resolution inverse Raman spectra of molecular nitrogen at 1-10 atm. *The Journal of Physical Chemistry*, 91(1):41–46, 1987.

[36] T. Brunner, R. Driver, N. Smith, and D. Pritchard. Simple scaling law for rotational-energy transfer in Na_2^*-Xe collisions. *Physical Review Letters*, 41(13): 856–859, 1978.

[37] G. Knopp, P. Radi, M. Tulej, T. Gerber, and P. Beaud. Collision induced rotational energy transfer probed by time-resolved coherent anti-Stokes Raman scattering. *The Journal of Chemical Physics*, 118(18):8223, 2003.

[38] J. I. Steinfeld, P. Ruttenberg, G. Millot, G. Fanjoux, and B. Lavorel. Scaling laws for inelastic collision processes in diatomic molecules. *The Journal of Physical Chemistry*, 95(24):9638–9647, 1991.

[39] T. Seeger, F. Beyrau, A. Braeuer, and A. Leipertz. High-pressure pure rotational CARS: comparison of temperature measurements with O_2, N_2 and synthetic air. *Journal of Raman Spectroscopy*, 34(12):932–939, 2003.

[40] D. Rapp and T. Kassal. Theory of vibrational energy transfer between simple molecules in monreactive collisions. *Chemical Reviews*, 69(1):61, 1969.

[41] M. Kneba and J. Wolfrum. Bimolecular reactions of vibrationally excited molecules. *Annual Review of Physical Chemistry*, 31:47–79, 1980.

[42] J.D. Lambert. *Vibrational and rotational relaxation in gases.* Clarendon Press, 1977.

[43] M. Capitelli, C. M. Ferreira, B. F. Gordiets, and A. I. Osipov. Plasma kinetics in atmospheric gases. *Plasma Physics and Controlled Fusion*, 43(3):371–372, 2001.

[44] E. Landau, L .and Teller. Zur Theorie der Schalldispersion. *Physikalische Zeitschrift der Sowjetunion*, 10(1):34–43, 1936.

[45] V. Sick, M. Decker, J. Heinze, and W. Stricker. Collisional process in the O_2 B $^3\Sigma_u^-$ state. *Chemical Physics Letters*, 249:335–340, 1996.

[46] C. Coletti and G. D. Billing. Vibrational energy transfer in molecular oxygen collisions. *Chemical Physics Letters*, 356(1-2):14–22, 2002.

[47] Fabrizio Esposito and Mario Capitelli. The relaxation of vibrationally excited f O_2 molecules by atomic oxygen. *Chemical Physics Letters*, 443:222–226, 2007.

[48] P. W. Fairchild, G.P. Smith, and D. R. Crosley. Collisional quenching of $A^2\sigma^+$ OH at elevated temperatures. *The Journal of Chemical Physics*, 79(4):1795, 1983.

[49] D. L. Holtermann. Rates of collision-induced electronic relaxation of single rotational levels of SO_2: Quenching mechanism by collision complex formation. *The Journal of Chemical Physics*, 77(11):5327, 1982.

[50] P. H. Paul, J. A. Gray, J. L. Durant, and J. W. Thoman. A model for temperature-dependent collisional quenching of NO A $^2\Sigma^+$. *Applied Physics B*, 57(4):249–259, 1993.

[51] M. Mailänder. Determination of absolute transition probabilities and particle densities by saturated fluorescence excitation. *Journal of Applied Physics*, 49(3):1256, 1978.

[52] A. P. Baronavski and J. R. McDonald. Application of saturation spectroscopy to the measurement of C_2, $^3\Pi_u$ concentrations in oxy-acetylene flames. *Applied Optics*, 16(7):1897–901, 1977.

[53] P. A. Bonczyk and J. A. Shirley. Measurement of CH and CN concentration in flames by laser-induced saturated fluorescence. *Combustion and Flame*, 34:253–264, 1979.

[54] M. Schäfer, W. Ketterle, and J. Wolfrum. Saturated 2D-LIF of OH and 2D determination of effective collisional lifetimes in atmospheric-pressure flames. *Applied Physics B*, 52(5):341–346, 1991.

[55] Y. Takubo, H. Yano, H. Matsuoka, and M. Shimazu. Saturation behavior of laser-induced CH fluorescence in a propane-air flame. *Journal of Quantitative Spectroscopy and Radiative Transfer*, 30(2):163–168, 1983.

[56] D. Killinger, Ch. Wang, and M. Hanabusa. Intensity and pressure dependence of resonance fluorescence of OH induced by a tunable UV laser. *Physical Review A*, 13(6):2145–2152, 1976.

[57] R. P. Lucht, N. M. Laurendeau, and D. W. Sweeney. Temperature measurement by two-line laser-saturated OH fluorescence in flames. *Applied Optics*, 21(20):3729–35, 1982.

[58] L. Pasternack, A. P. Baronavski, and J. R. McDonald. Application of saturation spectroscopy for measurement of atomic Na and MgO in acetylene flames. *The Journal of Chemical Physics*, 69(11):4830, 1978.

[59] K. Schofield. Quantitative atomic and molecular laser fluorescence in the study of detailed combustion processes. *Optical Engineering*, 20(4):204501, 1981.

[60] D. R. Crosley. Collisional effects on laser-induced fluorescence flame measurements. *Optical Engineering*, 20(4):204511, 1981.

[61] R. Altkorn and R. N. Zare. Effects of saturation on laser-induced fluorescence measurements of population and polarization. *Annual Review of Physical Chemistry*, 35:265–289, 1984.

[62] C. H. Muller, K. Schofield, and M. Steinberg. Near saturation laser induced chemical reactions of Na 3 $^2P_{3/2,1/2}$ in $H_2/O_2/N_2$ flames. *Chemical Physics Letters*, 57 (3):364–368, 1978.

[63] C. H. Muller, K. Schofield, and M. Steinberg. Laser induced flame chemistry of Li and Na . Implications for other saturated mode measurements. *The Journal of Chemical Physics*, 72(12):6620, 1980.

[64] K. Kohse-Höinghaus, W. Perc, and T. Just. Laser-induced saturated fluorescence as a method for the determination of radical concentrations in flames. *Berichte der Bunsen-Gesellschaft*, 87(11):1052–1057, 1983.

[65] E. W. Rothe, Y. Gu, A. Chryssostomou, P. Andresen, and F. Bormann. Effect of laser intensity and of lower-state rotational energy transfer upon temperature measurements made with laser-induced predissociative fluorescence. *Applied Physics B*, 66:251–258, 1998.

[66] M. V. Heitor and A. L. N. Moreira. Thermocouples and sample probes for combustion studies. *Progress in Energy and Combustion Science*, 19(3):259–278, 1993.

[67] M. Raffel, Ch. E. Willert, S. T. Wereley, and J. Kompenhans. *Particle image velocimetry*. Springer Berlin Heidelberg, 2007.

[68] J. B. Abbiss, T. W. Chubb, and E. R. Pike. Laser Doppler anemometry. *Optics & Laser Technology*, 6:249–261, 1974.

[69] C. J. D. Pickering and N. A. Halliwell. Laser speckle photography and particle image velocimetry: photographic film noise. *Applied Optics*, 23(17):2961, 1984.

[70] R. J. Adrian. Scattering particle characteristics and their effect on pulsed laser measurements of fluid-flow - speckle velocimetry vsparticle image velocimetry. *Applied Optics*, 23(11):1690–1691, 1984.

[71] R. J. Adrian. Twenty years of particle image velocimetry. *Experiments in Fluids*, 39(2):159–169, 2005.

[72] M. Lapp and C.M. Penney. *Laser Raman gas diagnostics*. Springer US, 1974.

[73] S. Lederman. The use of laser Raman diagnostics in flow fields and combustion. *Progress in Energy and Combustion Science*, 3(1):1–34, 1977.

[74] S. H. Starner, R. W. Bilger, R. W. Dibble, and R. S. Barlow. Some Raman/Rayleigh/LIF measurements in turbulent propane flames. *Symposium (International) on Combustion*, 23(1):645–651, 1991.

[75] A. Masri. Turbulent nonpremixed flames of methane near extinction: Mean structure from Raman measurements. *Combustion and Flame*, 71(3):245–266, 1988.

[76] F. Hassel, A. Hundhausen, Th Klos, U. Sprenzel, and H. Bockhorn. Joint PDFs of scalar quantities in turbulent diffusion flames by Raman and Rayleigh scattering. *Berichte der Bunsen-Gesellschaft*, 97(12):1713–1716, 1993.

[77] P. R. Regnier. On the possibility of measuring gas concentrations by stimulated anti-Stokes scattering. *Applied Physics Letters*, 23(5):240, 1973.

[78] F. Moya, S. A. J. Druet, and J. P. E. Taran. Gas spectroscopy and temperature measurement by coherent Raman anti-stokes scattering. *Optics Communications*, 13(2):169–174, 1975.

[79] J. D. Miller, M. N. Slipchenko, T. R. Meyer, H. U. Stauffer, and J. R. Gord. Hybrid femtosecond/picosecond coherent anti-Stokes Raman scattering for high-speed gas-phase thermometry. *Optics Letters*, 35(14):2430–2, 2010.

[80] J. D. Miller, S. Roy, M. N. Slipchenko, J. R. Gord, and T. R. Meyer. Single-shot gas-phase thermometry using pure-rotational hybrid femtosecond/picosecond coherent anti-Stokes Raman scattering. *Optics Express*, 19(16):15627–40, 2011.

[81] J. D. Miller, C. E. Dedic, S. Roy, J. R. Gord, and T. R. Meyer. Interference-free gas-phase thermometry at elevated pressure using hybrid femtosecond/picosecond rotational coherent anti-Stokes Raman scattering. *Optics Express*, 20(5):5003–10, 2012.

[82] Y. Ghermay, J. Mantzaras, R. Bombach, and K. Boulouchos. Homogeneous combustion of fuel-lean $H_2/O_2/N_2$ mixtures over platinum at elevated pressures and preheats. *Combustion and Flame*, 158(8):1491–1506, 2011.

[83] S. Daniele, P. Jansohn, J. Mantzaras, and K. Boulouchos. Turbulent flame speed for syngas at gas turbine relevant conditions. *Proceedings of the Combustion Institute*, 33(2):2937–2944, 2011.

[84] R. Suntz, H. Becker, P. Monkhouse, and J. Wolfrum. Two-dimensional visualization of the flame front in an internal combustion engine by laser-induced fluorescence of OH radicals. *Applied Physics B*, 47(4):287–293, 1988.

[85] H. Becker, A. Arnold, R. Suntz, P. Monkhouse, J. Wolfrum, R. Maly, and W. Pfister. Investigation of flame structure and burning behaviour in an IC engine simulator by 2D-LIF of OH radicals. *Applied Physics B*, 50(6):473–478, 1990.

[86] I. Boxx, M. Stöhr, C. Carter, and W. Meier. Temporally resolved planar measurements of transient phenomena in a partially pre-mixed swirl flame in a gas turbine model combustor. *Combustion and Flame*, 157(8):1510–1525, 2010.

[87] Q. V. Nguyen, R. W. Dibble, C. D. Carter, G. J. Fiechtner, and R. S. Barlow. Raman-LIF measurements of temperature, major species, OH, and NO in a methane-air bunsen flame. *Combustion and Flame*, 105(4):499–510, 1996.

[88] J. M. Seitzman, G. Kychakoff, and R. K. Hanson. Instantaneous temperature field measurements using planar laser-induced fluorescence. *Optics Letters*, 10(9):439, 1985.

[89] R. Giezendanner-Thoben, U. Meier, W. Meier, J. Heinze, and M. Aigner. Phase-locked two-line OH planar laser-induced fluorescence thermometry in a pulsating gas turbine model combustor at atmospheric pressure. *Applied Optics*, 44(31): 6565, 2005.

[90] W. G. Bessler and C. Schulz. Quantitative multi-line NO-LIF temperature imaging. *Applied Physics B*, 78(5):519–533, 2004.

[91] A. Denisov, G. Colmegna, and P. Jansohn. Temperature measurements in sooting counterflow diffusion flames using laser-induced fluorescence of flame-produced nitric oxide. *Applied Physics B*, 2013.

[92] W. G. Bessler, C. Schulz, V. Sick, and J. W. Daily. A versatile modeling tool for nitric oxide LIF spectra. In *Proceedings of the Third Joint Meeting of the U.S. Sections of The Combustion Institute (Chicago, March 16-19, 2003, paper PI05)*, 2003.

[93] M. P. Lee, P. H. Paul, and R. K. Hanson. Laser-fluorescence imaging of O_2 in combustion flows using an ArF laser. *Optics Letters*, 11(1):7, 1986.

[94] J. E. Goldsmith and R. J. Anderson. Laser-induced fluorescence spectroscopy and imaging of molecular oxygen in flames. *Optics Letters*, 11(2):67, 1986.

[95] M. P. Lee, P. H. Paul, and R. K. Hanson. Quantitative imaging of temperature fields in air using planar laser-induced fluorescence of O_2. *Optics Letters*, 12(2): 75, 1987.

[96] G. Witt, J. Stegman, D. P. Murtagh, I. C. Mcdade, R. G. H. Greer, P. H. G. Dickinson, and D. B. Jenkins. Collisional energy-transfer and the excitation of O_2 b $^1\Sigma_g^+$ in the atmosphere. *Journal of Photochemistry*, 25(2-4):365–378, 1984.

[97] L. R. Martin, R. B. Cohen, and J. F. Schatz. Quenching of laser induced fluorescence of O_2 b $^1\Sigma_g^+$ by O_2 and N_2. *Chemical Physics Letters*, 41(2):394–396, 1976.

[98] M. Berry, M. Browne, A. Langville, V. Pauca, and R. Plemmons. Algorithms and applications for approximate nonnegative matrix factorization. *Computational Statistics & Data Analysis*, 52(1):155–173, 2007. ISSN 01679473.

[99] J. W. Daily. Laser induced fluorescence spectroscopy in flames. *Progress in Energy and Combustion Science*, 23(2):133–199, 1997.

[100] G. Millot, R. Saint-Loup, J. Santos, R. Chaux, H. Berger, and J. Bonamy. Collisional effects in the stimulated Raman Q branch of O_2 and $O_2 - N_2$. *The Journal of Chemical Physics*, 96(2):961, 1992.

[101] K. Bennett and R. L. Byer. Computer-controllable wedged-plate optical variable attenuator. *Applied Optics*, 19(14):2408–2412, 1980.

[102] M. Reinke, J. Mantzaras, R. Schaeren, R. Bombach, A. Inauen, and S. Schenker. High-pressure catalytic combustion of methane over platinum: In situ experiments and detailed numerical predictions. *Combustion and Flame*, 136(1-2):217–240, 2004.

[103] E. Hecht. *Optik*. Addison-Wesley Publishing Company, 5. Auflage, 2009.

[104] J. Luque and D. R. Crosley. Database and spectral simulation for OH $A - X$; OD $A - X$; NO $A - X$, $B - X$, $D - X$; CH $A - X$, $B - X$, $C - X$; CN $B - X$; SiH $A - X$ and CF $A - X$. URL `http://www.sri.com/cem/lifbase`.

[105] R. C. Hilborn. Einstein coefficients, cross sections, f values, dipole moments, and all that. *American Journal of Physics*, 50:982–986, 1982.

[106] F.K. Kneubühl. *Laser*. Vieweg+Teubner, 2008.

[107] M. Schultze, J. Mantzaras, R. Bombach, and K. Boulouchos. An experimental and numerical investigation of the hetero-/homogeneous combustion of fuel-rich hydrogen/air mixtures over platinum. *Proceedings of the Combustion Institute*, 34 (2):2269–2277, 2013.

[108] V. Vasudevan, D. F. Davidson, and R. K. Hanson. Direct measurements of the reaction $OH + CH_2O \rightarrow HCO + H_2O$ at high temperatures. *International Journal of Chemical Kinetics*, 37(2):98–109, 2005.

[109] R. Stocker and D. Hein. www.combustion-database.com.

[110] M. Schultze, J. Mantzaras, F. Grygier, and R. Bombach. Hetero-/homogeneous combustion of syngas mixtures over platinum at fuel rich stoichiometries and pressures up to 14 bar. *Proceedings of the Combustion Institute*, 2014, in press.

[111] D. L. Huestis. Vibrational energy transfer and relaxation in O_2 and H_2O. *Journal of Physical Chemistry*, 110(21):6638–42, 2006.

[112] D. L. Albritton, A. L. Schmeltekopf, and R. N. Zare. Diatomic intensity factors. data tabulated in Krupenie [4].

Publication List (at printing date)

Marco Schultze, John Mantzaras, Felix Grygier, Rolf Bombach, Hetero-/homogeneous combustion of syngas mixtures over platinum at fuel rich stoichiometries and pressures up to 14 bar, *Proceedings of the Combustion Institute*, 2014, in press.

Poster Presentations

Oxygen Thermometry - Effects of Rotational Energy Transfer within the O_2 $X^3\Sigma_g^-(v'' = 7)$ state,
34th International Symposium on Combustion 2012, Warsaw,

Rotational Energy Transfer within the O_2 $X^3\Sigma_g^-(v'' = 7)$ state,
Gordon Research Seminar Laser Diagnostics in Combustion 2013, Waterville Valley NH

Rotational Energy Transfer within the O_2 $X^3\Sigma_g^-(v'' = 7)$ state,
Gordon Research Conference Laser Diagnostics in Combustion 2013, Waterville Valley NH